Sedimentary structure, subsidence history and roughness analysis of Nansen and Amundsen Basin, Arctic Ocean

Sedimentstruktur, Subsidenz- und Rauhigkeitsanalyse des Nansen und Amundsen Beckens, Arktischer Ozean

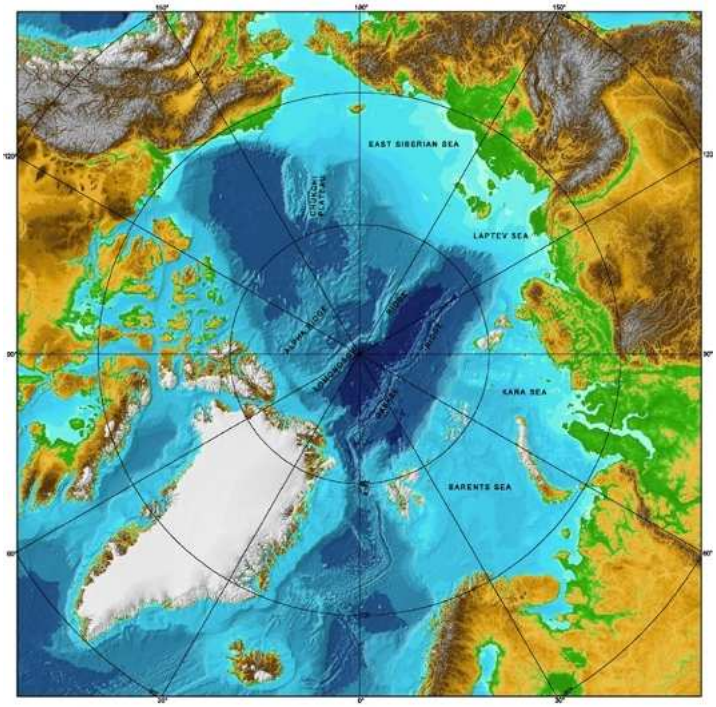

Diplomarbeit

von
Uli Micksch

Geophysikalisches Institut
der Universität Karlsruhe (TH)

30. Januar 2004

Referent: Prof. Dr. Friedemann Wenzel

Korreferent: Prof. Dr. Heinrich Miller

UNIVERSITY OF KARLSRUHE

AWI
Alfred Wegener Institute
for Polar and Marine Research

Eidesstattliche Erklärung

Hiermit erkläre ich, dass ich die vorliegende Diplomarbeit selbständig angefertigt und keine weiteren außer den angegebenen Quellen und Hilfsmittel verwendet habe. Wörtlich oder inhaltlich entnommene Stellen sind als solche kenntlich gemacht.

Karlsruhe, den 30.01.2004

Was ist Wissenschaft anderes,
als die unablässige Taterfüllung
uralter Menschheitsträume?

Stefan Zweig, Die Heilung durch den Geist

Contents

List of Figures

List of Tables

List of abbreviations

m^2	squaremeter
m^3	cubicmeter
A-MR	Alpha-Mendeleev Ridge
AB	Amundsen Basin
AGC	automatic gain control
AGU	American Geophysical Union
AMOR	Arctic Mid Ocean Ridge
AMORE	Arctic Mid Ocean Ridge Expedition
AWI	Alfred-Wegener-Institute for Polar- und Meeresforschung
AWK	data formatting tool, initials of developers
BSR	bottom simulating reflector
CDP	aommon depth point
CMP	common mid point
CRS	aommon reflection surface
D	dimension
EGS	European Geophysical Society
EUG	European Union of Geosciences
FZ	fracture zone
Gb	Gigabyte
GMT	generic mapping tools
GPS	global positioning system
GR	Gakkel Ridge
h	hour
Hz	Hertz
IBCAO	International Bathymetric Chart of the Arctic Ocean
km	kilometers
kn	knots
LR	Lomonosov Ridge
Mb	Megabyte
MOR	Mid Ocean Ridge
ms	milliseconds
Myr	million years
NB	Nansen Basin

NMO	normal move out
p	pressure (wave)
PODAS	Polarstern Data System
r	radius
R/V	research vessel
RMS	root mean square
s	shear (wave)
SB	sonobuoy
SEG-D	standardized seismic data format
SEG-Y	standardized seismic data format
SNR	signal to noise ratio
t	time
to	tons
TWT	two way traveltime
v	velocity
VLF	very low frequency
x, y, z	coordinate axes

1 Introduction

1.1 The Arctic Mid Ocean Ridge Expedition 2001 and the seismic data

During summer 2001 a joint US-German experiment was carried out in the Arctic Ocean. The goal of the AMORE (Arctic Mid Ocean Ridge Expedition) was to investigate Gakkel Ridge, the slowest of the worldwide oceanic spreading centers, as well as the adjacent basins with geophysical, petrological and glaciological methods. Due to the usual heavy ice conditions in these latitudes, a two ship setup was used to ensure data quality during dredging and seismic profiling.

With R/V Polarstern and USCGC Healy (both scientific icebreakers) as support, it was possible to obtain three reflection seismic sections, two in the Nansen Basin and one in the Amundsen Basin. The two ships operated in tandem. USCGC Healy opened a passage through the ice, R/V Polarstern followed with the geophysical gear in tow at a more or less constant speed. In spite of this technique, the sometimes dense ice cover hampered the acquisition. The problems with geophysical data acquisition in ice covered regions are explained below. Along the transects sonobuoys were deployed for wide angle and refraction seismic data.

The seismic sections in the Nansen Basin are labelled 20010100 and 20010460, the profile in the Amundsen Basin is called 20010300. It was possible to merge profile 20010100 to a profile acquired in 1999, labelled 99176. Sonobuoys are labelled SB2101, for example, up to buoy 29.

Figure 1.1 shows the obtained profiles and other important data used in this thesis: The red lines mark the processed profiles, the accompanying black dots mark the dropped sonobuoys. Blue lines mark the magnetic anomalies, the identified chron number is written next to them. Bold black lines mark seismic profiles acquired by R/V Polarstern in 1991, the results from their interpretation are compared with data and results in this work. A insert shows the global setting of the survey areas, the small red rectangles indicate the sector of the profiles in following, more detailed maps. A foldout version of this map is supplied in the appendix for a constant comparison. The depth contour lines are traced every km, the resolution of the topography/bathymetry grid (IBCAO) is 1 km.

The main objectives of the thesis are the development of depth sections from the reflection seismic data with the results from the refraction seismic data-set and to visualize the sedimentary

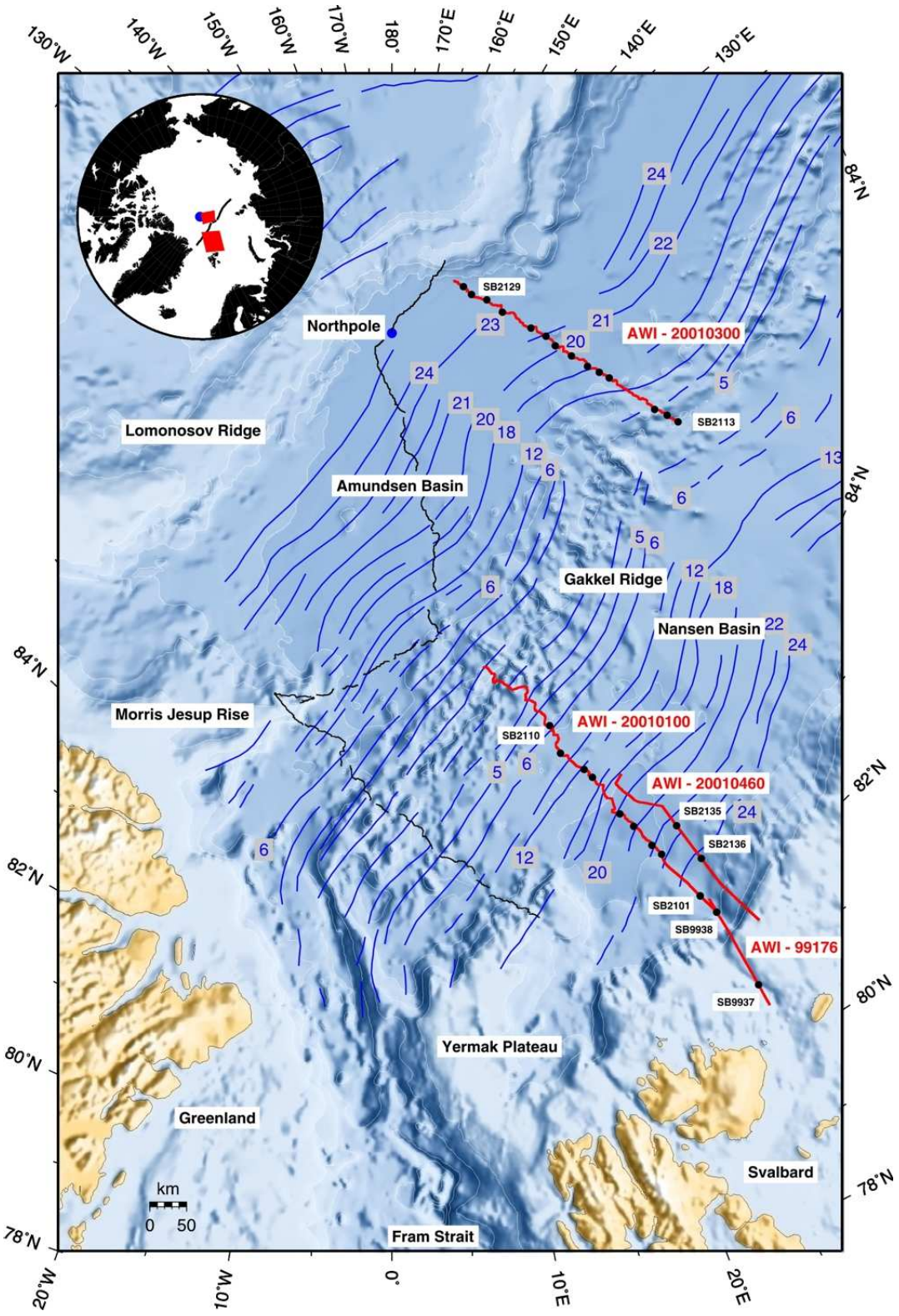

Figure 1.1: Overview map with the seismic profiles

structure in detailed line drawings. Another major goal was the analysis and interpretation of basin subsidence and crustal roughnesses of the available seismic data set.

1.2 Outline of the thesis

First, a morphological and geological introduction to the survey area is given. After describing the experimental setup and gear with its special specifications for a deployment in ice covered regions, the applied data processing sequence is explained in detail.

The first interpretation of the processed seismic data is made during modelling the refraction data set, starting there, by identifying refracted and reflected phases. The outcome of this will be velocity-depth functions at the positions of the sonobuoys, distributed along the reflection seismic transects. This velocity information is used to depth-convert the reflection seismic profiles. A description of the distinctive features in the seismic sections is given afterwards. The subsequent chapters deal with the visualisation of the seismic data (line drawings), and with tools to quantify relations of the basin to their age and the spreading regime of Gakkel Ridge: Subsidence history and crustal roughness analysis. A comparison between Nansen and Amundsen basin is given afterwards, before the major results of this thesis are listed.

A major part of the interpretation is based on the work of Karasik (1968) and Vogt et al. (1979), who described and compiled the geophysical knowledge of the Eurasian Basin, especially about magnetic data and spreading rates of Gakkel Ridge. Their results and interpretations are still valid and confirmed and refined by Brozena et al. (2003), for example. Another source of information are recent publications by Dick et al. (2003), Jokat et al. (2003) and Michael et al. (2003) about petrology and geophysical findings on GR. The results of the roughness calculations are compared the ones obtained by Weigelt (1998) who worked with both seismic an gravimetric profiles from an expedition in 1991 (ARCTIC'91) (black lines in the overview map).

Figure 1.2 shows a satellite image of the ice coverage during the AMORE cruise, since the ice conditions are mentioned a lot. The map shows mainly Greenland to the left, but also line 20010100 towards GR, before the ship track turns 'left' along axis of GR. The white cross marks north pole, reached by the expedition at 6.9.2001. Clearly visible is the decrease of open water space towards the pole, indicating difficult ice conditions for the profile in the Amundsen Basin (20010300). The two following figures (1.3, 1.4) show both ships during the cruise in different ice conditions.

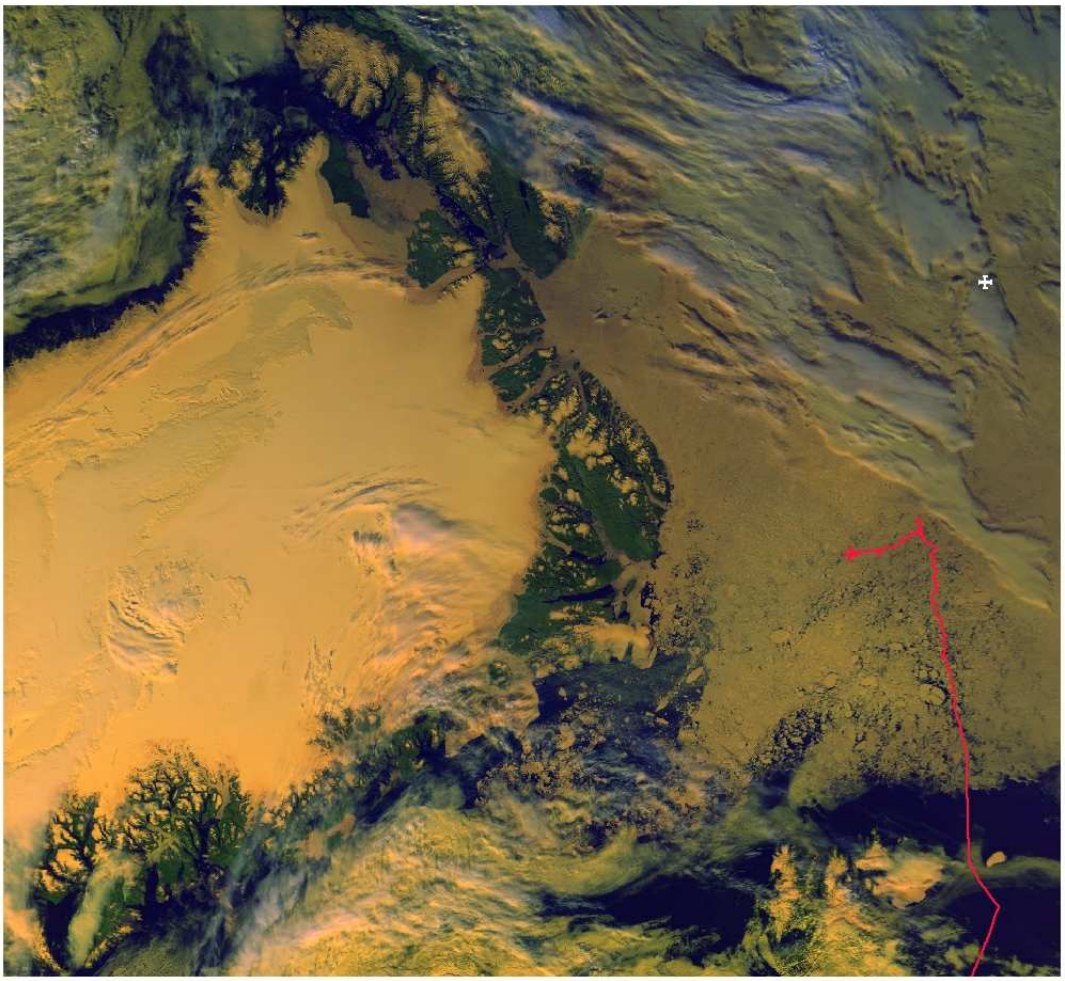

Figure 1.2: Ice conditions, seen from space

Figure 1.3: R/V Polarstern during seismic profiling.

Figure 1.4: USCGC Healy cruising through a polynia (open water between ice floes).

2 Morphological and geological introduction

2.1 General overview

The Arctic Ocean, as we see it today, is imbedded between the huge landmasses of the Eurasian and North American continent. It is divided by the continental Lomonosov Ridge in two oceanic basins, the Amerasian and the Eurasia Basin (see figure 2.1). Each basin again, is subdivided by parallel ridges. The shelf regions of the Arctic Ocean belong to the largest in the world and are almost as big as the deep abyssal plains (49 %) (Johnson, 1990). In addition, there are a couple of submarine plateaus, like Morris Jesup Rise and Yermak Plateau, whose origin is still discussed in literature. Several authors argue for a creation caused by a hot spot, proved by prominent magnetic anomalies (Feden et al., 1979), whereupon more recent investigations find no evidence for a hot spot related creation (Ritzmann and Jokat, 2003).

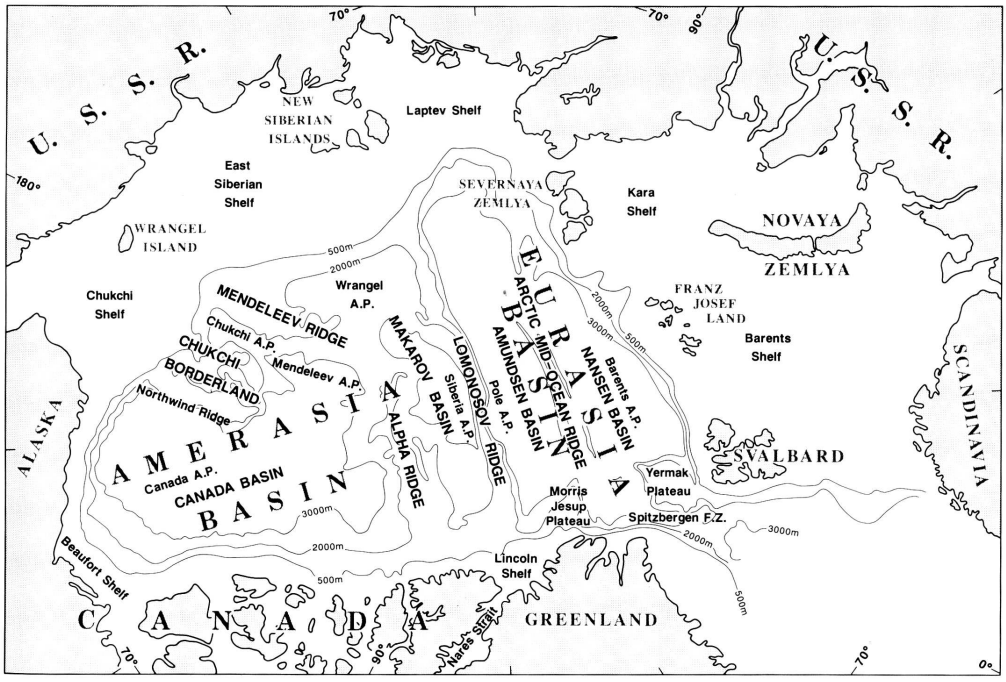

Figure 2.1: Overview map showing the morphological features of the Arctic Ocean, a larger version can be found in the appendix (Grantz et al., 1990).

The focus of this thesis is the Eurasia Basin, with its Nansen and Amundsen sub basins, divided by the worlds slowest Mid Oceanic Ridge, Gakkel Ridge (also known as Nansen or Arctic Mid Ocean Ridge (AMOR)).

The Nansen Basin (NB) extends for about 1800 km with a width of 200 - 500 km. The depth of the abyssal plain ranges between 3000 - 4000 m with very flat topography in the central part of the basin. The Amundsen Basin (AB) has the same dimensions as the NB, but is slightly deeper (4500 m). Estimated sediment thicknesses are derived from depth to source analysis of magnetic data (Kovacs and Vogt, 1982) and are given as 3 - 5 km (NB) and 2.5 km (AB) (Vogt et al., 1979). Crustal thicknesses of the basins are given between 3 and 6 km by Weigelt (1998).

Gakkel Ridge is the northern continuation of the Mid Atlantic Ridge, connected by several smaller ridges (Knipovich Ridge, Mohns Ridge, ...) and transfer zones (Jan Mayen Fracture Zone, Spitzbergen FZ, ...) (see figure 2.2). The ridge vanishes under sediments close to the Laptev Shelf and its further extension is still object of current research. It seems that the ridge continues into several extensional features throughout the Laptev Sea and the coastal mountains (Gaina et al., 2002). It is the slowest Mid Oceanic Ridge with current half spreading rates of 3 mm at the Laptev Sea and up to 7 mm in the Fram Strait (Michael et al., 2003). Peculiarities of Gakkel Ridge will be explained in a extra section in more detail (see below).

Lomonosov Ridge (LR) borders the Eurasia Basin throughout the whole polar sea from Greenland to the New Siberian Islands. It is assumed, that LR was once connected to the Kara and Barents Shelf prior to the opening of the Eurasia Basin. Under roughly 500 m of marine sediments lies consolidated terrestrial material of mesozoic age. The Eurasian side of the ridge shows typical half graben and extensional structures associated with rift systems (Weigelt, 1998).

The Arctic Ocean has only two openings to the adjacent oceans. These are the narrow Bering Strait between Alaska and Russia and the Norwegian Greenland Sea. There, the main water

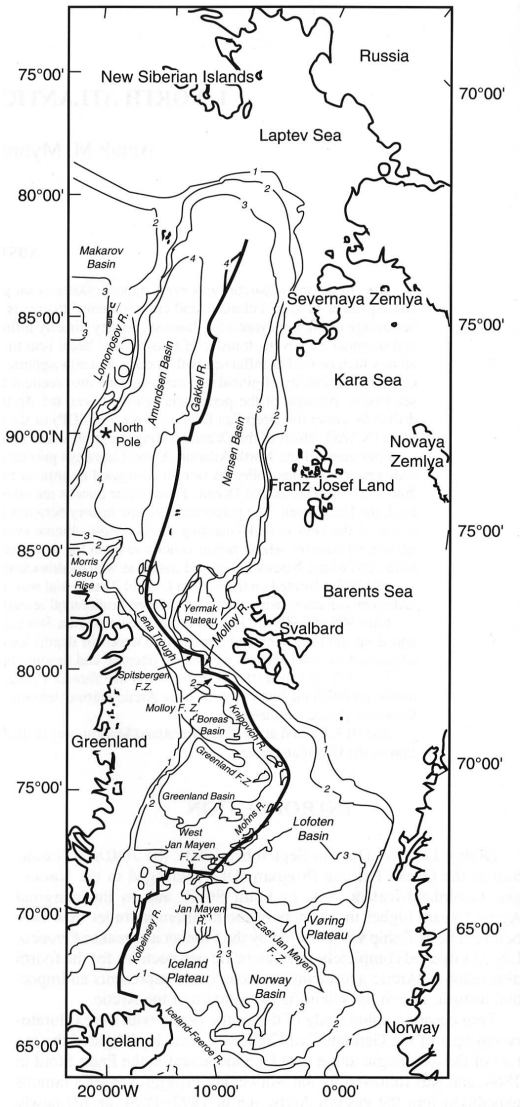

Figure 2.2: Overview map, showing the linkage between the Atlantic- and Arctic Ridge systems (Myhre and Thiede, 1995).

exchange happens thought the Fram Strait between Svalbard and Greenland, which is the only deep water passage out of the Arctic Ocean (Lena Trough). The supply of freshwater comes from a huge catchment area on the surrounding continents, drained by huge rivers like Lena or Ob. These rivers are a major sediment source. In addition, a huge sedimentary input and distribution is given by the transport of sediments trapped in ice floes. The ice floes freeze to the riverbanks or to the flat shelf regions in winter and carry on attached sediments when they break apart in spring. When they melt, they release their freight, including huge dropstones weighting up to several hundred kilos. The ice floes in the Arctic Seas can reach ages up to three years, until they are transported out of the Fram Strait into warmer regions by the Transpolar Current. This process was already described by Kiær (1906), a member of the famous Norwegian North Polar Expedition 1893 - 1896 under the leadership of Fridtjof Nansen.

Sometimes it is referred to left, right, top or bottom of maps or figures instead of the cartographic nomenclature (west, east,...). This is due to the geographical position close to the north pole, where south can have any direction.

2.2 Tectonic evolution

The existence of a mid ocean ridge system in the Arctic Ocean was first postulated by Heezen and Ewing (1961) after the analysis of a few earthquake epicenters and reevaluation of scattered Soviet depth soundings in 1961 and was confirmed by following aerogeophysical surveys (Kristoffersen, 1990). The found magnetic anomaly pattern unveiled a relatively simple spreading history of the Eurasian Basin (ridge parallel spreading anomalies), compared to the other ocean basins in the polar sea.

The initial rifting at the yet to be Gakkel Ridge started around 60 Myrs ago. The first seafloor spreading occurred about 53-56 Myrs ago, fixed by the oldest identified magnetic anomaly, chron 24 (Vogt et al., 1979) (more on magnetic chrons see below). A reconstruction with six time slices is shown in figure 2.3 by Kristoffersen (1990) giving a rough overview of the tectonic evolution.

Clearly visible is the relative uniform opening of the basin. The major changes can be seen at the bottom of the figures in the separation of Svalbard and Ellesmere Island from the greenlandic coast along strike slip faults, De Geer and Wegener fault, respectively. Greenland acts as a separate plate, bordered by rift zones to the southwest and southeast, opening the Labrador and Greenland - Norwegian Sea. In the early Oligocene, spreading in the Labrador Sea stops and Greenland is attached to the American Plate. A linked Yermak Plateau and Morris Jesup Rise are build up and subsequently rifted apart, creating the early Fram Strait. Strike slip motion along the Spitzbergen Fracture Zone connects the Knipovich Ridge with the Arctic Mid Ocean Ridge (see figure 2.2), leading to the present day situation.

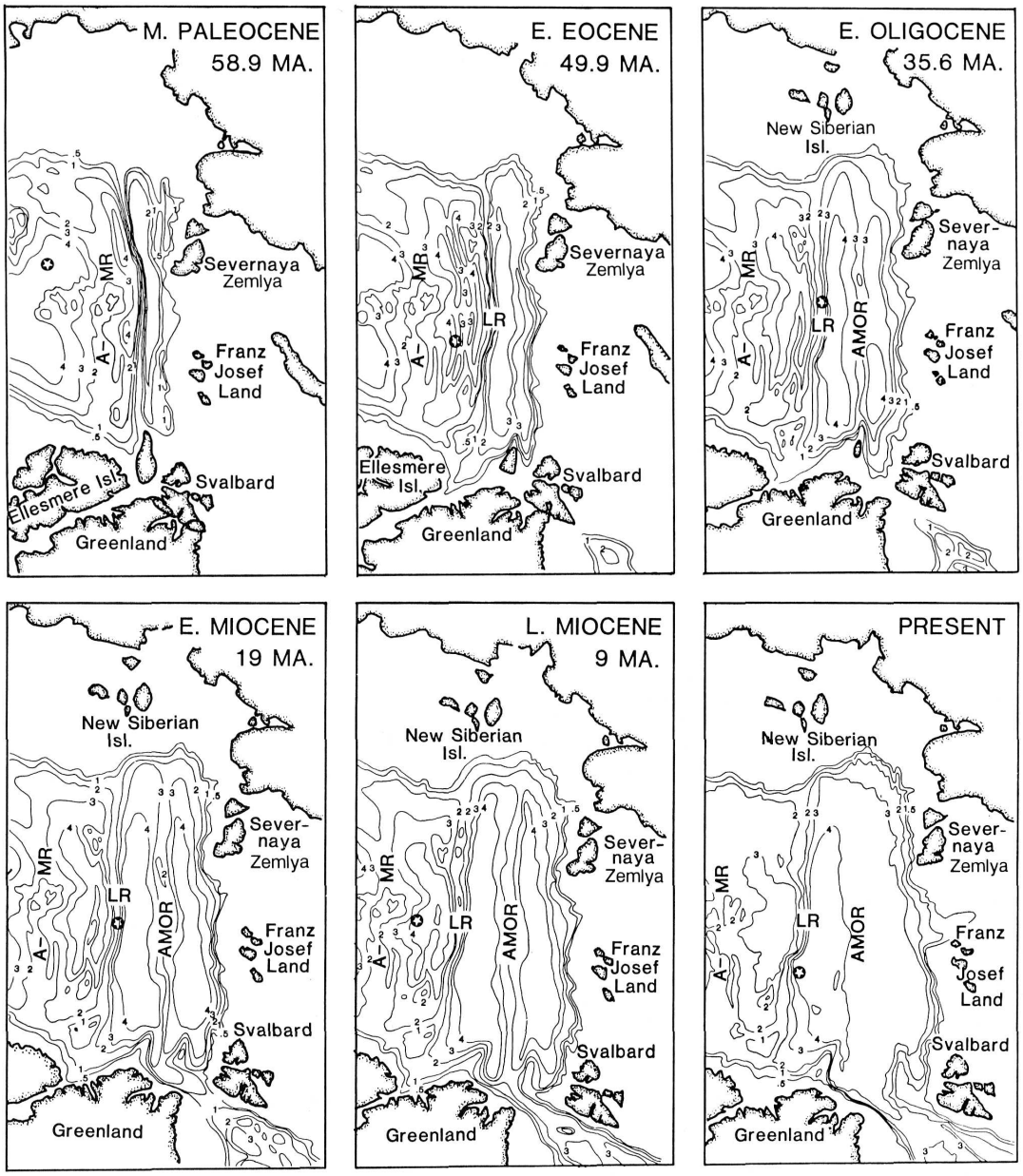

Figure 2.3: Tectonic evolution of Gakkel Ridge over the past 60 Myrs (Kristoffersen, 1990). A-MR stands for the Alpha-Mendeleev Ridge, LR for Lomonosov Ridge and AMOR for Arctic Mid Ocean Ridge. See also figure 2.1 for present situation. The star marks the position of the north pole.

2.3 The structure of Gakkel Ridge

The current structure and spreading regime of Gakkel Ridge is important to know in view of the adjacent basins, because they preserve the conditions at the ride axis from former times. The unique features explained below, may have varied along axis, but since Gakkel Ridge always showed slow spreading rates, it is assumed that the current findings of the ridge are representative. A small asymmetric spreading was detected by Vogt et al. (1979).

Following paragraphs summarize some main aspects from recent geophysical and petrological publications on Gakkel Ridge in Nature, vol. 423, 2003, by Jokat et al. and Michael et al..

The ultra slow spreading rates of Gakkel Ridge (GR) were associated with only little volcanism and most new crustal material should therefore be created by accretionary processes of asthenospheric material. Dredging operations should foster mainly peridotites. Instead, zones of high volcanic activity were found during the AMORE cruise. They were mapped by dredging fresh, glassy basalts from recent lava flows or by the localization of hydrothermal plumes in the water column. Mantle peridotites were found directly at the ridge axis in a broad zone that completely lacks magmatism.

It was found, that these zones differ in morphology, if compared in the detailed bathymetric chart, acquired alongside. The covered area was divided in three sections, western and eastern volcanic zones with a sparsely magmatic zone in between. The axial valley of GR is strikingly deep (sometimes >5 km), the deepest of the worldwide oceanic spreading centers. No major fracture zones offsetting the ridge axis were found, similar to the findings on the ultra slow spreading South West Indian Ridge (Dick et al., 2003). The eastern parts of the ridge contain more sediments than the western parts, where only a thin veneer of sediments is found. These features coincide with findings from potential field measurements (gravimetry and magnetics) visible in a new compiled map by Brozena et al. (2003).

In currently accepted models, crustal thickness should diminish with decreasing spreading rates. Fast ridges produce more melt and therefore generate more volcanism, resulting in thick basaltic and gabbroic layers. At GR, exceptionally thin crust was found, between 1.9 - 3.3 km, compared to the rather usual value of approx. 7 km found on faster ridges. The local findings of fresh peridotites at the ridge axis indicate no oceanic crust there at all.

Strongly focused volcanism in some parts of the rift valley creates basement ridges perpendicular to the axis, that can be followed in the IBCAO bathymetric chart (Jakobsson et al., 2000) until they vanish under the sediments. They seem to be active for several million years, sustained by the acquired helicopter based, magnetic surveys, conducted during the experiment. Older features of the same origin may be visible in the seismic data, displayed later, as prominent basement highs or partly buried seamounts, which bias the subsidence of the basement and the crustal roughness as shown in following calculations in this thesis (see figure 2.4 for additional information).

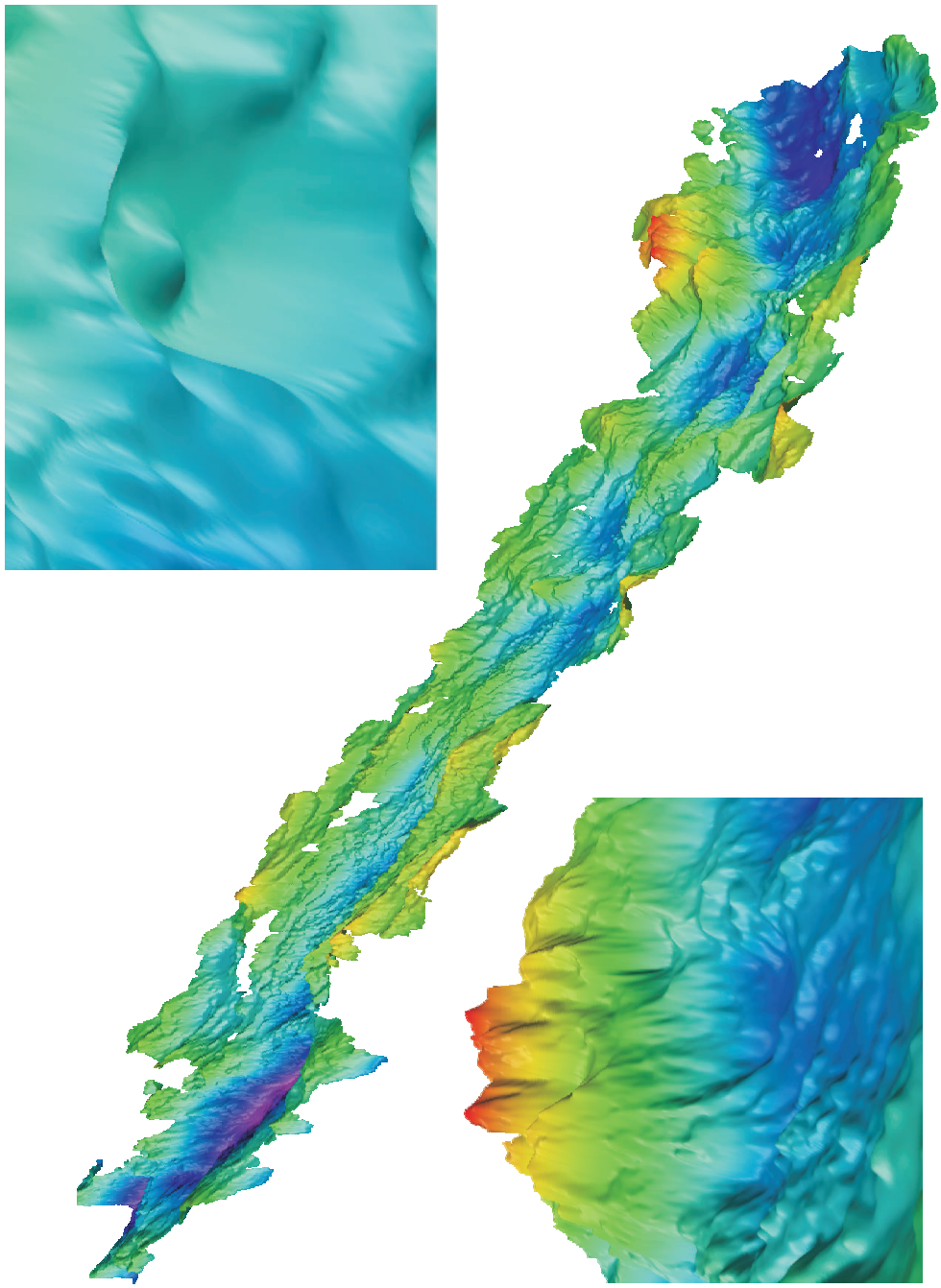

Figure 2.4: Detailed bathymetric chart of the western volcanic zone, blue colors stand for great depths (the picture should be viewed in landscape mode). The viewing angle on the ridge is from the Alaskan-Canadian side, similar as in figure 2.1. The right side of the picture shows the entrance of Lena Trough in the Fram Strait (4500 m), the beginning of the deep valley on the left side (blue to violet colors, +5000 m) marks the transition to the sparsely magmatic zone. Rifting structures are visible in the axial valley (approx. 3000m) as lineations in strike direction. The valley floor is dotted with a vast number of volcanic cones, a real nice exemplar is shown in the upper right. The lower left inset shows the prominent seamount visible above the entrance of Lena Trough. Here, the small blobs on the valley floor seem to be volcanoes as well, the seamount itself is rifted apart by the ridge (Gauger, 2002).

3 Data acquisition

The following sections describe the data acquisition, the technical set up and the problems of marine geophysics, especially in ice covered regions. For the basics of reflection and refraction seismic theory the reader is referred to standard literature like Kerz (1992), Berckhemer (1997), Telford et al. (1985), Palmer (1986), Robinson and Çoruh (1988). For a specific introduction to marine geophysics Jones (1999) is highly recommended.

3.1 Reflection seismic

Marine seismic surveys require basically a source creating pressure waves in the water and a chain of hydrophones (streamer) towed behind the ship. Both exist in various designs and sizes. Because there are no topographic obstacles like towns or mountains, marine seismic surveying can be carried out in a very effective way and is highly productive.

Industrial surveys for oil and gas exploration may use 8 or more digital streamers towed in parallel, each up to 12 km long or even ocean bottom cables (receivers, that are lowered down to the seafloor). These streamers communicate and adjust their relative positions using ultrasonic signals and a set of 'birds' (depth controlling system) and floating buoys with GPS sensors attached. The sources range from 'sparkers', electrical devices that generate high-frequency signals (1 kHz) to massive, large volume airguns with chamber capacities of 60 - 100 l that generate low frequencies (10 - 20 Hz). Also, arrays of airguns may be used, meaning several airguns are clustered together to increase energy and enhance the signal. Sometimes, a system of two ships is used, one towing the source, the other towing the receiver equipment. This arrangement results in very complex shot-receiver geometries and excellent data coverage. It seems, that the limit for industrial exploration is only given through too narrow seas for tuning circles to revert course.

Scientific polar research is not only limited in funding compared with the exploration industry, but also has to cope with the ice coverage of the polar seas, and therefore it has to be creative in design and accept cutbacks in data quality and areal coverage.

3.1.1 The source

Most marine profiles are acquired with airguns. These devices are made of high quality steel and consist mainly of two air chambers that are sealed with a double-ended piston (see figure 3.1). Pressurized air enters chamber A through a vent and is conducted to chamber B through a channel in the axis of the piston. As the area of flange X is greater than the area of flange Y, the piston is is held firmly in place by the compressed air due to unbalanced downward and upward forces. The seals of the airgun consist of O-rings and can be seen as black dots in the shown cross section. After an electronic trigger signal, the solenoid valve opens a passage and air reaches the underside of flange X. This additional upward force is sufficient to override the downward force and causes the piston to retract rapidly into chamber A. This releases the trapped air in the lower chamber through the portholes. The pressure in chamber A increases, which slows the moving piston and slams it down again in its initial position. Through the constant supply of air, chamber B is refilled and the firing cycle can start again. The release of the air happens within 4 ms, the reloading with air needs 25 ms to 40 ms (Sheriff and Geldart, 1986).

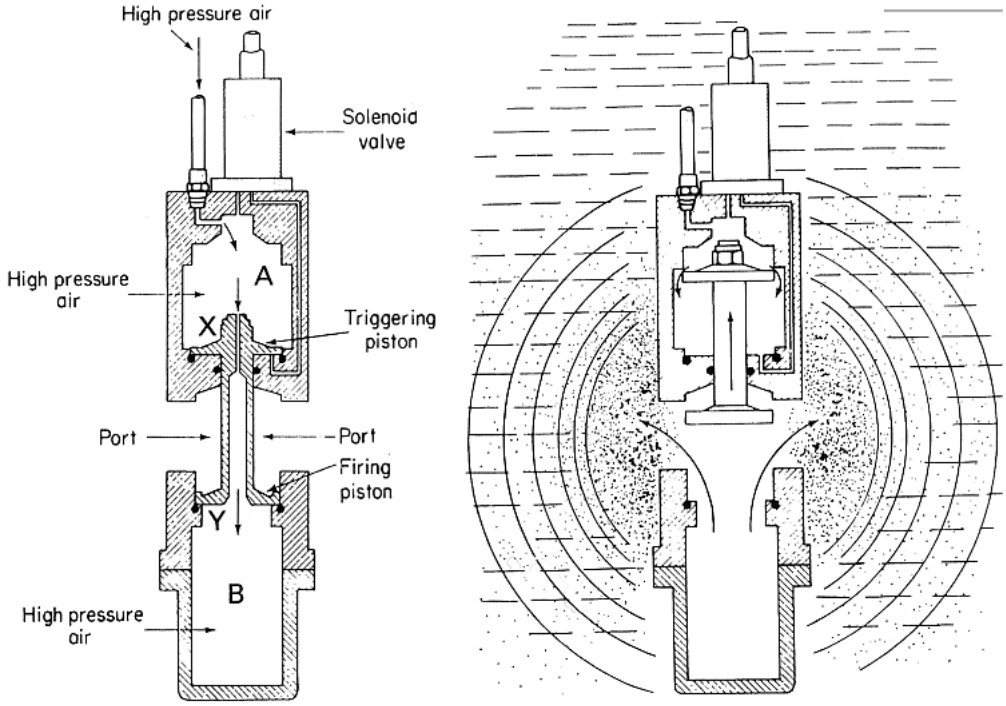

Figure 3.1: Cross section of a VLF (very low frequency) airgun, pressurized (left) and during the release of air (right) (Jones, 1999)

The power specification of the compressor (volume of pressurized air delivered in a given time), the shooting pressure and the volume of the airguns limit the range of possible shot intervals technically. The shot interval is also set by the operator, dependent on the energy of the source and therefore its penetration. No destructive interferences of two shots are wanted in

the data. So, subsequent shots can only be triggered after several seconds, when the seismic energy is dissipated enough.

AWI's preferred source for long transects in dense ice cover is a cluster of 8 VLF - airguns, manufactured by Prakla-Seismos, working like explained above. These guns are very reliable, easy to maintain and can be repaired very fast, if vents or O-ring seals are broken. They can be handled by one or two persons and no special tools are needed. Each gun has an air chamber volume of 3 liters (24 l in total), and was fired every 15 seconds with a target pressure of 120 bar during the AMORE cruise. The generated frequencies range up to 120 Hz, but the main frequencies are situated around 40 - 50 Hz (Jokat et al., 1992).

3.1.2 The airgun array

After the ship breaks the ice floes, a narrow and sometimes fast closing channel is opened up behind it. It would be risky to tow the guns in single file behind the ship because the air hoses and electrical trigger cables are exposed to the still big ice fragments and in risk to be cut. Also, losing of a complete gun or even more gear is possible. A special heavy, rigid steel frame, which is towed only about 10 m behind the ships stern was developed to protect the seismic equipment (Jokat et al., 1994). The 8 airguns are attached with steel chains in two rows underneath the frame. The hoses and cables for each gun are fixed and protected by rubber casings and lots of heavy-duty tape to permit only limited movement during the heavy discharge of air. The whole thread is protected by a thick hard rubber tube, leading to the ship (see figure 3.2). The array is stabilized by two floats at the rear and two steel cables fix it sideways to the stern of the ship. The array is deployed and retrieved using the ships A-frame winch. The depth of the source ranges between about 5 and 10 m, depending on the ships speed.

Despite these tight measures, the array can still be exposed to the forces of the ice, especially during turns of the ship when the array starts to drift sideways. Sometimes large blocks of ice (up to 3 x 2 x 1.5 m) get trapped between the array and the ship and a ripping of supply cables is possible. Cables can also be damaged by abrasion with their neighbors and the steel frame during the airgun bursts. If airguns fail due to a pressure leak in the cables or a broken O-ring it is for the chief scientist to decide whether to stop shooting and repair or to go on. Usually, the 'loss' of one airgun is acceptable.

3.1.3 The streamer

A common streamer consists of a lead-in cable, stretch sections, an active section and a tail section with a buoy attached to the end. Usually these parts are divided in smaller sections again to allow a modular set up and a easy exchange of damaged sections. Only the lead-in

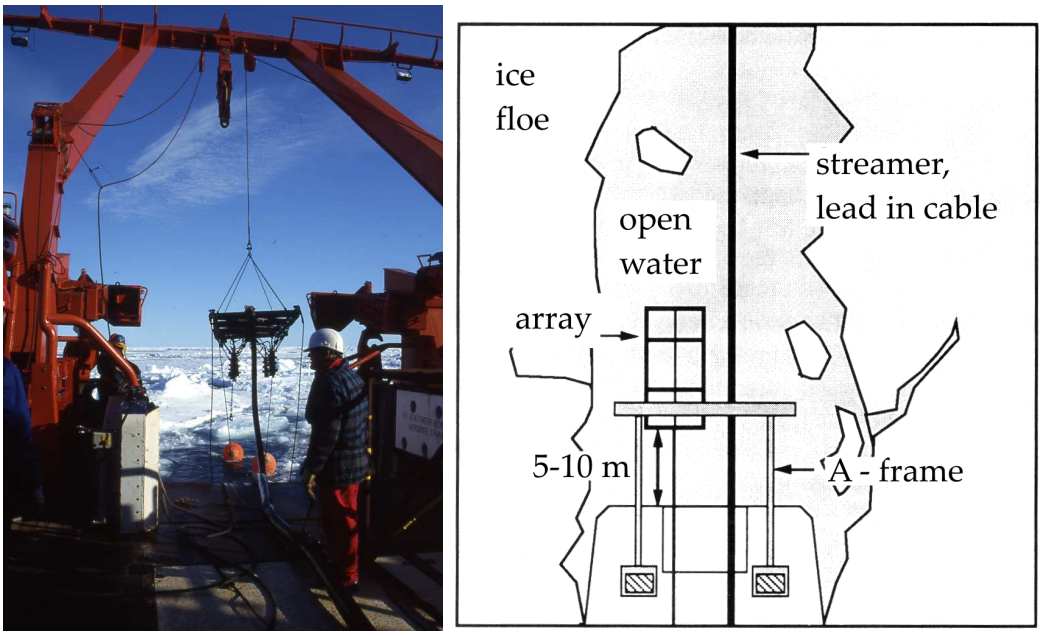

Figure 3.2: Airgun array, ready for lowering into the water and sketch as seen from above. Note the dense ice cover behind the array (sketch taken from Hübscher (1994)).

cable is made of steel wire to guard the supply and recording cables next to the airguns and to provide a certain offset of the receivers (see figure 3.3).

The further sections consist of a plastic tube (about 10 cm in diameter) which is filled with oil to provide a neutral buoyancy and a strength member to accommodate towing strains (Jones, 1999). The oil has an acoustic impedance close to that of seawater. The stretch sections act as a sort of spring, to damp the effects of the ships motion, i.e. by waves. Active sections include hydrophones made of a piezoelectric material which converts pressure fluctuations into a proportional voltage. Several hydrophones are connected in parallel to be less affected by noise and act as a hydrophone group (referred to as a channel or receiver later on). After the active sections, stretch sections can be inserted again to damp disturbances from the tail buoy. Streamers may also use a depth control system, which is called 'birds'. These birds are a set of wings attached to the streamer, their angle of incidence can be controlled from the ship according to the data from depth sensors. The seismic data can also be converted from analogue signals to digital data in the streamer sections and may then also be transferred with fibre optics to the recording unit, to cope with transmitting losses through plain cables.

The used streamer configuration during the AMORE cruise was an analogue streamer without birds or depth sensors attached, manufactured by Syntron. The use of an end buoy as depth and position control was impossible, again, due to the ice conditions. The dense ice coverage permitted a total streamer length of just 480 m (180 m lead in and stretch sections, one 300m active section) and 48 channels. Even so, the data show that the streamer had occasional contact with ice and was not always floating freely. Because of this, anything attached to the

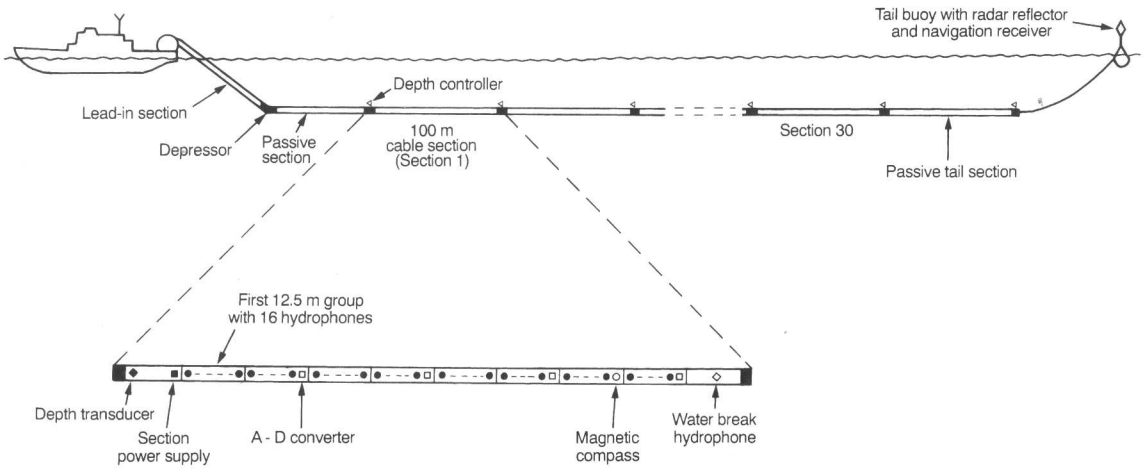

Figure 3.3: Sketch of a high end digital streamer with depth controllers and tail buoy (Jones, 1999)

streamer would be ripped off (i.e. birds) and could lead to the complete or partial loss of the streamer itself. The depth of the streamer should range between 15 m to 20 m, a constant ship speed provided. During turns, the streamer sinks without any depth control to countersteer. Sinking can also lead to damage due to the water pressure weighting heavily on the plastic tube and hydrophones. Sinking also happens during the slowing of the ship when it encounters thicker and bigger ice floes or ice ridges and give rise to to disturbed data (see below).

The worst case for geophysical profiling is, when the ship gets stuck in the ice and must reverse in order to perform ramming operations. All the gear must be put on deck, to avoid its entanglement in the ship's propeller. This time is used also for repairs of the equipment, but results in data loss too, since the tight schedule must be kept and profiling is not started again at the point of termination after a passage is cleared. To minimize the risk of these interruptions, the two ship setup with USCGC Healy was used.

3.1.4 Recording unit

The received signals from the streamer were recorded with a registry unit (ES-2420) manufactured by Eg&G GEOMETRICS. The time, essential for the recording and exact trigger impulses for the airguns is provided by a Meinberg satellite clock (see figure 3.4). A record length of 12 seconds was used.

An anti-alias filter was applied to suppress frequencies above the Nyquist frequency of 180 Hz. Afterwards, the data was digitized with a sample rate of 2 ms and written to magnetic field tapes in SEG-D format with a capacity of 250 Mb. The small tape units are selected for security reasons. If a tape gets damaged before demultiplexing and copying, only half an hour of data is lost.

For online quality control, a thermal printer plots one channel of the data. This also provides a first glance at the new data with the opportunity for a first visual comparison with existing gravity, magnetic or sedimentary maps.

Figure 3.4: Recording room, where a lot of seismic watches were spend.

Figure 3.4 shows the technical devices necessary to control the equipment and record the data. Starting from left to right, the first two racks control the airguns and streamer. The grey boxes with the black covers are the registry unit, where all data (reflection and sonobuoy data) are multiplexed and digitized. The oscillograph next to the GEOMETRICS is used for monitoring the electrical return signals from the airguns. On the right-hand side, the tape recording devices are visible with the GPS clock on top. Everything is firmly lashed in case of stormy weather during transit or movement caused but the ice.

3.1.5 Noise

Normal static white noise is superimposed on the wanted reflection impulses with several distinct frequencies. Noise can be 'natural' or generated by the survey team and equipment. The main marine noise sources are listed below:

- Noise from the ship itself, especially originating from the ships propeller and engine. This can be mitigated by trailing the streamer far behind the ship and/or by reducing the ships speed, both within practical limits (Robinson and Çoruh, 1988). The main frequency of the propellers of RV Polarstern is around 11 Hz (Jokat et al., 1992).

- Noise generated through the pitch and roll movements of the ship by wave motion forwarded to the streamer. This is minimized through the stretch sections in the streamer. Due to the ice coverage in the high polar seas, waves are almost nonexistent. Instead, ice breaking generates very jerky and erratic movements of the ship. These movements have low frequency spectra and are of no real concern due to the stretch sections. If ice gets trapped between the propeller and its steel casing for a focused thrust, violent vibrations with relatively high frequencies are generated until the propeller shredders the ice. These should also not have any effect on the data.

- Noise from the surf in costal areas results usually in high frequencies (+200 Hz), but could be neglected too, due to the absence of costal regions in the survey area.

- Noise generated by contact between the streamer and ice is much more relevant. This results in in noisy data or clipped sections, depending on the force of the contact. Here, all frequencies are possible.

- Coherent noise caused by short shot intervals ranges usually in the frequency band of the desired frequencies (Herber et al., 1997).

- The seismic sources are not free from noise generation, either. The main problem here is the 'bubble' (see section below) or broken seals, etc. leading to a bad seismic signal.

3.1.6 Bubble and Ghost

As the airgun releases its charge in the water, the accelerated air expands over the equilibrium of water and air bubble, due to its inertia. This creates a low pressure in the bubble, forcing it to collapse, which in turn gives rise to an overburden pressure inside of it. These reverberations continue until balance is reached, or the bubble reaches the surface. The oscillating bubble acts as a new source (bubble pulse), smearing the wanted 'spiked' pulse from the airguns. The oscillating frequency is in the range of the wanted response signal and creates multiple reflection of a horizon in the range of some milliseconds. In figure 3.5, the primary wave is marked with P and the first bubble impulse marked with B. After about 150 ms a second bubble event is visible at 0.3 s.

Solutions to minimize bubble effects are a well thought out airgun arrangement and triggering sequences (different air volumes and delayed shot times) or improvements of the airgun design. For example, GI guns from Sodera release several bursts of air in a short succession at the points of bubble collapse, so the bubble expands continuously. The bubble signature in the

data can also be removed through processing, but this wasn't done here due to time and objectives of the thesis.

The multitude of peaks inside the first bubble pulse may also be the result of reflections from the hull of R/V Polarstern with the corresponding surface reflection, because the array is towed closely behind the ship. The body of the ship starts to reverberate and so, acts as emitter of new impulses, broadening the signal. This effect must be accepted as another of the complications caused by working in ice covered regions.

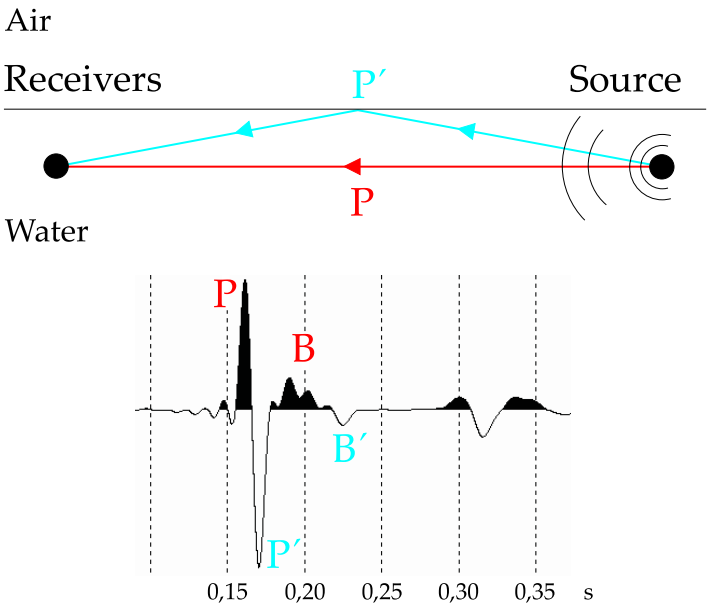

Figure 3.5: Bubble and ghost examples shown in the direct wave. P stands for the Primary pulse and B for the bubble pulse. P' and B' represent the surface reflection (ghost).

Ghosts in the seismic data originate from reflections of the seismic waves at the sea surface. When the wave is reflected at the water-air boundary, its phase is shifted by π, since the angle of incidence is almost vertical at the sea surface, and the refection coefficient is -1 (see figure 3.5). The ghost arrives at the hydrophones some ms later than the corresponding wave following a 'direct' path.

3.1.7 Streamer depth variations

Neutral buoyancy of the streamer occurs at a certain depth, adjustable with the fill level of the streamer oil, and no acceleration present. If towed, the streamer is sensitive to changes in the ship's speed due to varying ice coverage. It starts to sink if slowed down and rises again when the speed is increased. This results in lens-shaped distortions in the data (see figure 3.6). The upward and downward movement of the streamer changes the traveltime geometry of the waves and their corresponding ghost. When the streamer is sinking, the traveltime of

the seafloor reflection decreases, and the traveltime of the ghost reflection from the seafloor (travel path: source→ seafloor→ water surface→ receiver) increases, creating the lens.

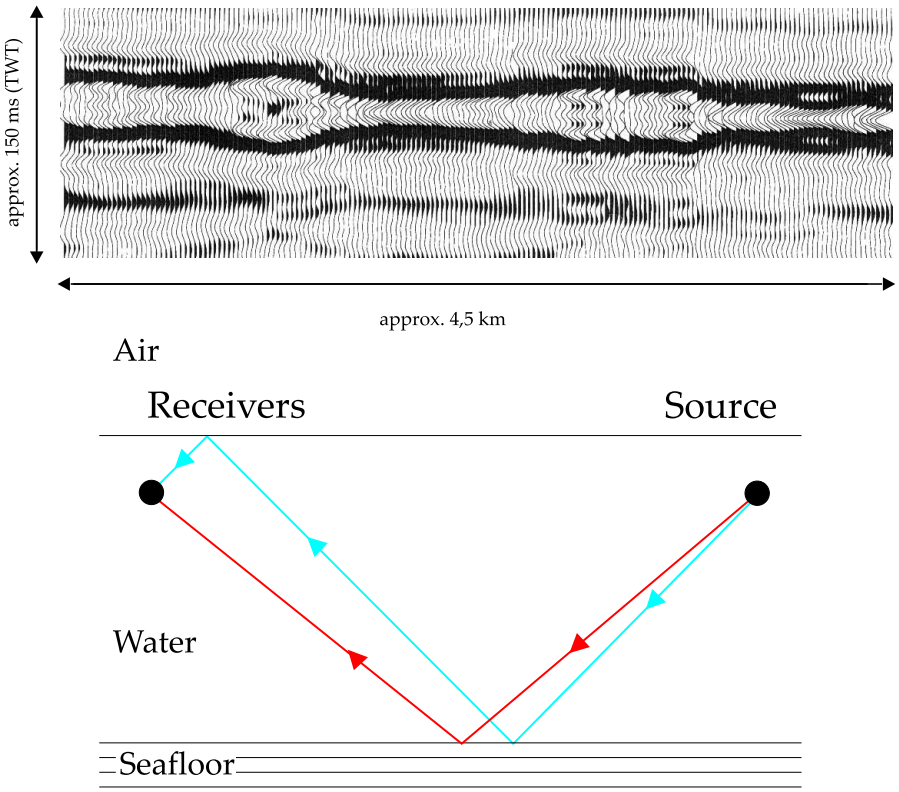

Figure 3.6: Detail of the seafloor reflection with lenses caused by ghosts due to streamer variations and a possible travel path geometry, shown underneath.

Since it was not possible to use a depth controlling system, the streamer's position and its behavior during accelerations, and therefore of the receivers too, is not known at first hand. These time-variant changes of the experiment setup could be included in the normal geometric settings for data processing.

Several approaches to overcome these problems have been tried by Weigelt (1998), but no solution has yet been found. In my opinion, a detailed model of streamer movements must be made first, instead of working on the already 'bad' data for correction. Such modelling could make use of the logs of seawater salinity, density, temperature written in the ship's database system (PODAS) as well as the speed and position. With a streamer behavior model, seismic data could be generated for real cruise parameters (velocity, etc.) and could be compared with the acquired data.

Reflectors can still be distinguished and followed, because the lenses are only local features. Problems caused by these lenses can occur during migration or detailed analysis of the data for BSR, fluid convection, small scaled faults or reservoir possibilities for gas or oil.

3.2 Refraction seismic

The same source configuration was used for refraction experiments along the reflection seismic transects. No refracted arrivals could be extracted from the streamer because of its limited length. In water-depths of approx. 4 km, the first refracted phases show up at offsets of 13 km. Only long wavelength signals have enough energy to be detected at such far offsets. They are less disturbed by small scale variations in the ground than high frequency signals. To record refracted phases, sonobuoys were simply dropped in the water behind the ship.

3.2.1 Sonobuoys

The sonobuoys consist mainly of a hydrophone and a data processing and transmitting unit and were manufactured at AWI (see figure 3.7). The hydrophone is submerged at a minimum depth of 10 m, the buoy floats at the water surface. The received signals are transmitted via radio waves to antennas on the ship and recorded along with the reflection data. The maximum useful offsets for the seismic data range between 20 - 30 km. At this far offsets, the seismic signal is very weak and can not be distinguished from normal static noise any more. A small hole in the casing of the buoy is blocked by a salt tablet which dissolves after some hours and the buoy sinks to the seafloor. The low coast of the system do not justify the time to haul in the airguns and streamer and reverse the course to search for the buoy, since no positioning or retrieval system is built in. The buoy drifts with the ice due to water currents and wind.

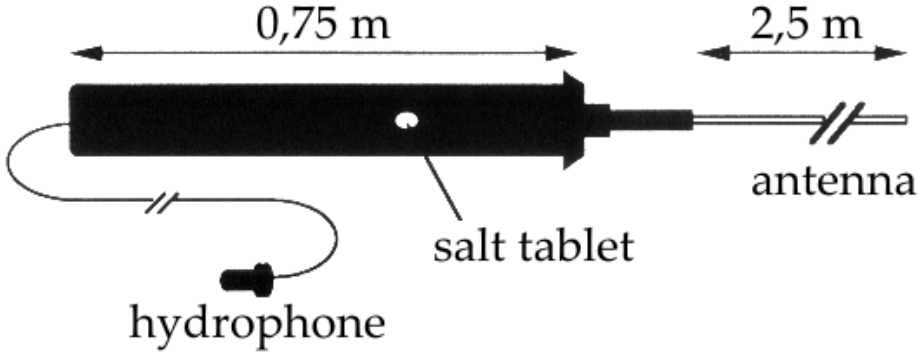

Figure 3.7: Sketch of a sonobuoy (Hübscher, 1994).

3.2.2 Ref-Tek stations

In the Amundsen Basin, two additional Ref-Tek stations were deployed on ice floes with the onboard helicopters. These systems consist of a data logger with several channels, a hard-disk and a GPS antenna for position and time. Two channels were used with 8 geophone

chains each. Each chain contains 6 vertical component geophones. The multitude of receivers enhance the data, since the signals received from the airguns are added up (they have all the same shape) and the static noise on the receivers interferes destructive (increase of the signal to noise ratio). A pattern of the chains was spread out around the data logger and covered with snow to minimize noise created by wind and weather, shaking the cables. The distances between the spread geophones is of no concern, because of the long wavelengths of the signals.

Figure 3.8: The setup of a Ref-Tek station on a foggy day. It seemed like gardening...

Here, retrieval is critical, if the ice floe drifts for greater distances. All the equipment fits inside a standard Zarges box, making it difficult to locate the gear from the helicopter without additional help. A radio beacon was set next to the station to locate it with sounding equipment. Also, a visual backup system was provided. Nautical distress signals (smoke bombs) could be triggered remotely from the helicopter, if necessary.

High frequency noise is not critical for refraction data, because the wanted signals range around 20 Hz. Higher frequencies (above 30 Hz) will be filtered from the data. Long wavelength disturbances like ocean waves or tilting movements of the ice floe are of higher concern. Additional problems are the unresolvable drift paths of the sonobuoys and the risk of annihilation of ice floe stations by the occasional polar bear.

3.3 Resolution of the seismic data

Seismic resolution is defined by how close two reflective features can be together and yet still be seen as two unique events in the data, meaning the resolvable layer thickness for example. This depends strongly of the used frequencies and therefore of the used source and energy. The results of the example calculations apply for the AMORE data.

3.3.1 Vertical resolution

According to Yilmaz (1987), a quarter of the main wavelength can be seen as a minimum distance between two reflectors to be recognized as two events. This can be altered through a noisy recording to larger ratios.

The main frequencies (f) of the the VFL-airguns range between 40 and 50 Hz. Seismic velocities (v) for sediments and basement range between 2 and approx. 5 km/s. With the following equation, this results in wavelengths (λ) between 40 and 100 m:

$$\lambda = \frac{v}{f}. \tag{3.1}$$

Therefore a best vertical resolution of 10 to 25 m is possible for the reflection seismic data. The frequencies of interest for refraction seismic data are situated around 20 Hz, resulting in wavelengths of 100 to 250 m. The resolution ranges between 25 and 62 m. For later modelling of the refraction data, layer thicknesses under 60 m must be very well constrained if they are not omitted in total.

As the seismic energy decreases with increasing depth due to inelastic damping, absorption and diffraction, the vertical resolution reduces as well (sperical divergence).

Figure 3.9 shows a model with a wedge, illustrating layer thicknesses and demonstrates the limits of vertical resolution and its dependence on wavelength. The model is convolved with a kind of ricker wavelet and the synthetic response is shown the lower part of the figure. Spikes indicate the position of the model boundaries and resemble also a single frequency source signal. At 10 ms TWT wedge thickness, the two boundaries can not be seen as separate events.

3.3.2 Horizontal resolution

The horizontal resolution also depends mainly on the frequency and is also affected by the spacing between the receivers and the covered ground between two shots.

A seismic wave front is not reflected instantaneously from one single point but instead from an area over a short time interval. Hence, signals from reflectors close-by, that come to the receiver

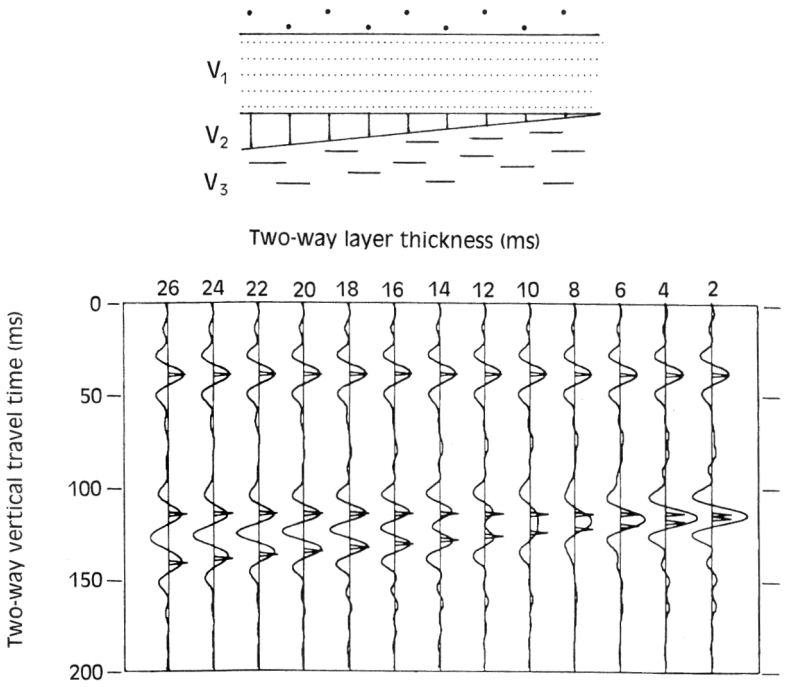

Figure 3.9: Example of the dependence of wavelength and layer thickness, the two sketches are not the same scale (Jones, 1999).

in that time-frame can't be distinguished from each other and interfere. For a given frequency, energy arriving at the receiver inside the time window resembling half of the wavelength ($\lambda/4$, one way travel time) interferes constructively and enhances the signal (Yilmaz, 1987). The area where these reflections originate is called the Fresnel zone, or first Fresnel zone (see figure 3.10) and reflections from inside that zone are not separately resolvable.

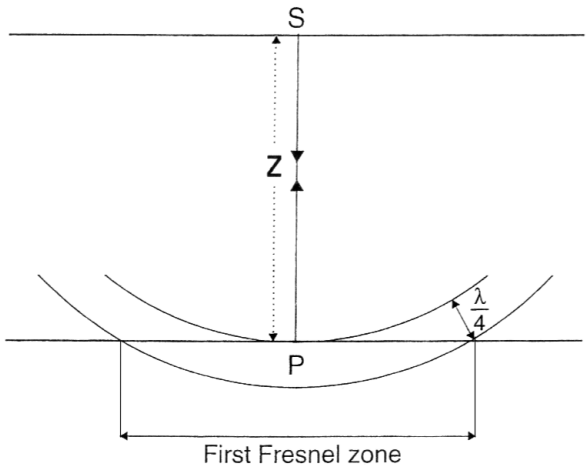

Figure 3.10: Geometry of the Fresnel zone (Jones, 1999).

High frequencies (short wavelengths) result in narrow Fresnel zones. The smaller the Fresnel zone, the easier it is to differentiate between two reflecting points. Hence, it is a measure for lateral resolution (Yilmaz, 1987).

The radius (r) of the Fresnel zone is given by Schmöller (1987), according to the following equation:

$$r_{fres} = \sqrt{\frac{1}{2}\ z \cdot \lambda} = \sqrt{\frac{1}{2}\ z\ \frac{v}{f}}, \tag{3.2}$$

in wich z is the depth of the reflector and λ the dominant signal frequency. The horizontal resolution decreases with increasing depth and with increasing wavelength.

For a 50 Hz signal the Fresnel zone amounts to 490 m at the seafloor (4000 m, v = 1.5 km/s). With a sedimentary cover of 2 km and an average velocity of 2.5 km/s, the horizontal resolution on the top of the basement is 774 m. At a frequency of 20 hz (refraction seismic) these values amount to 774 m (seafloor) and 1224 m (top of basement).

These quite large Fresnel zones result from the depth of the ocean. A means to increase lateral resolution is to tow the streamer and/or source close to the seafloor (see figure 3.11), although this requires good sounding devices to provide the positions and depths of the submerged equipment.

The shot spacing of about 40 m does not increase the resolution. The short interval is used to collect more information (better coverage) of a reflective feature, for CDP sorting and stacking, explained in the following chapter about processing.

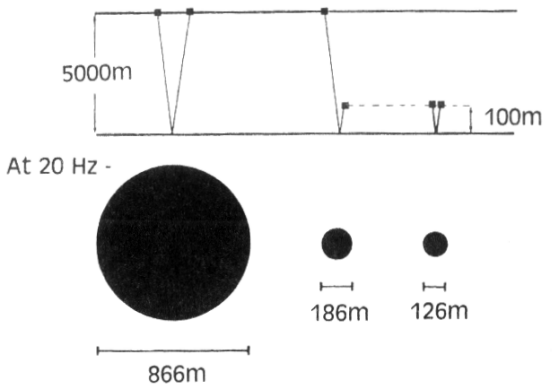

Figure 3.11: Minimizing of Fresnel zones. The black circles demonstrate the relative size for the different source receiver configurations. For the speed of sound in water a velocity of 1.5 km/s was used, the source frequency is 20 Hz (Jones, 1999)

4 Processing

The quality of 'raw' data files from the field is not sufficient enough for a geological interpretation. Therefore, a kind of standard approach is used to process seismic data (see 4.2.1). For example, the geometric settings and coordinates of the profiles must be linked to the corresponding shots, or the signal to noise ratio (SNR) can be increased by proper filtering and stacking. There are several similarities between the processing of reflection and refraction data, although, in general, processing of refraction data is less time intensive.

The goal of this processing is to obtain high quality time and depth sections of the seismic transects and a profound velocity model from the refraction data.

R/V Polarstern has an onboard processing capability, like that at at AWI in Bremerhaven, so that data quality control or first steps in the processing sequences can be done during the work of other research groups or transit time.

For more detailed information on data processing than that given below, the reader is referred to books and papers by like Yilmaz (1987), Yilmaz (2001), Sheriff and Geldart (1986) and articles of Forkmann and Weber in Militzer and Weber (1987). The books on geophysics and processing published by the American Association of Petroleum Geologists (AAPG) (Beaumont and Foster, 1988), also provide a good overview.

4.1 Software

The Software used on R/V Polarstern and at AWI to process seismic data consists of a script-based industrial programm called DISCO and its interactive version FOCUS. The jobs created with FOCUS resemble the format DISCO uses and vice versa, so that they can be called from both programs. All information related to a singe profile like names, setup, processing parameters, mutes and velocity models are stored in a seismic database, and can be called conveniently from each module inside FOCUS or DISCO. In addition several UNIX based programs for editing source code or sorting lists, like AWK, or GMT to create maps of the profiles, are used extensively. Examples of DISCO code and FOCUS are shown in the following figures of this chapter.

4.2 Reflection seismic

4.2.1 Processing sequence

Raw data

⇓

Demultiplexing

⇓

Geometric definition

⇓

CDP sorting

⇓

Editing

⇓

Filtering

⇓

Spherical divergence correction

⇓

Velocity analysis

⇓

NMO correction

⇓

Stacking

⇓

Muting

⇓

AGC and final stacks for further interpretation

4.2.2 Demultiplexing and geometric definition

The field data tapes must be demultiplexed and tied to the navigation data like water depth, cruising speed, course, heading and latitude/longitude positions. A list with entries for each shot with corresponding positions, etc. is created.

During demultiplexing, the time sequences from the tape are resorted to channel sequences for each shot, called shot-gather (see figure 4.1). With a supposed mean cruising speed of 5 kn during profiling (about 9 km/h) and a shot interval of 15 s, the shotpoint spacing is approximately 38 m.

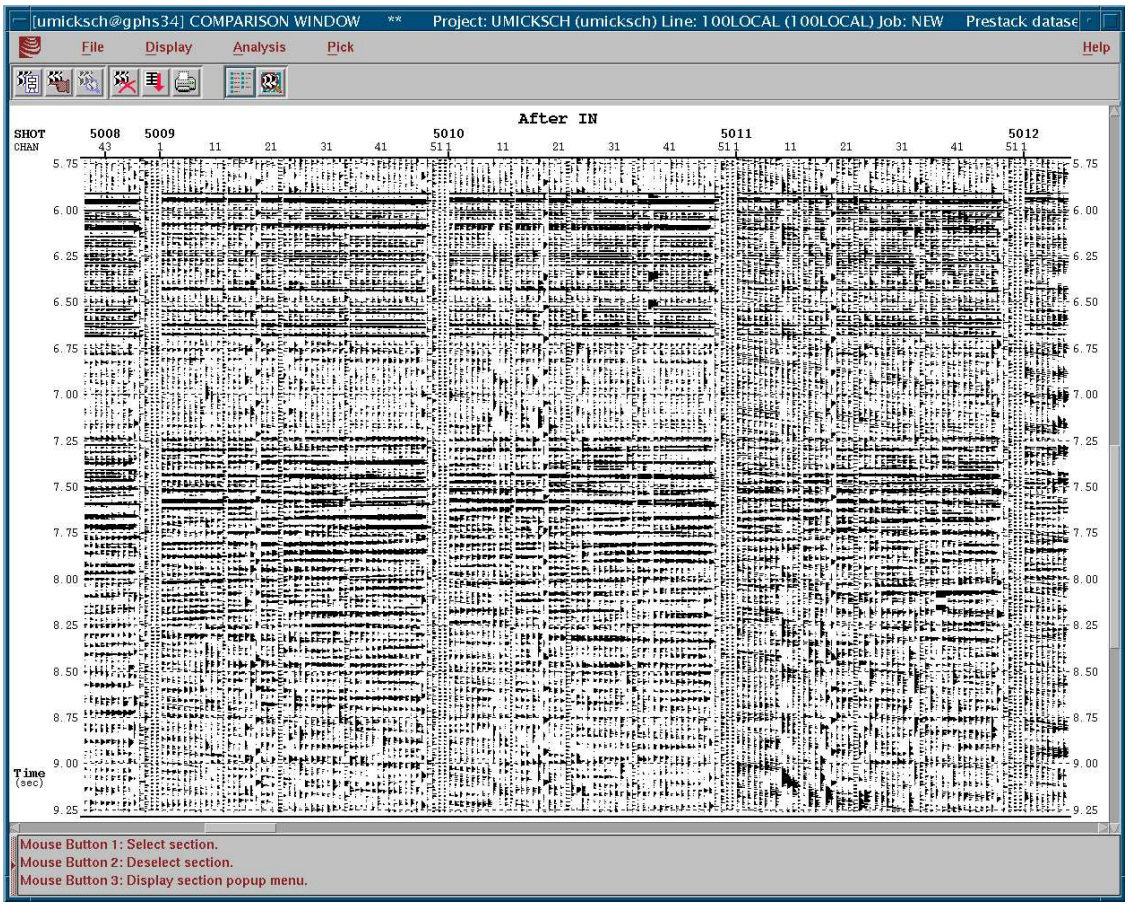

Figure 4.1: Shot-gathers of profile 300 showing raw unfiltered data. The gather on the right side is more noisy than the others, especially for the first 10 channels. This is due to a possible contact of the streamer with ice floes.

4.2.3 CDP sorting

As the ship and the 'recording unit' move along the profile, different receivers in the streamer collect data from the same locations at depth (see figure 4.2). These 'depth points' are imaged repeatedly, the number of repetitions depends on the experimental setup. For each shot, the length of the imaged line is half the length of the active streamer section, assuming a horizontal layering.

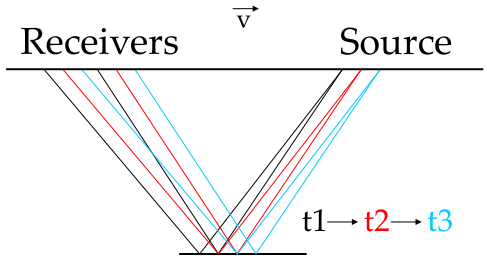

Figure 4.2: Sketch of the shot - receiver geometry

Since we know the geometric settings, we can merge the data channels into groups with the same point of reflection, called common depth points (CDP). Strictly speaking, this is only valid for horizontal layering. With dipping layers, one gets information of a common reflection surface, CRS (see figure 4.3), and gets a common midpoint. CDPs are a special case of CMPs.

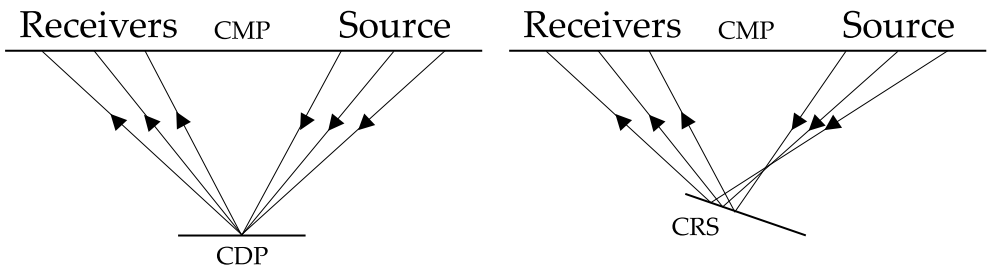

Figure 4.3: CDP vs. CMP

In this study, gathering the traces with a constant CDP spacing of 25 m results in a CDP fold of about 25, meaning 25 receivers build a CDP-gather. Variations in the folding (± 5) for each CDP result from variations in the speed of the ship during icebreaking. A data example is shown in figure 4.4

4.2.4 Editing

After CDP-sorting, the gathers are visually checked to find bad traces, which have to be removed to prevent a destructive interference of the data during stacking.

If the weather was suitable during seismic profiling helicopter-based work was done, for example magnetic measurements. This meant, that the ship had to deviate its course to turn

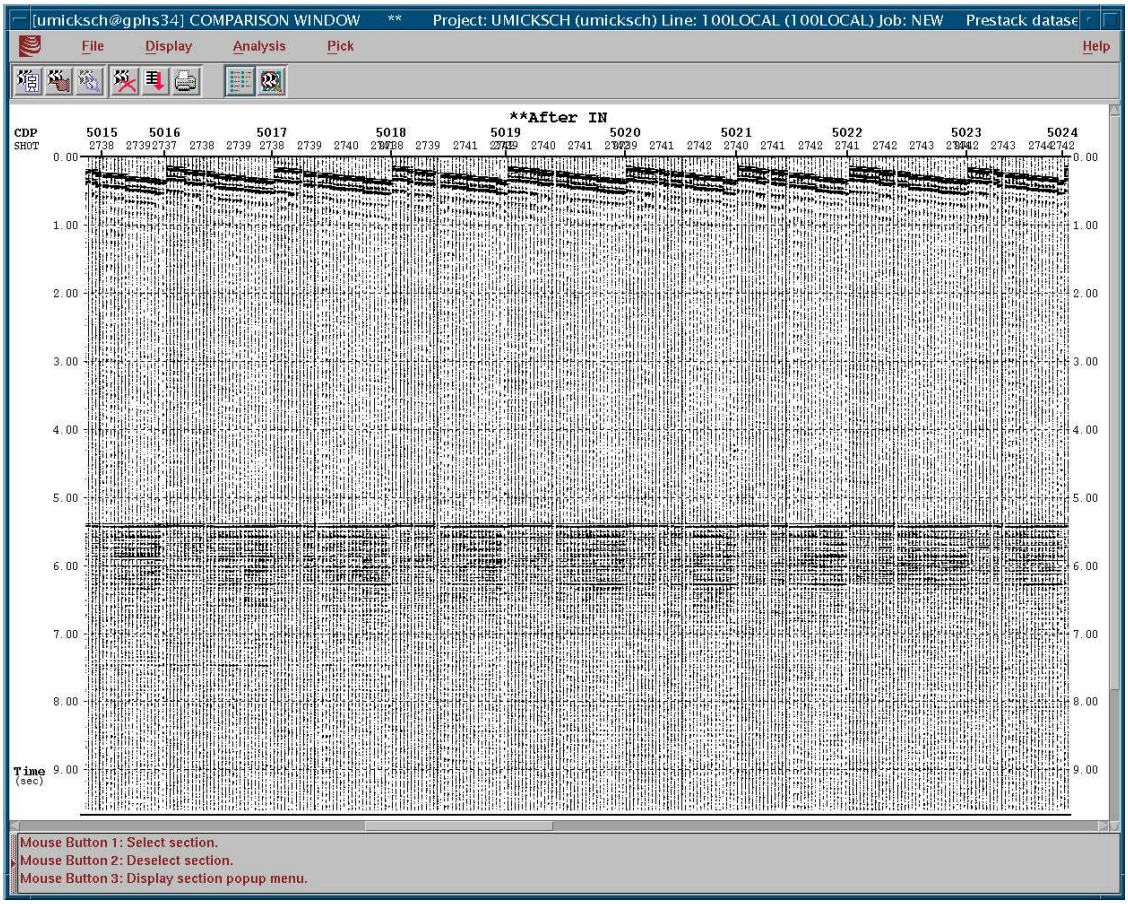

Figure 4.4: Several CDP-gathers of profile 20010100 showing the direct wave and the sea floor reflections.

in the right wind direction for take-off and landing operations, causing the streamer to sink and drift sideways. The correct position and behavior of the streamer are not known in these cases resulting in a geometrical setup not considered during the geometric definition. These parts of the transects can be excluded for further processing and show up as lateral gaps in the data, if the deviation is of a greater amount.

The traces are very noisy, if there was a lot of contact of the streamer with ice floes. Part of this noise can be removed by filtering, but severely disturbed CDPs or traces are removed. A broken hydrophone, resulting in a dead or or bad scaled channel, must be excluded. Reversed traces (meaning a wrongly polarized connection in the cables or switchboxes) must be reversed in polarity. A by-product of the editing process is therefore a kind of 'health status' of the recording equipment and a really bad streamer section could be replaced before the next deployment.

For the used streamer sections, channels 12, 18, 22 and 27 proved bad and were neglected for further processing.

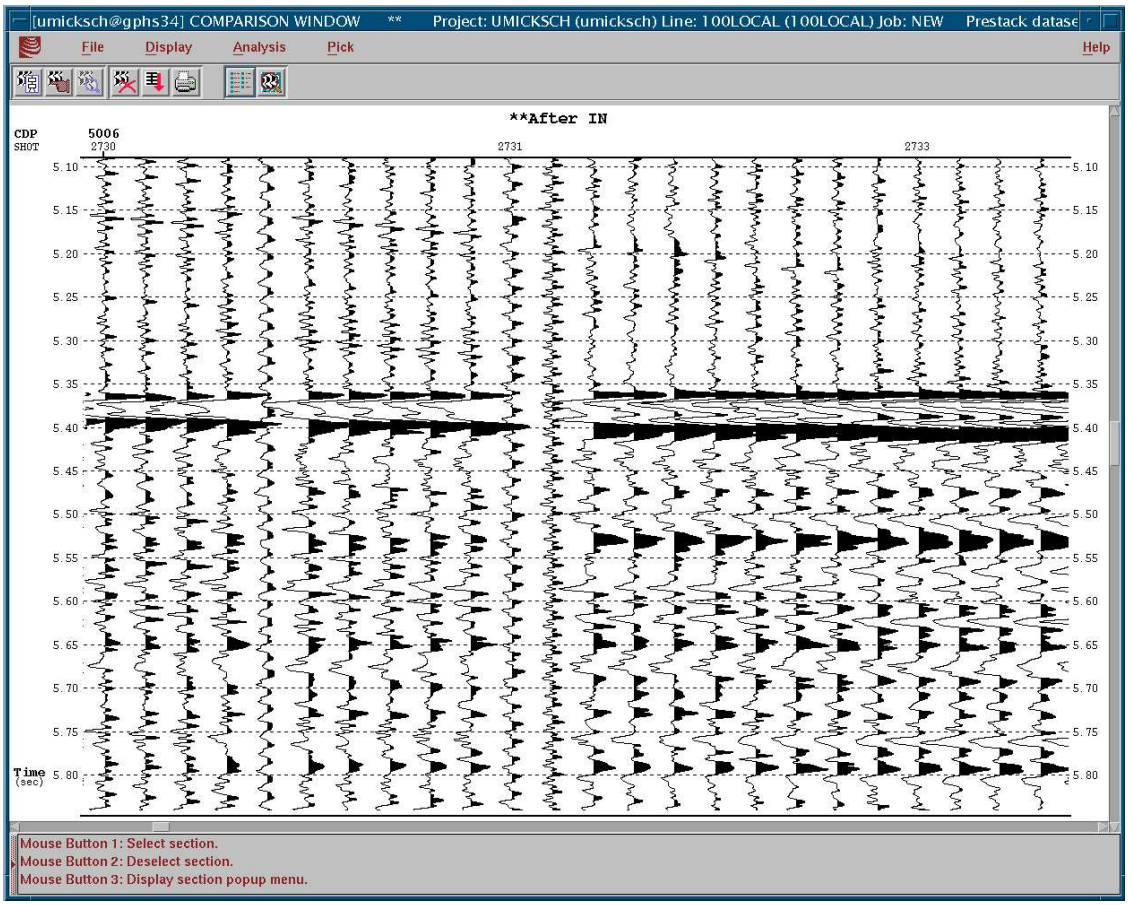

Figure 4.5: Examples of bad traces, visible in the middle of the figure, showing a CDP-gather from profile 20010100

4.2.5 Filtering

Marine data, in comparison with land data, look much quieter at the first glance, due to the undisturbed water column and the often fine-grained, flat-layered sediments. Nevertheless, filtering is necessary. The signals arriving at the streamer are already filtered by the different layers of the Earth and are altered again from the hydrophone specifications, but here, only the user-applied filters, after receiving the data from the streamer, are listed.

An anti-alias filter was applied before digitizing the data, to suppress frequencies above the Nyquist frequency of 180 Hz.

Filtering digital data is quite convenient with FOCUS. One can calculate frequency spectra in-user defined windows in the time section of the data, and in this way one can quickly distinguish between signal and noise frequencies. It is possible to test different filters in adjacent windows on the screen, to find the best border frequencies for a bandpass filter, for example. The filter slopes should be smooth enough to minimize signal distortion due to the Gibb's phenomena. A time variant filter is recommended, because with increasing travel-time natural filtering occurs due to inelastic damping and absorbtion of individual frequencies, reflections and diffractions. Bandpass or notch filters (to rid the data of a single frequency), are the main types of filters used in seismic processing. Some processing sequences alter the data slightly in the frequency, so further filtering can be necessary later on.

The main frequencies of reflection data are between 10 and 70 Hz, with a dominant frequency around 30 Hz (Yilmaz, 2001). The main frequencies of the VLF airguns used during the cruise are between 40 and 50 Hz. Bandpass filters used in the processing had following corner frequencies : 15\20 80\90 Hz. The bubble frequency ranges between 13 - 17 Hz, and so is suppressed by filtering. The 'normal' ambient and artificial noise (Ship, etc.) is reduced by filtering as well.

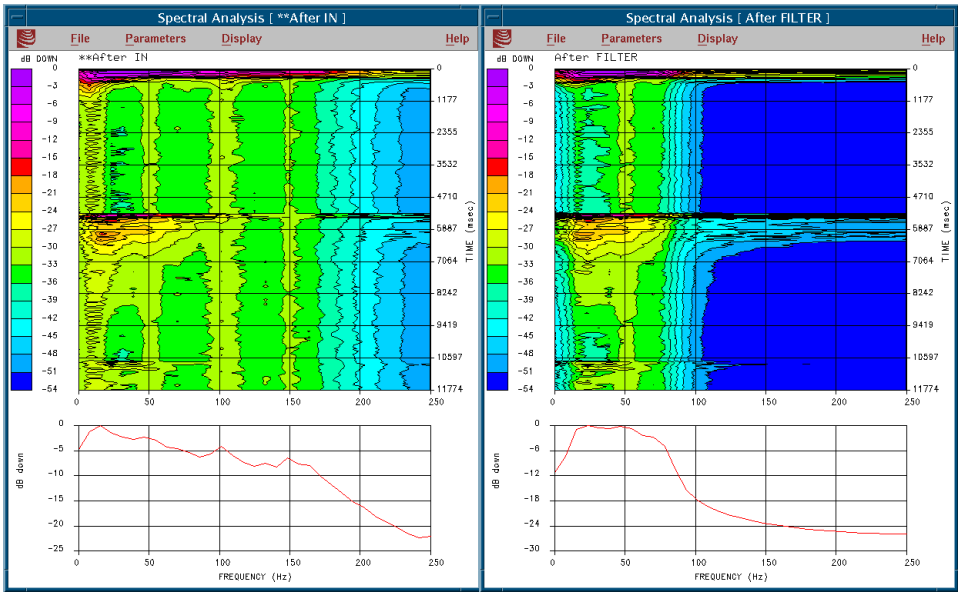

Figure 4.6: Unfiltered frequency spectra (left) and filtered (right), for the whole recording length of 12 seconds. The corresponding data example is shown in the next figure.

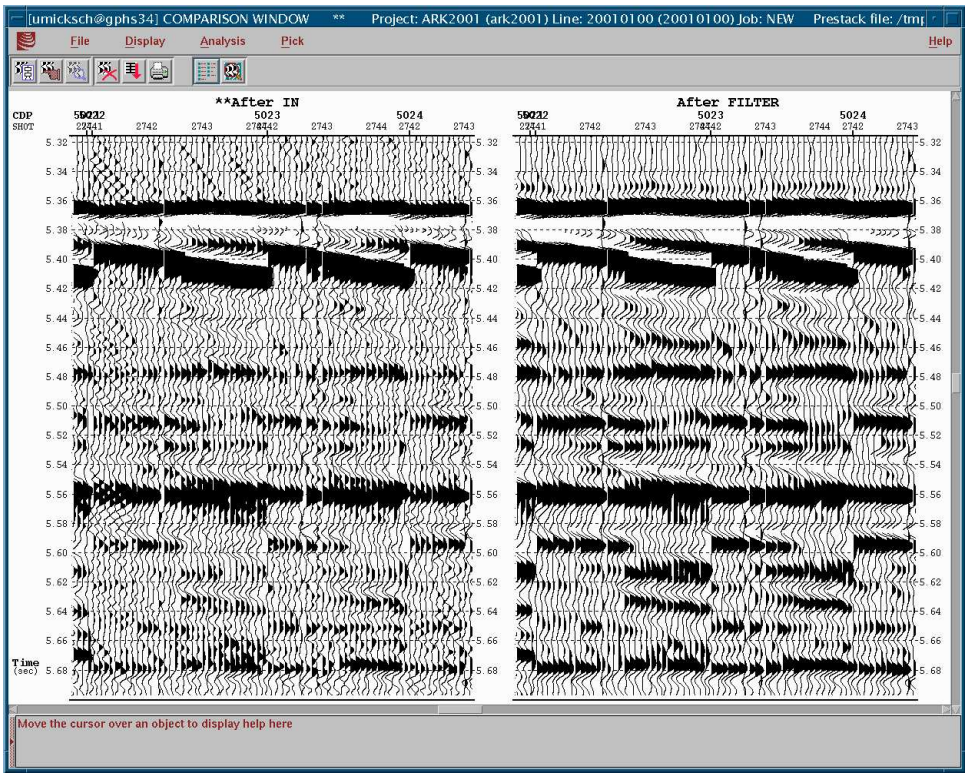

Figure 4.7: Raw (left) and bandpass filtered data (15\20 to 80\90; right), profile 20010100. Here, only the first 300 ms after the seafloor are plotted to show the effects of filtering.

4.2.6 Spherical divergence correction

The shape of the wave released from the airgun is approximated to an expanding spherical wave in theoretical models, neglecting the bulging occurring in the Earth through its inhomogeneous composition. The wave loses energy due to inelastic damping, transmission and spherical divergence as it propagates. This spherical divergence causes a decrease in the energy density, because the energy of the wave must be distributed over an ever-increasing surface with radius r. This happens in a dependence of $\frac{1}{r^2}$. The amplitude of the wave decreases in a ratio of $\frac{1}{r}$.

To cope with the loss, each trace is multiplied with a time variant amplitude scaling function, meaning every sample of the trace is scaled depending of the radius r of the spherical wave at this time.

4.2.7 Velocity analysis and dynamic correction (NMO)

For further processing, like stacking, a velocity model of the investigated area is needed. The velocity model is created with the FOCUS module VELDEF and stored in the seismic database.

In a time vs. offset sketch (see figure 4.8), reflections show up as hyperbolas, with a delay time, Δt, that depends on the offset. In order to stack the correct phases, the traveltime for each receiver, t_R, must be transferred to t_0 (zero offset time). This process is the normal move-out (NMO) correction.

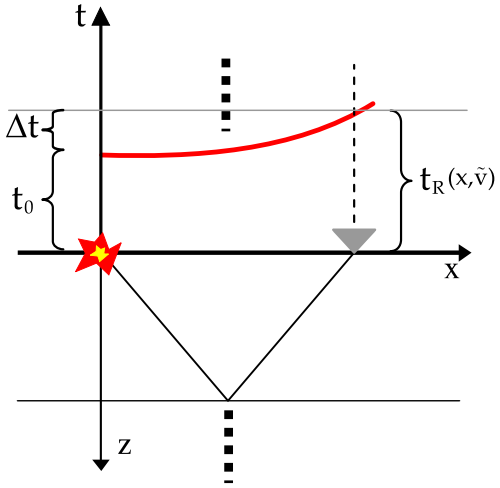

Figure 4.8: Time vs. offset sketch

These hyperbolas can be calculated with

$$t_R^2 = t_0^2 + \frac{x^2}{\tilde{v}^2}, \qquad t_0 = \frac{2z}{v}. \tag{4.1}$$

This equation is a 2 dimensional approximation of that for 3 dimensional wave propagation through an elastic medium, valid for a horizontally layered half space. x is the distance from source to receiver, z the depth of the reflector. $\tilde{v}$ is the rms velocity and a measure for the bending of the hyperbola and is given by (Forkmann, 1987):

$$\tilde{v} = \sqrt{\frac{\sum_k d_k v_k}{\sum_k \frac{d_k}{v_k}}} = \sqrt{\frac{\sum_k {v_k}^2 t_k}{t_0}} \tag{4.2}$$

d_k is the thickness and v_k is the velocity of the k-th layer.

The correction term, $\Delta t_{NMO} = t_R - t_0$, depends on the depth of the reflected layer and the velocity of the layers above ($\tilde{v}$). The deeper the reflectors are situated, the flatter the hyperbola. In deep ocean basins (depth about 4 km) even the seafloor arrivals, that are encountered at about 5 s TWT, give rise to almost 'planar' hyperbolas (see figure 4.9).

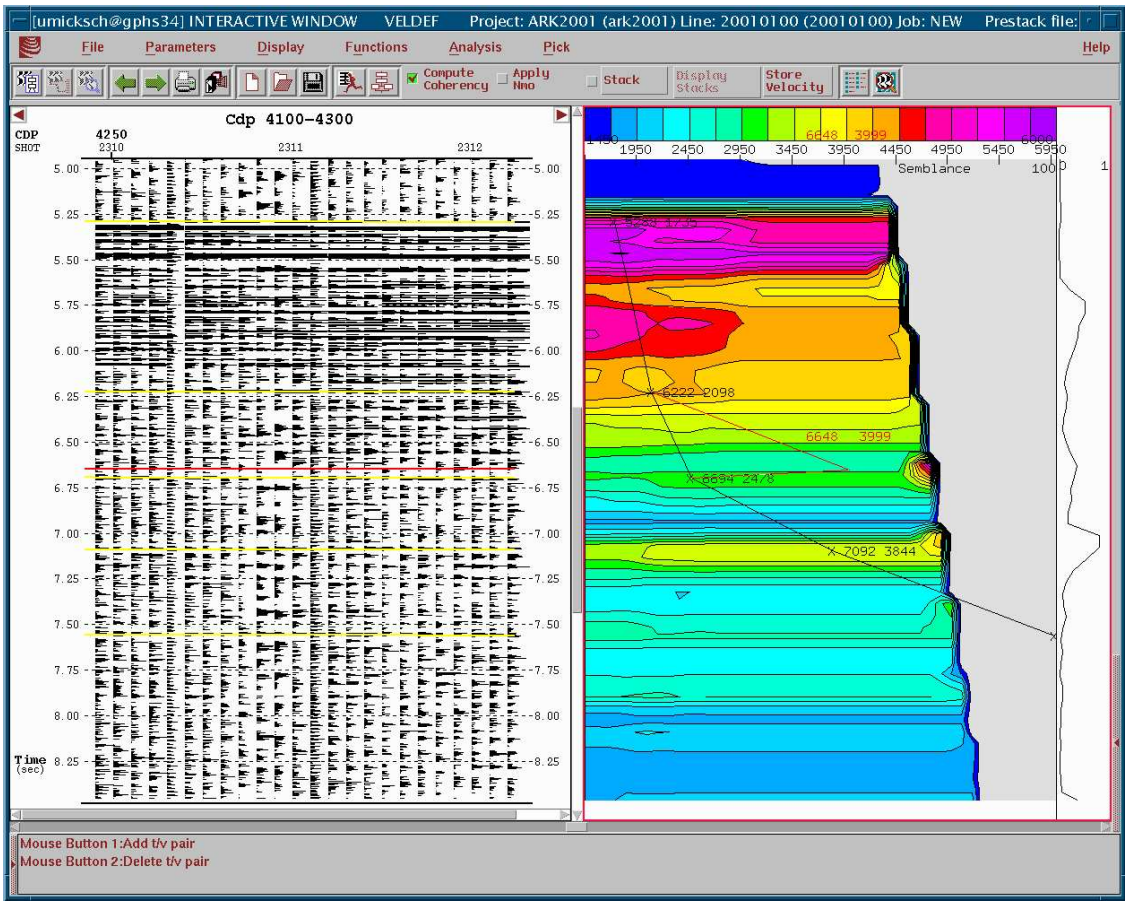

Figure 4.9: VELDEF module in FOCUS

Figure 4.9 shows the interactive VELDEF module in use with a CDP-gather (profile 20010100, CDP 4250) on the left side. The right side shows a time-velocity chart with superimposed semblance. Here, one can pick a theoretical and reasonable time-velocity model, for example

the black curve on the right side. The corresponding calculated traveltime hyperbolas are superimposed on the real data set, on the left (yellow 'lines').

For a better fitting of the curves, the semblance is helpful, which is a measure of coherency. All traces of a CDP-gather are corrected with constant velocities (several NMO corrections) and then compared inside a given time window along the whole trace. The results are coded in colored areas. Zones of high semblance are good candidates for the right time-velocity values, resulting in a good fitted hyperbola. Alternatively, velocity spectra can be used as guidance.

The black curve shown at the right in figure 4.9 is not correct, and serves to demonstrate the problems with deep sea data. The red line in the middle of the black curve is a 'rubber band' line, moving along for further picks, the actual traveltime hyperbola is shown in realtime, colored in red, on the left side. Note, that the red line is parallel to the yellow line underneath. The hyperbolas for a reflector can have a multitude of velocities for calculation, because the bending can not be resolved with the given offsets. The problem could be solved with a longer streamer, unfortunately not practical in regions with heavy ice coverage. With long streamers it may also be possible to include refracted phases in the velocity analysis, depending on the water depth.

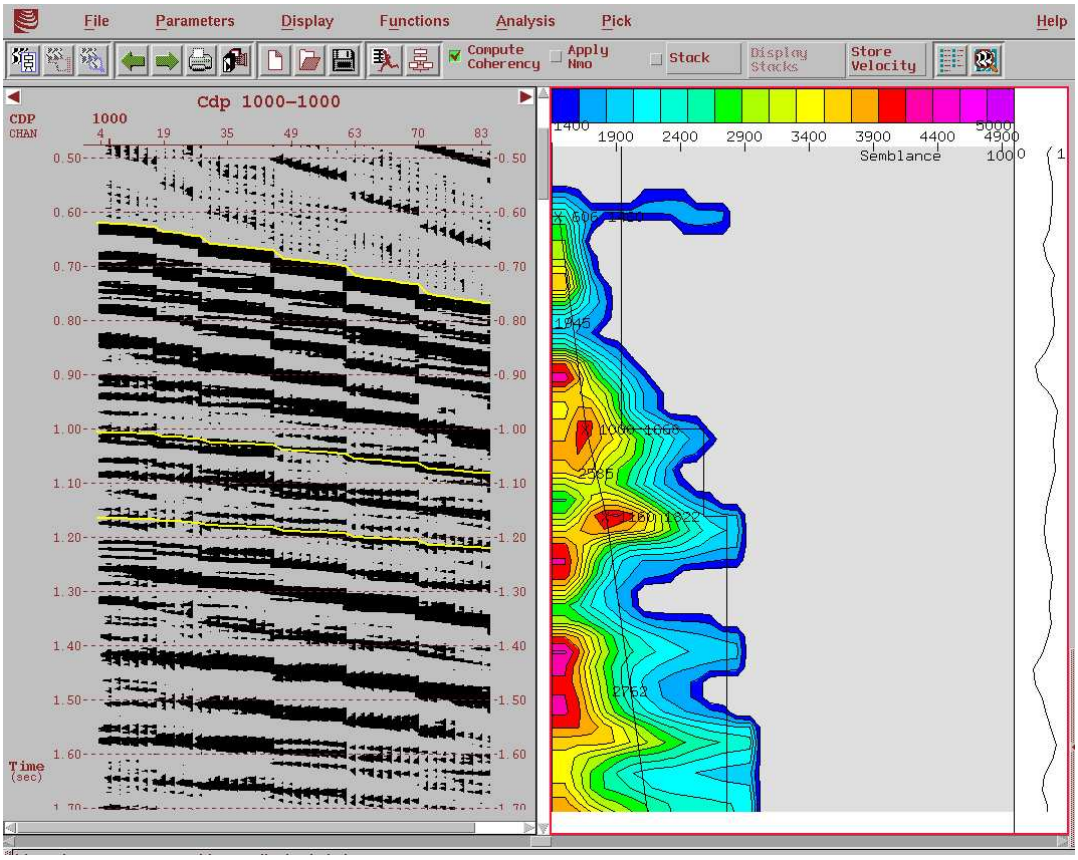

Figure 4.10: VELDEF example of a profile acquired in the Antarctic summer season 2001/2002 (ANT 19/2) (Helm, 2003).

Figure 4.10 shows example data from the R/V POLARSTERN cruise ANT 19/2. The streamer used during this cruise was twice the lengh of the AMORE cruise's streamer. Here, accurate velocity picking is possible. Note however, that the first reflections occur at 0.6 s, while the first multiple shows up at 1.2 s: a problem in shallow waters. Useful data may be under multiples, and can be included in a velocity analysis, but mispicking a multiple reflection will result in a bad stack.

An additional help is test-stacking (stacking see 4.2.8) with different constant velocities for 20 to 50 CDPs. These also have to be controlled visually. If the stacking velocity is correct for a given reflector, it shows up in the test stacks as a horizontal event. If a test stacking velocity is a little too low, the selected reflector bends 'downwards', towards the origin of the time axis, i.e. distant receivers register the data first. This is not possible with reflection seismic methods. The gained velocity information is transferred back to the picking of time-velocity pairs to refine the velocity model. Test-stacking is also useful to obtain a velocity model in areas with a complex geologic structure.

In case of the AMORE data, picking was done with a spacing of 200 CDPs along the profiles, with a simple velocity-depth gradient, considering the the better velocity model extracted from modelling the refraction data.

As already mentioned above, the parameter for the NMO correction is $\Delta t_{NMO} = t_R - t_0$. For a horizontal layered media, it can be written as (Forkmann, 1987)

$$\Delta t_{NMO} = \sqrt{{t_0}^2 + \left(\frac{x}{\tilde{v}}\right)^2} - t_0. \tag{4.3}$$

If this correction is applied to the whole profile, using the velocities picked in the velocity analysis, all 'real' reflectors should show up as horizontal lines in the CDP gathers, but diffracted waves and multiple events are still bent.

4.2.8 Stacking

After the NMO correction, all seismic traces that share a CDP can be summed up, whereby signals in phase are amplified, and incoherent noise is damped statistically, increasing the signal to noise ratio. Diffractions and refractions are also reduced. A n-fold stack results in a $\sqrt{n}$-times improvement of the initial data (Schmöller, 1987). In our case, a CDP fold of 25 results in a 5 times improvement in data quality (see figure 4.11). This method equals a simulated zero-offset experiment for all receivers. Summing up over these traces is also a kind of data reduction without great losses, but with data improvement. For example, the file size after CDP sorting of profile 20010100 amounts to 14 Gb, and the the stacked section occupies only about 530 Mb.

Instead of the normal mean value stack, a median stacking is used, because the noise does not necessarily adopt a Gauss distribution (Geissler, 2001; v5.0 Focus Manual, 2002). The

normal noise spectra is superimposed with several high peaks generated during icebreaking, by reverberations in the icefloes, by potentially damaged instruments or a bad sources (like a defective airgun). The median stack hence provides a better weighting of the signal.

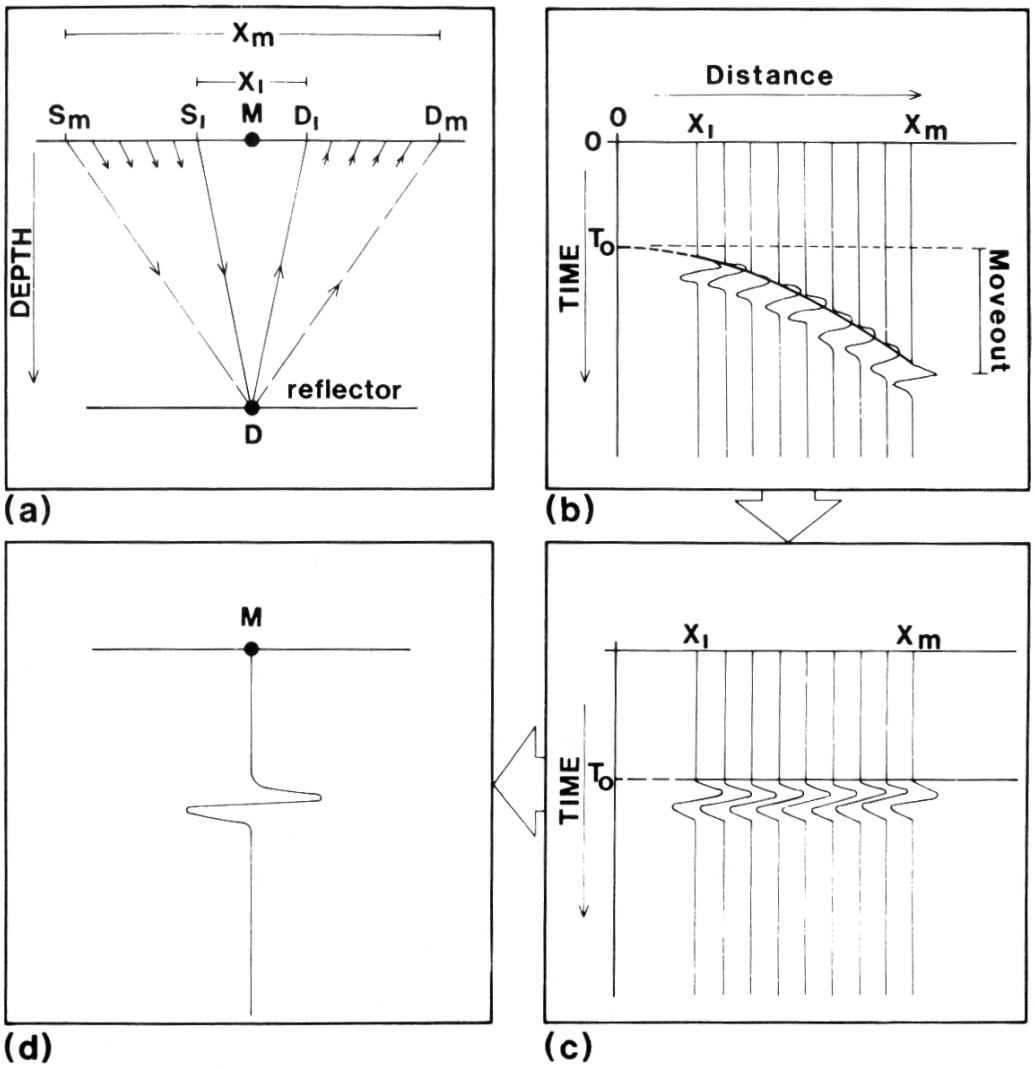

Figure 4.11: The process and result of CDP sorting (a), NMO correction (b,c) and stacking (d) (Beaumont and Foster, 1988)

4.2.9 Muting

Since the water column above the sea floor contains no information useful for a geological interpretation, the amplitudes are reduced to zero for a clearer view of the sub-seafloor data. A mute is created by picking the seafloor topography in FOCUS.

4.2.10 AGC and final stacks

A further way of enhancing seismic data is the use of an automatic gain control (AGC). AGC is a time-variant scaling of the seismic traces that depends on the mean amplitude of all non-zero samples in a given time window, that slides along the trace. The window length itself can be constant or time variant. The amplitude in the center of the window is then multiplied by a scalar, depending on the mean amplitude. The visual result depends strongly on the window length: Long windows retain the character of the input data, whereas too short windows boost weaker signals, but also the noise, levelling the amplitudes. By applying an AGC to all the traces of a shot gather, the signal amplitude for increasing offsets is amplified, making up for the loss of energy of the seismic wave. Applied to the stacked section, AGC increases especially prominent reflectors like the seafloor for example. This is visible as a kind of 'white band'. Later reflections, with amplitudes little over the surrounding noise, are enhanced this way, too. An AGC of 500 ms was used in the processed sections.

Some other common processing sequences, like multiple suppression, for example, were not necessary because of the waterdepth. The first multiple starts to show up after 8.5 seconds TWT at the beginning of the profile 20010100 in the Nansen Basin, useful data is visible only until about 8 s TWT. Deconvolution, or other complex seismic image enhancement processes were not necessary, because the main interpretative goal of the theses - formation of the basins and their structure - does not require precise imaging of sedimentary bodies for their fine texture, concerning reservoir possibilities, for example.

Profile 99176 and 20010100 join each other close after the Svalbard shelf margin. Therefore, it was possible to merge both stacked profile sections. The data files were kept separately and the merging followed in the plotting jobs. This is possible since the two profiles link together perfectly (see figure 4.12). The used source was the same for both profiles, but 1999, is was possible to use a much longer streamer due to light or absent ice (active section 2400 m). Also, the processing sequence varies such as Geissler (2001) used different border frequencies for the bandpass filters or multiple suppression operators were applied on the shelf. This results in a visual effect in the plots, noticeable in different shades of gray.

After these processing sequences the data were plotted as 'stacked sections', a kind of first product. The sections are shown in figure 4.13 to 4.15 and in the appendix. Detailed descriptions of the profiles are given after their depth conversion. 2000 CDPs equal 50 km in all seismic sections to follow.

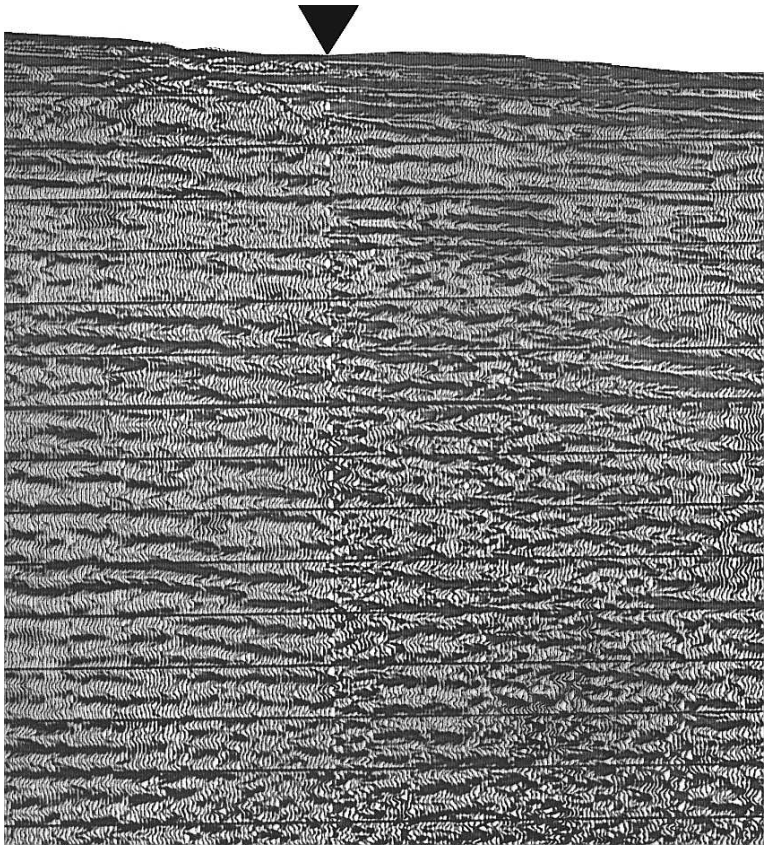

Figure 4.12: The point of rendezvous of both profiles, fitting together perfectly. Profile 99176 is left from the marker, 20010100 is situated on the right side. The shown data section spans over approx 7 km and 1.6 s.

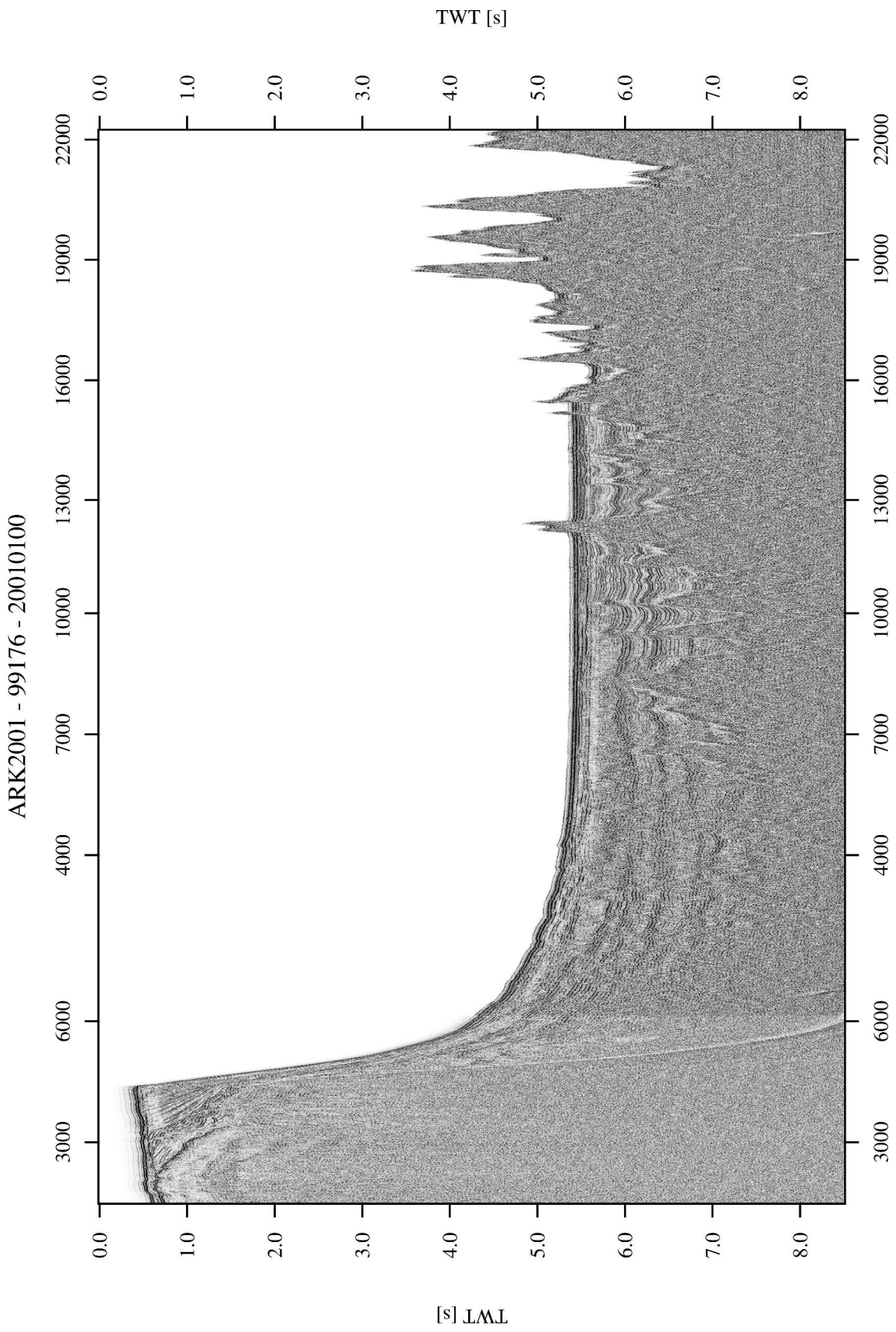

Figure 4.13: Stacked section, 99176 and 20010100

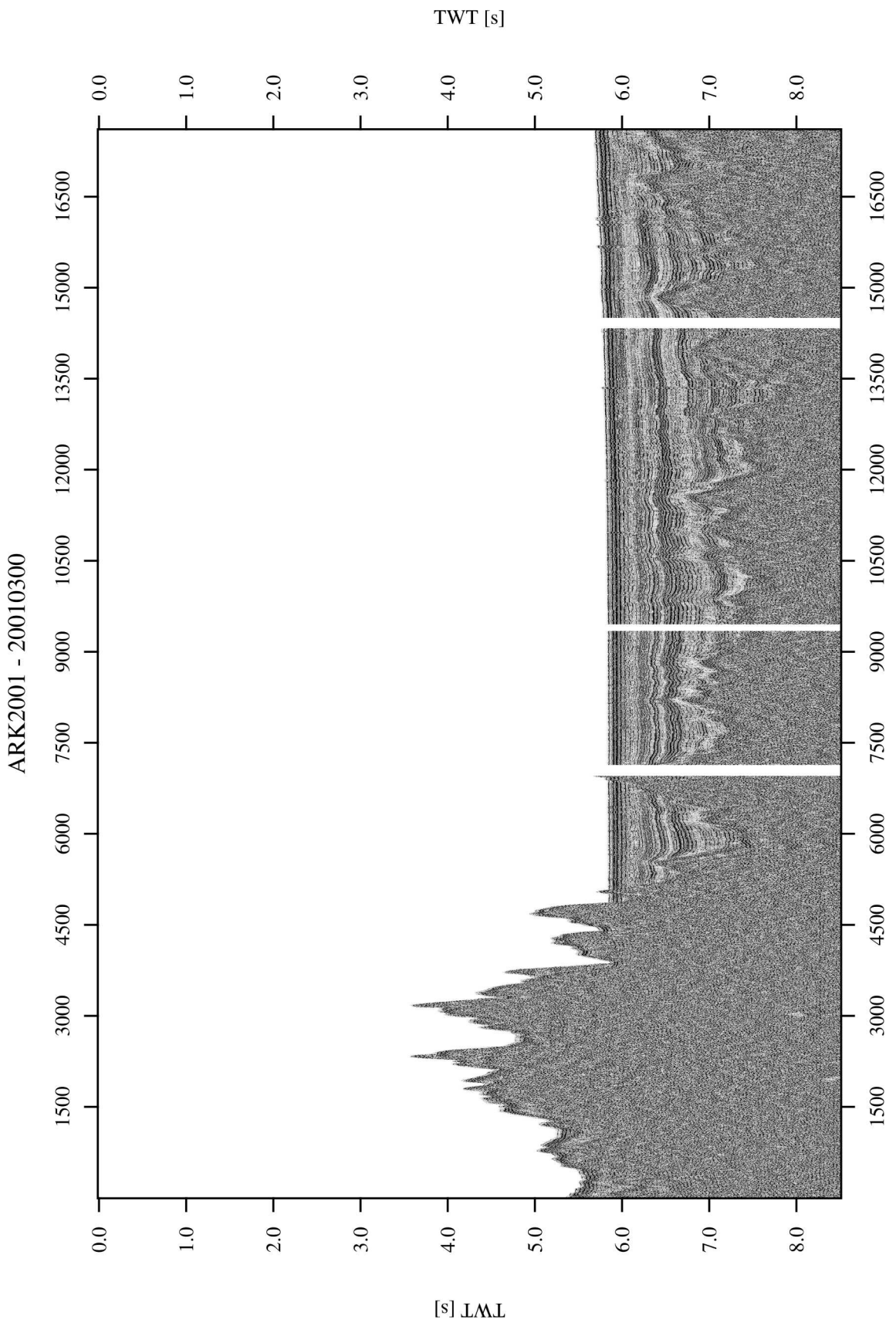

Figure 4.14: Stacked section, 20010300

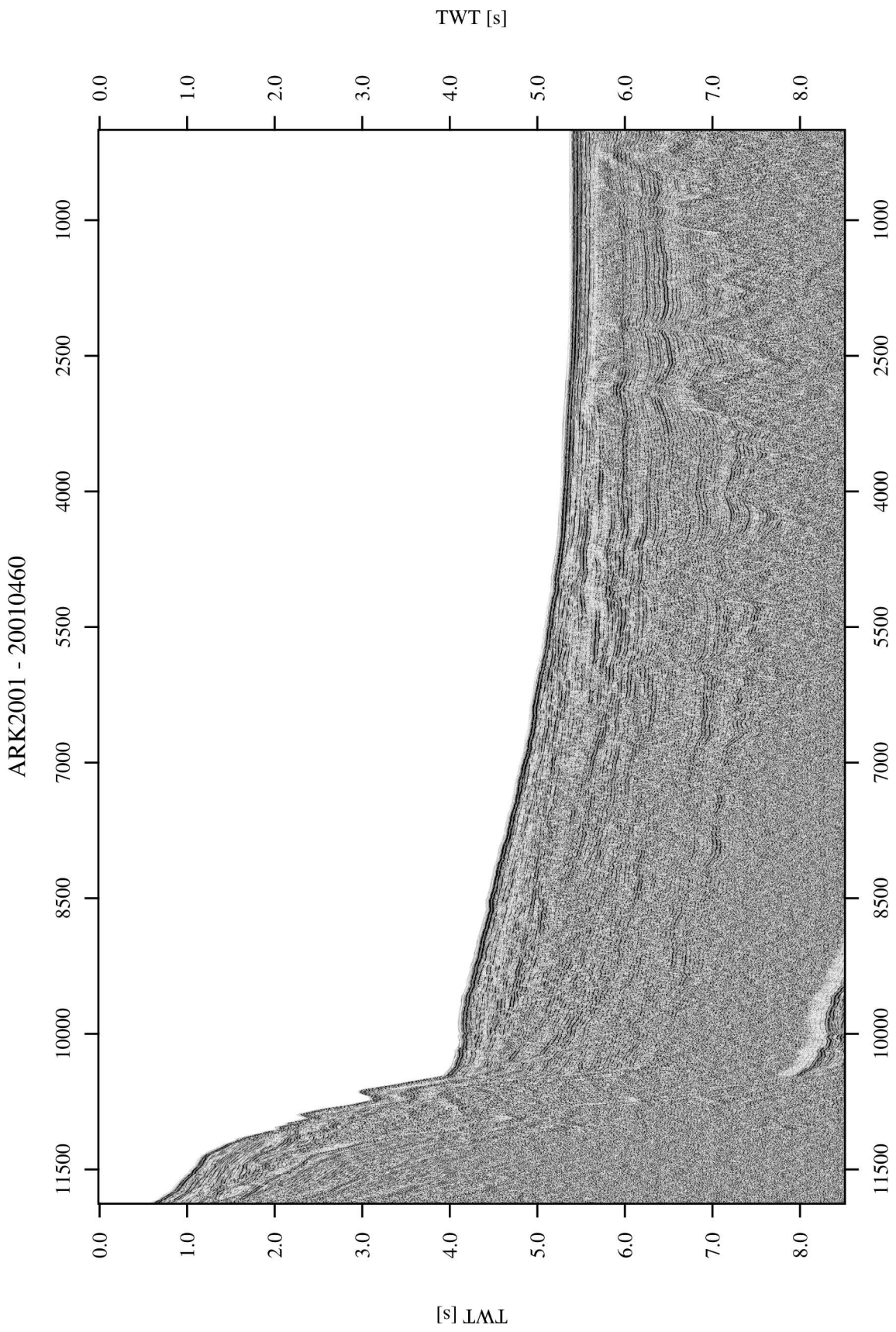

Figure 4.15: Stacked section, 20010460

4.3 Refraction and wide angle seismic

4.3.1 Processing sequence

Raw data

⇓

Demultiplexing

⇓

Geometric definition

⇓

Filtering

⇓

AGC

⇓

Final plots and files for modelling

4.3.2 Demultiplexing and geometric definition

Demultiplexing of the seismic refraction field data follows the same procedure as for the reflection data. The refraction data are recorded along with the reflection data in two additional channels standing for two radio frequencies. Afterwards, the individual sonobuoys have to be 'cut out' of the recordings of channels #49 or channel #50 at the corresponding recording times and saved in separate files. As the sonobuoys record only one channel, the resulting shot-gather consists of one trace per shot, plotted over offset. A typical shot-gather can be seen in figure 4.16. The following figures show the complete data of SB2101, with a magnified insert that shows the first appearance of the refracted waves through the seafloor reflection and the prominent direct wave. Some of the sonobuoys did show a slight 'splitting' of the direct wave, caused by ice coverage. Part of the direct wave travels through ice floes with a higher p wave velocity than seawater and then to the receiver, creating this splitting.

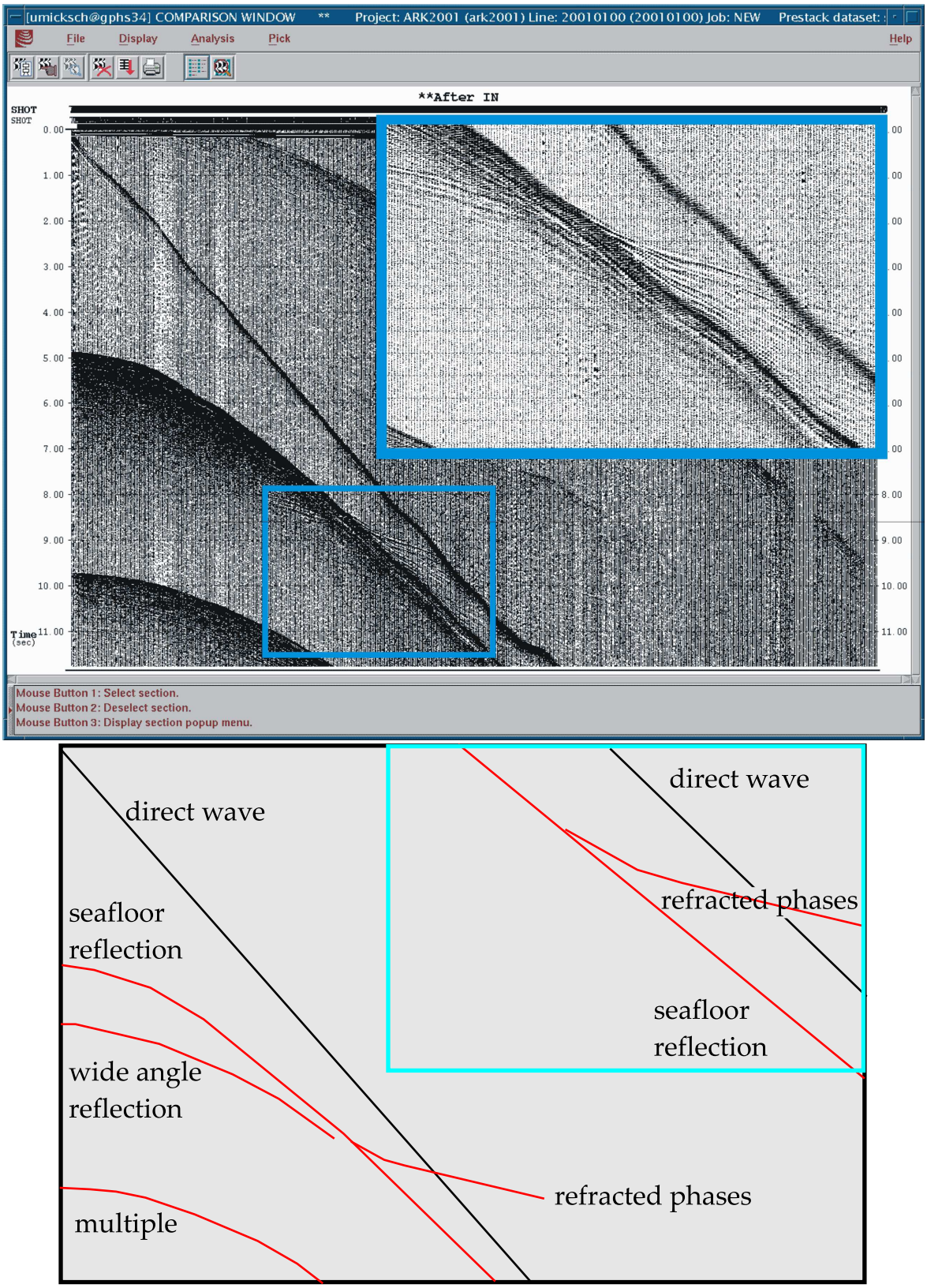

Figure 4.16: Raw sonobuoy data of SB2101 and legend explaining the different types of waves.

4.3.3 Filtering

The bandpass filters applied to refraction data usually have very low border frequencies. This results from the use of big airguns with air chambers of several deciliters that generate a low frequency source. The VLF guns used in the examined profiles generate low frequencies as well, but with much lower energy. The data were bandpass filtered. The filters' corner frequencies ranged around 3\5 20\30 Hz. (see figure 4.17).

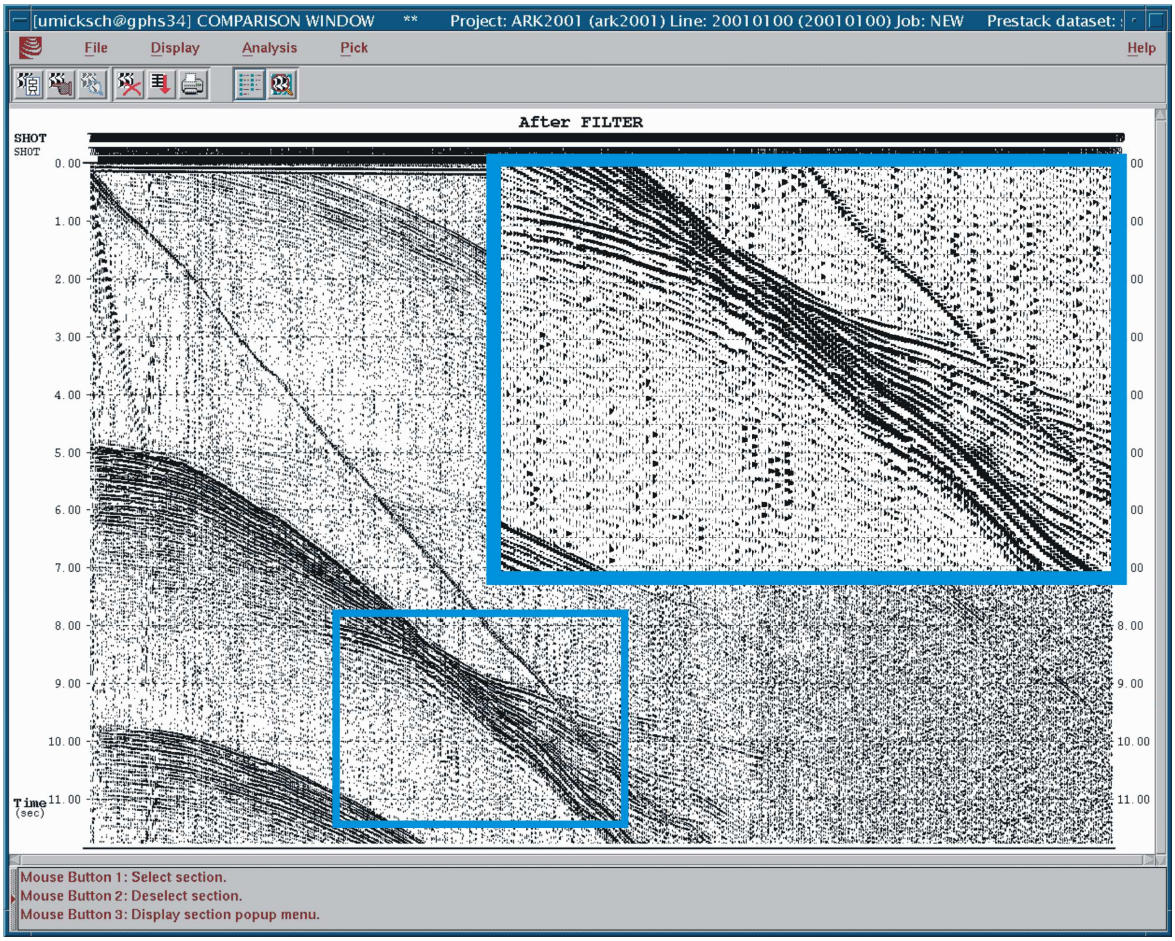

Figure 4.17: Filtered sonobuoy data, SB2101

4.3.4 AGC and final plots

An AGC with 500 ms window length was used for the final processed data files, plots and further modelling (see figure 4.18).

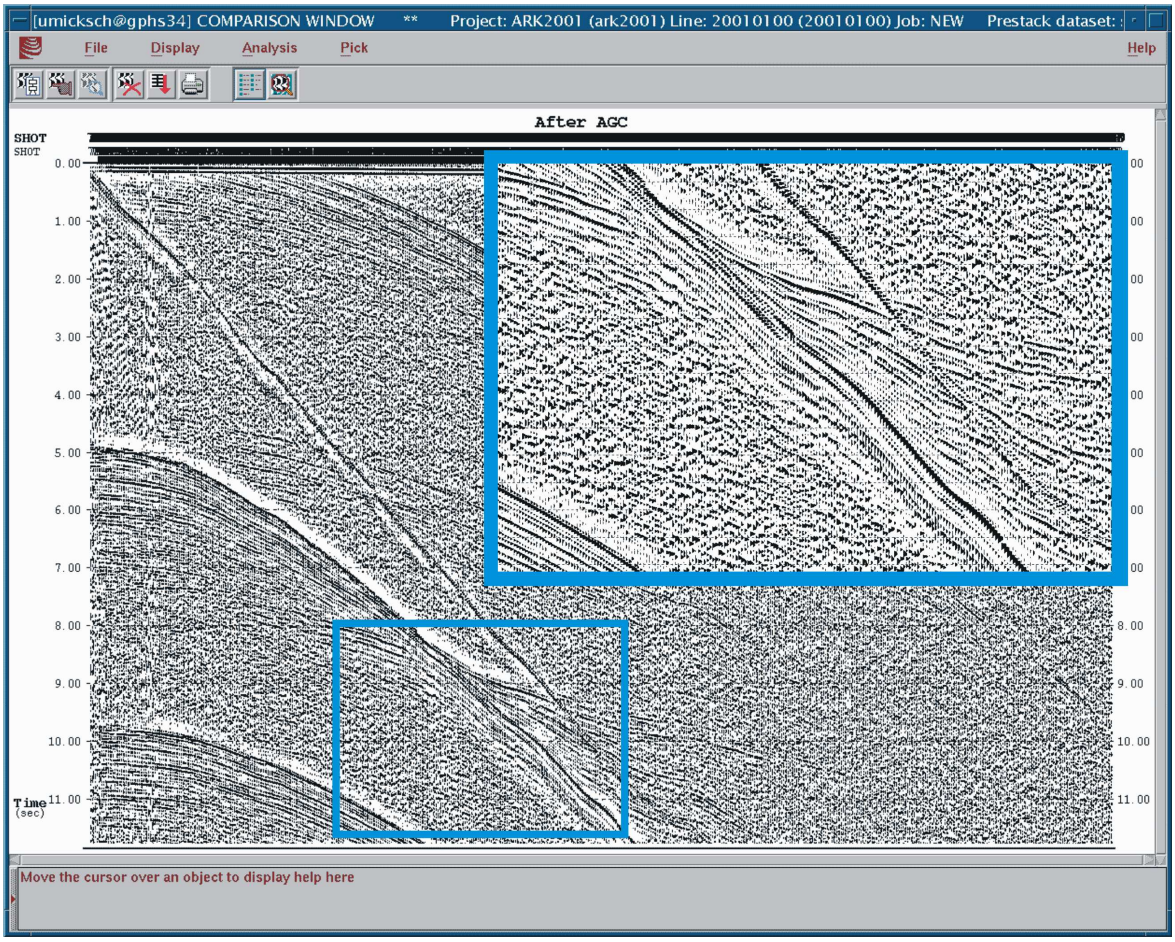

Figure 4.18: Processed sonobuoy data, SB2101 (filtered, AGC)

5 Modelling of the sonobuoy data

5.1 Modelling sequence

Final plots and files after processing

⇓

Manual phase-picking

⇓

Conversion to SEG-Y-format

⇓

Conversion to Z-format

⇓

Phase-picking and assignment with Z-PLOT

⇓

Modelling with RAYINVR

5.2 Preparation for modelling

5.2.1 Manual phase-picking

After plotting, the refracted and reflected phases were colored to distinguish between different phases. Their apparent velocities and intercept times were calculated from the slopes of the refractions and their points of intersection with the time axis (also called zero offset time). The DIX-equation (Dix, 1955; equation 5.1) relates these values to interval velocities of the unique layers. With these interval velocities a draft 1D model was created, that forms basis for further modelling.

The DIX-equation :

$$v_k = \sqrt{\frac{v'^2_k \cdot t_{0,k} - v'^2_{k-1} \cdot t_{0,k-1}}{t_{0,k} - t_{0,k-1}}} \tag{5.1}$$

needs as input the apparent velocities v' and the intercept time t_0 of each layer k.

The data were also plotted with a reduced traveltime. This means the offset is divided by the reduction velocity v_{red}:

$$t_{x_{red}} = t_x - (x/v_{red})$$

The advantage of this technique, is that branches of the traveltime curve with the same velocity like $1/v_{red}$ (or v_{red}, depending on the plotting direction of t) appear horizontal. This provides a clearer image for identifying refracted phases visually, since you have a velocity base to orientate, but must include a reduction term to the calculation of the apparent velocities.

5.2.2 Conversions

The required conversion of the data were carried out with DISCO and segy2z, first into SEG-Y format and then in a format suitable for ZPLOT.

5.2.3 Phase-picking and assignment with Z-PLOT

In figure 5.1, an example of the use of ZPLOT is shown. Different phases are coded by color, like the seafloor reflection in red, for example. On the left side of the seafloor reflection, wide angle reflections are marked (hyperbolic appearance), on the right side, refracted phases are marked (straight lines). The program allows easy navigation and zooming throughout the data and the picks and calculations are of course more accurate than that done on paper. The auto pick function of ZPLOT proved to be not very practicable, because correcting the deviated picks on phase undulations (geometric errors caused by course deviations) took nearly the same time as their picking by hand in ZPLOT. The autopicker also had problems in areas with weak signals or noisy data, where a visual interpretation or interpolation is necessary.

The picks are passed on for use with RAYINVR as time offset-pairs with a user defined error in ms and the 'ray-code' extracted from the color of the picks.

5.3 Modelling with RAYINVR

In the following subsections the fundamentals of ray tracing as well as the modelling itself, with its advantages and limitations are explained. Afterwards, the results are presented and the output for further interpretation is introduced. For further information about ray-tracing, consult Červený et al. (1977), McMechan and Mooney (1980) and Zelt and Smith (1992).

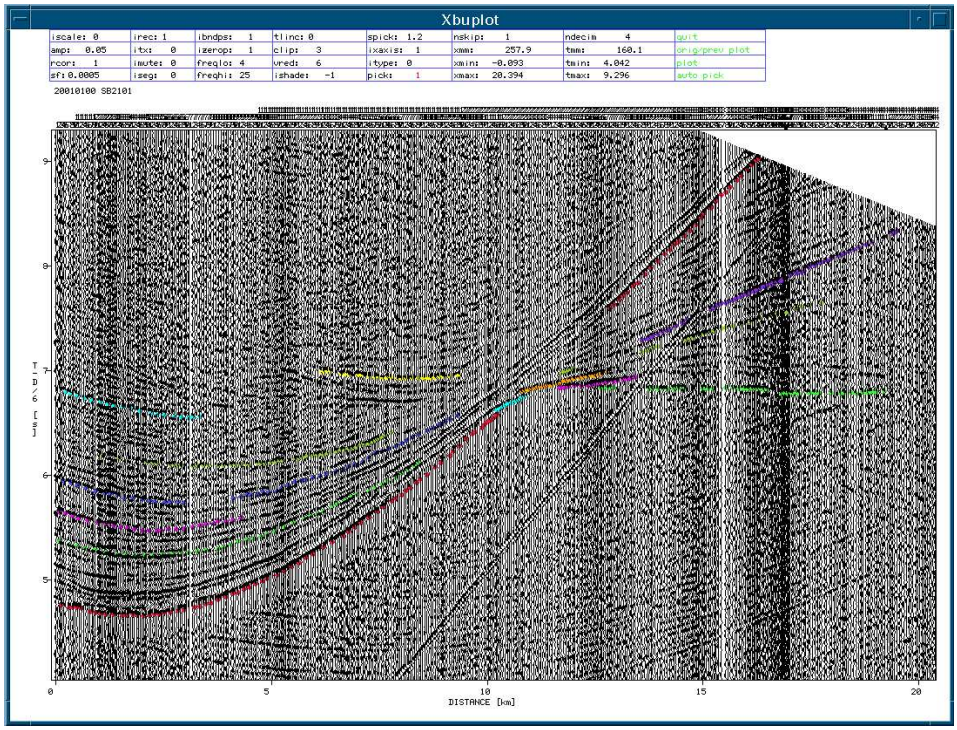

Figure 5.1: ZPLOT, screenshot example (SB2101). The the used reduction velocity is 6 km/s

5.3.1 Fundamentals of ray tracing

The ray tracing method uses an efficient numerical solution to the 2D ray-tracing equations coupled with an automatic determination of ray take-off angles (Zelt and Smith, 1992). These ray tracing algorithms were developed by Červený et al. (1977). The program from Zelt and Smith (1992) uses smooth boundary layers to overcome problems of instability caused by model parameterizations, resulting in 'shadow zones' (Zelt and Ellis, 1988).

A seismic wave is modelled by a set of rays, where each ray represents the wavefront propagation from the source to the receiver. Each time the ray crosses a geological interface (changes in density), the ray is reflected or transmitted (bended, refracted, ...), and therefore the angles of incidence change and must be recalculated. Although seismic waves can be converted from pressure to shear waves and back again, only p waves were regarded in this thesis. It was assured, that no s wave (converted to p waves again) was mistaken as a pressure wave during modelling, by testing with the $\sqrt{3}$ ratio of the velocities, for example.

The 2D ray tracing equations are a pair of first order ordinary differential equations and can be written in two forms (Červený et al., 1977, equations 3.19 and 3.19'):

$$\frac{dz}{dx} = cotan\Theta \ , \qquad \frac{d\Theta}{dx} = \frac{(v_z - v_x cotan\Theta)}{v}, \quad and \tag{5.2}$$

$$\frac{dx}{dz} = tan\Theta \ , \qquad \frac{d\Theta}{dz} = \frac{(v_z \ tan\Theta - v_x)}{v}. \tag{5.3}$$

The initial conditions at the source of the ray are given through $x = x_0, z = z_0, \Theta = \Theta_0$. The choice of equation pair is made by the alignment of the rays. Equation 5.2 is used for near-horizontal ray paths, with x as the integration variable, whereas equation 5.3 is used for near-vertical ray paths, with z as the integration variable. Θ is the angle between the tangent to the ray and the positive depth axis, z. v is the wave velocity, with its 2D components v_x and v_z (see figure 5.2).

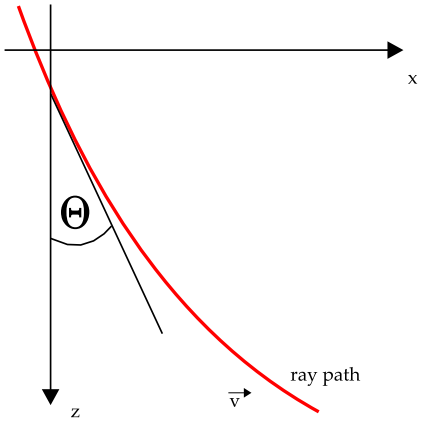

Figure 5.2: Ray tracing parameters

Furthermore, the ray step length and the ray take-off angle must be calculated with methods described in detail by Zelt and Ellis (1988). The ray step length depends on the local velocity field of the model and so is sensitive to the amount of bending, for example. This dependence is needed to avoid small step lengths when the bending is small (needlessly increases CPU time) and errors in ray tracing through large step lengths when bending is large. To speed up calculations, the take off angles are calculated only for ray groups. A ray group is defined as a set of rays, that all have the same turning or reflection point. For a refracted ray group, after determining the angles for the shallowest and the deepest ray, the take off angles for all other rays must lie in between. This narrows the search range of angles for each calculation. Determination of the marginal angles is done by a search algorithm from Zelt and Ellis (1988).

Figure 5.3 shows the used ray types, propagating in a simple subsurface model. The first layer has a constant velocity body (simulating the water column), the other layers have gradients, expect the uppermost figure. Here the second layer also has a constant velocity body, too.

Figure 5.3a and 5.3b show reflected waves, reflected at the same horizons, but with different velocity distributions in the layers. For a constant velocity layer (5.3a), the rays have linear paths, and are recordable over very large offsets, even outside the shown area. Note, that there are no reflections at model edges. With a velocity gradient in the rock layer (5.3b), the reflected waves bend, and the maximum offset shortens. Back in the water column, rays are

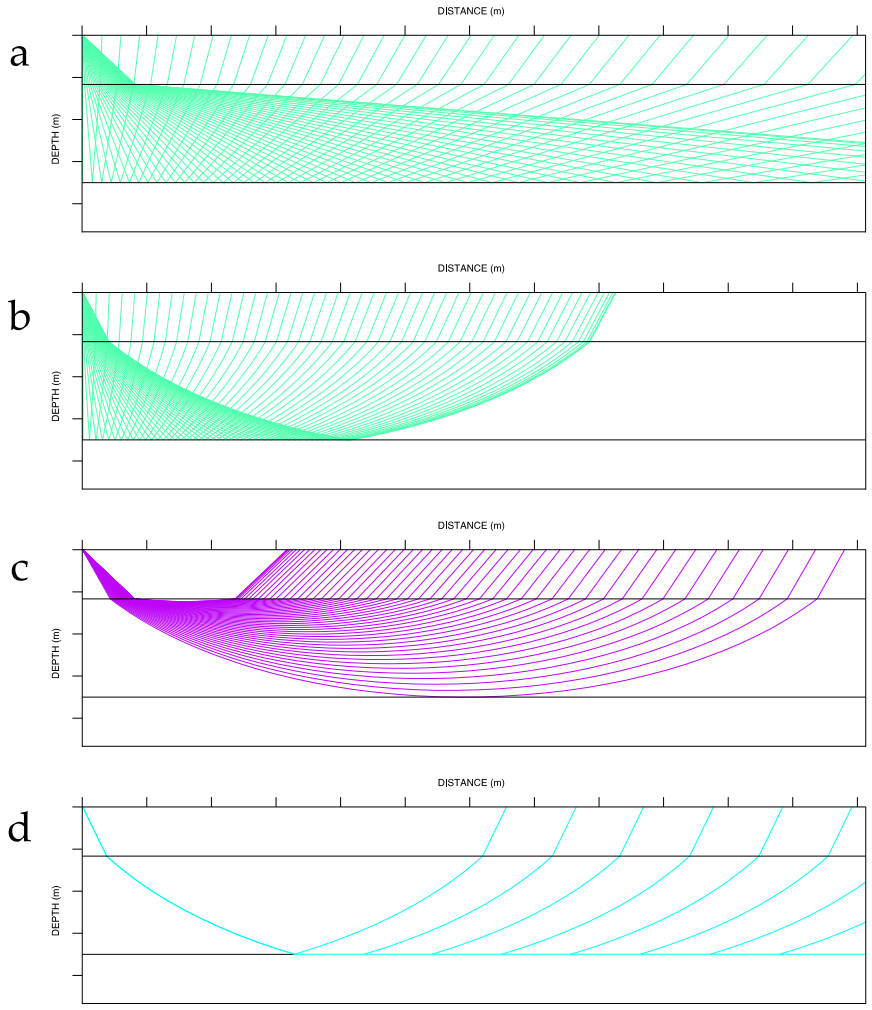

Figure 5.3: Ray tracing of different phases through a simple velocity model (reflected (a,b) refracted (c) and head waves (d)).

straight again. Figure 5.3c shows the ray group of a refracted wave travelling through layer two. In order to create refracted waves, a velocity gradient is necessary. Figure 5.3d shows a Mintrop wave or head wave. These waves travel in the boundary between the two layers involved, at the higher velocity of the lower layer, and continuously emit waves back to the surface. It is possible to model multiple reflections for any horizons or converted waves, zero offset reflections or floating reflections emerging at boundaries not associated with velocity discontinuities.

5.3.2 Model parametrization

The ground models RAYINVR processes can be very arbitrary and complex, and basically consist of layers and blocks defined by nodes, that are connected by linear interpolation. The position and number of these nodes can be different for each horizon, to include areas of higher resolution (more receivers) or to follow horizon topography like the sea floor for example. Horizons are not allowed to cross each other, but free ending and beginning of horizons is possible. The velocity field of a layer is given through top and bottom velocities beneath the upper layer boundary. Velocities can be equally arbitrarily placed within the model, although they must not be on the same positions as horizon nodes, and top and bottom velocities must not be equal. So, the input data for the model consists of blocks representing the unique layers, and are parameterized by horizon data and two velocity values (see figure 5.4). Each data point (node) needs the x position along the profile, the depth or velocity and an inversions parameter (0 or 1).

```
1    0.00  28.00    % length of layer is 28 km.
0    0.00   0.00    % depth of the layer = 0 (ocean surface)
        0      0
1    0.00  28.00
0    1.54   1.54    % upper water velocity
        0      0
1    0.00  28.00
0    1.54   1.54    % lower water velocity
        0      0
2    0.00  10.00  12.00  15.00  28.00    % additional x positions
0    3.85   3.86   3.90   4.00   4.05    % seafloor topography
        0      0      0      0      0
2    0.00  28.00
0    1.90   1.90    % upper velocity of the first sediment layer
        0      0
2    0.00  28.00
0    2.00   2.00    % small gradient in the sediments
        0      0
3    0.00  15.00  28.00
0    4.80   4.70   4.60    % first horizon, slightly dipping
        0      0      0
      ...
```

Figure 5.4: Velocity model input for RAYINVR

For ray tracing, the layers are divided into trapezoidal sections at given nodes with vertical boundaries. The velocity field inside these trapezoids is defined by the velocities at their corners and is determined by linear interpolation. Shattering and focusing of rays might occur

at boundaries due to the blocky parametrization of the model. This can result in shadow zones at the surface and in low a number of rays reaching the receivers. To overcome these obstacles, Zelt and Ellis (1988) implemented a smooth boundary simulation in the program, which samples the boundary transition at a few hundred points and applies a filter to smooth the transitions.

5.3.3 Ray-tracing practice

In addition to the velocity model and the file including the picks from ZPLOT, an 'operating' file is needed to run RAYINVR. All necessary parameters for ray tracing, the type of rays to be calculated as well as the parameters for visualization are declared in this file. Modelling is then the time-consuming process of fitting the calculated response of the underground model to the recorded data within a fault tolerance, defined by the accuracy of the pics. This process is a total visual one (see figure 5.5) and achieved by varying the velocities, horizon depths and topography and repetitive ray tracing. For ease of use different ray groups (reflected wave at the first layer and/or the refracted wave in layer four ...) can be displayed separately.

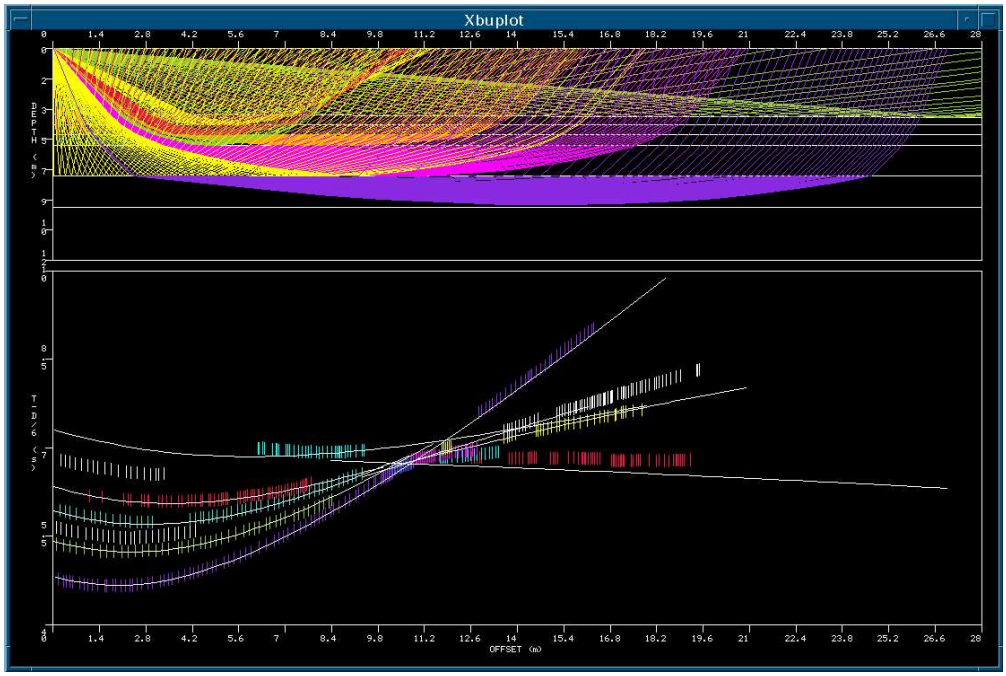

Figure 5.5: Example of the visual output of RAYINVR. All traced rays from all assigned wave types shown. The last layer (red picks on the right) still needs some tending.

Modelling the travel time curves is a non-unique process. Some combinations of layer depth and velocities can lead to the same result of a good fitted traveltime curve. It is possible to generate good fits just by varying the velocities and keeping the depth constant, and vice versa. In such cases was is helpful to look at the created 1D model or choosing plausible

velocities: The first layer of marine sediments normally won't have velocities of 4 km/s, for example.

The procedure is followed top to bottom, starting with the surface/seafloor layer. The seafloor topography is simply obtained the ship's sounding and positioning system, or, like on Polarstern provided by the bathymetric working group. For the deeper horizons the corresponding sections of the reflection data were considered to get a idea of horizon arrangement and variation. Note, for ray tracing the source-receiver layout is reversed. The source is seen as the receiver and the starting point of the rays is the hydrophone of the sonobuoy. This is not necessary for ray tracing, but merely an adaption from land refraction seismic methods, which normally have a one shot, multiple receivers setup.

5.3.4 Limits and errors

As already mentioned, one problem is the non-uniqueness of the modelling, which can be compensated by skillful modelling. The main errors occur through the experimental setup or the user's interpretation of the data during phase-picking.

The biggest error results from drifting of the used sonobuoys, whose position is only known at the position of deployment. Due to wind, sea currents and ice movements the sonobuoy drifts from that position. Inside a certain radius of the deployment position, the drift is irrelevant, because of the long wavelengths used in in refraction seismic. In addition, with longer travel paths in depth direction (z) small variations in the x/y position of the receiver are not relevant. The drift paths are also reduced, since the buoy is only active for 2 to 3 hours at most. During the refraction seismic experiment directly on Gakkel Ridge (Jokat et al., 2003), Ref - Tek stations were deployed on ice floes for two or more days. They did record a variety of drift paths, but no obvious order or pattern was found in these, which could be applied to the sonobuoys to correct their position.

Drifts show up noticeably as lateral gradients in the water column or anomalous water velocities in comparison with that available from the bathymetric group on board. The wrong water velocities result from a violation of the assumed fix experiment geometry. The only correction of the sonobuoy position is possible in the 'in line' direction (ship track direction), calculated with the deviations of the water velocities. Variations to the 'left' and 'right' can't be resolved. In the data set from profile 20010100 for example, a huge lateral velocity gradient (huge drift) could be found only for one sonobuoy. The applied drift correction did not really improve the quality of the model and was therefore omitted as well as for the other stations with minor deviations in water velocity. One Ref-Tek station was used for modelling in the Amundsen Basin and the coordinates of the station are known since these devices are equipped with a GPS sensor. Here, a drift correction was applied.

For the future, a retrievable buoy is in development, equipped with a GPS sensor and a satellite

phone to transmit its position. This means that larger offsets, meaning longer recording times, are possible as well as a drift correction (H. Martens, personal communication).

Another problem is the lack of a reverse shot through the model, because no second buoy was deployed some kilometers before the ship. This could be possible with the use of the onboard helicopters, but the ship's speed could decrease or it could get stuck due to the ice conditions, meaning the data would be not useful due to the buoy's limited recording time. Because of this, it is not possible to determine if changes in the slope of the refractions are due to new layers, or just to dipping layers. Apart from the basement, the sedimentary layers in the reflection seismic data show no large inclinations in the areas covered with sonobuoys. Therefore, the lack of a reverse shot is no serious problem.

The final error in the horizon depth and in the modelled velocities derives from the set error to describe the accuracy of the picked phases. This error was estimated to be between 50 to 100 ms and incorporates the read off error and effects due to shape variations of the signal caused by noise and filtering. For almost all sonobuoys a error of 50 ms could be kept for modelling. At a few buoys, a error of 75 or 100 ms was assigned to unique phases, in order to model these (ie. SB2109). This was necessary because of diminished data quality and the influence of the basement highs in close vicinity, biasing the ray-tracing models. The model boundaries were fitted to the top and bottom of the error bars (50 ms) by varying the horizon depth, whilst keeping the velocity constant, and vice versa, to asses the error of the underground model. The depth of the modelled layers may vary within 200 m for a depth of 7 km. For a depth of 4.5 km the variation is little below 100 m, which is fine considered the best vertical resolution of approx. 25 - 60 m. The velocities may vary within 0.1 to 0.2 km/s.

Figure 5.6 shows the picked travel-times (black bars) together with the calculated travel-times curves (red lines) from modelling SB2101 and SB2103, which fit reasonable well. The length of the error bars are 50 ms. The seafloor reflection is slightly outside the given, minimum error bars at some offsets, perhaps due to small drifts of the buoys, since a fixed water velocity was assumed.

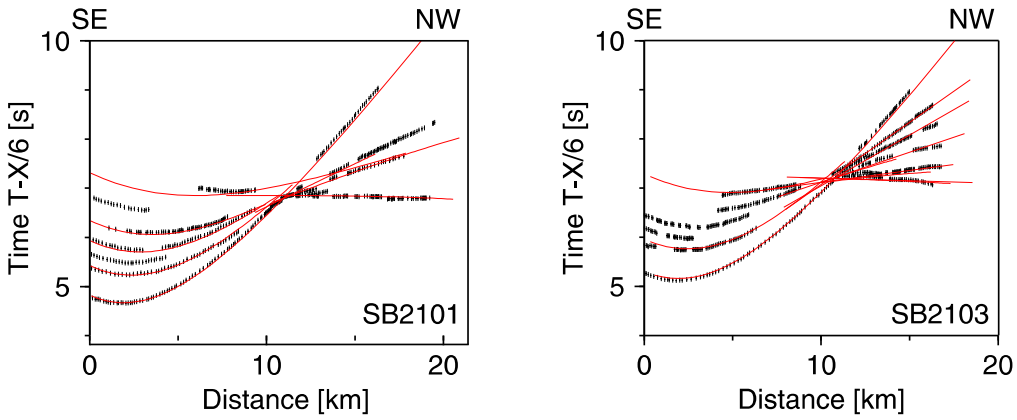

Figure 5.6: Travel-time/offset chart for SB2101 and SB2103.

5.3.5 Results of the ray-tracing

Altogether, 29 sonobuoys were deployed along the ship-track. In the Nansen Basin, 12 sonobuoys were dropped (10 on profile 20010100, 2 on profile 460). 17 sonobuoys were deployed along the transect in the Amundsen Basin. Not all SBs could be used for interpretation due to the recorded data quality or malfunction. On profile 20010100, SB2102 was excluded, in the Amundsen Basin, three buoys (SB2116, SB2120, SB2125) could not be used. In addition, 2 Ref-Tek stations were set up on ice floes in the AB, whereof ST302 was used for interpretation.

The modelled boundaries were exported from RAYINVR at the sonobuoy positions as time-velocity pairs. These results were marked in the plots of the reflection data, to check if modelled interfaces coincide with real reflectors, before declaring a model as final.

Figure 5.7 shows a visualisation of the the p wave velocity distribution at the sonobuoy positions of all three examined profiles. Corresponding layers of each sonobuoy could be modelled with similar velocities. Their generalized velocities are shown in the legend, right-handed to the belonging profile. The upper section of each column with the buoy label is part of the water column. 4 major sedimentary layers could be identified for all profiles. The velocities range from 1.8 to 3.8 km/s. Basement (crustal) velocities are interpret to occur above 4 km/s and are marked with a dashed signature. Note that the thickness of the basement layer does not imply the total crustal thickness. The basement could not be resolved at every buoy due to the recorded data quality.

The detailed alignment of the horizons and the real distances between the sonobuoys can be viewed in the line drawings later on for a clearer understanding of the shown data. SB2105 of Profile 20010100, for example, is situated directly over a prominent basement high, which biases the deeper model layers. The layers and velocities which fit not to the segmentation of the other buoys and were marked extra. The velocity distribution of 20010100 and 20010460 is similar. In the Amundsen Basin, three sonobuoys close to the axial valley of GR (SB2113-Sb2115) are shown with an extra velocity code. SB2128 and SB2129 are believed to be situated already over transitional or continental crust close to the Lomonosov Ridge. Layer 4 (2.8 - 3.0) shows seismic velocities not typical for oceanic crust of ages older than 55 Myrs. In addition a increase in crustal velocity was asserted in direction towards the Lomonosov Ridge.

The sonobuoy interpretation already mirrors the structure of each basin as well as their differences, even with this little number of sampling points provided. The subsidence of the basement is clearly visible in profile 20010100, as well as the rough basement relief can be guessed from the variations of the top of the basement. Profile 20010300 (AB) shows much lesser sediment than the Nansen Basin in comparison.

The shown (figure 5.7) velocity distribution was used as input for the depth conversion of the stacked time sections, which is described in the next chapter.

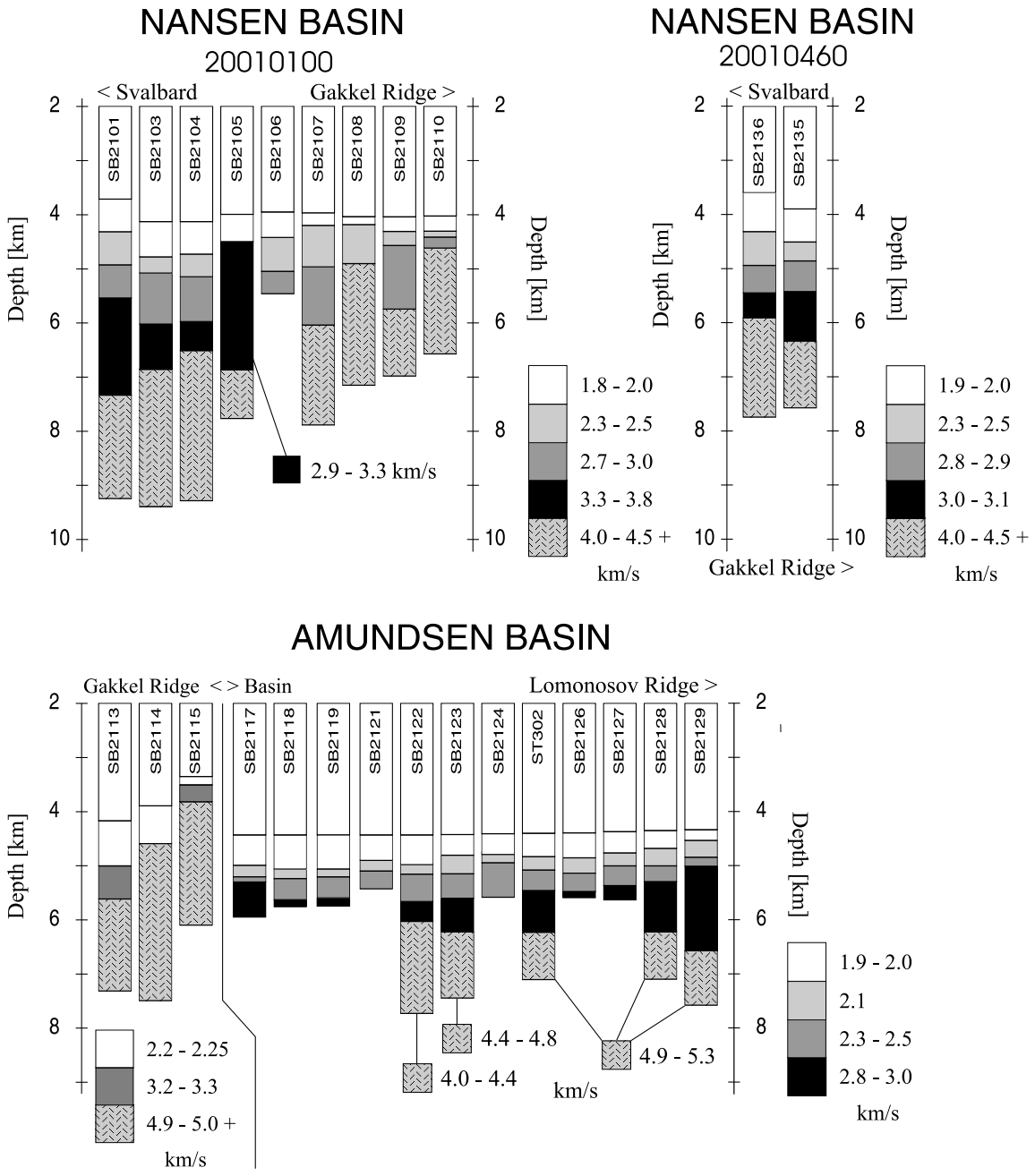

Figure 5.7: Velocity-depth distribution of the refraction data set from AMORE

6 Merging of reflection and refraction data: Depth conversion

A velocity model for the reflection data is created from the results of sonobuoy modelling, and afterwards, the stacked time sections are converted to depth sections, using this. The transfer of the refraction velocity model to the reflection data was quite time consuming, since several ways had been tried out before the best and working solution was found. Another tricky point was merging profiles 99176 and 20010100 in order to convert both profiles together. The problems and solutions are explained in detail in the following chapters. This chapter should also have some kind of 'manual' character, so that following students may have a guide to depth conversion with sonobuoy models and the knowledge is not buried in oblivion.

6.1 Velocity model and VELMOD module

First, some equations explaining the basics of depth and time relations are introduced, that are necessary for the creation of depth models from data displayed as a function of time (v5.0 Focus Manual, 2002).

The velocity, v_b, at the base of a horizontal layer of thickness Δz, which contains vertical velocity gradients, is:

$$v_b = v + g\Delta z \tag{6.1}$$

where v is the velocity of the top of the layer and g the vertical gradient. The vertical one-way traveltime, Δt, across a layer with a nonzero vertical velocity gradient is defined with

$$\Delta t = \frac{1}{g} \ln \left(1 + \frac{g\Delta z}{v} \right) \tag{6.2}$$

rather than the usual form :

$$\Delta t = \frac{\Delta z}{v} \tag{6.3}$$

Equation 6.3 may be rearranged to give the thickness of a layer with a vertical velocity gradient and known one-way traveltime:

$$\Delta z = \frac{v}{g}(\exp(g\Delta t) - 1) \tag{6.4}$$

The usual form of this equation for layers without a vertical velocity gradient is:

$$\Delta z = v\Delta t \tag{6.5}$$

The XVMODEL module of RAYINVR supplies, next to model properties like the angle of the layers, either these time/velocity or time/depth pairs of the boundary layers at user defined x (offset) coordinates. These pairs must be stored, using a VELDEF disco job, in the seismic database at the CDP numbers corresponding to the sonobuoy positions, in order to link the velocity data with the reflection seismic data (see figure 6.1). Note, for storing velocities, it is required to load data, even if it is only one CDP. The CDP is set with HANDVEL, the time/velocity pairs go underneath.

```
*JOB    ARK2001 20010100
*CALL   DSKRD
namofil CDP     /awi8/data/20010100.stack
4320    4321
*CALL   VELDEF  CDP                     100sonoUTVRMS
HANDVEL 1135
0       1540    4820    1540    5420    1598    5930    1682
6340    1796    7310    2148    7500    2239    7700    2381
7880    2562    8800    3317
HANDVEL 4321
0       1500    5310    1500    5960    1562    6200    1609
6850    1772    7290    1955    7840    2367    8140    2683
8800    3215
```

Figure 6.1: VELDEF disco code, example

The FOCUS velocity utility then provides a table with all necessary parameters like time, RMS, interval, and average velocity, depth of the modelled layers for each CDP/sonobuoy position). Additionally, this velocity field can be viewed as well as the stored velocity model necessary for the NMO correction and stacking, and a first visual comparison of the two velocity models is possible.

If one now transfers the data to depth, the result is not satisfying. Although the sedimentary structure is relatively even, the undulating basement topography is not accounted for. Hence, some basement highs are assigned with sedimentary velocities. In addition, the 'square-edged' velocity model causes 'hard transitions' between different velocity layers (see figure 6.2). This results from the vertical stretch function applied during depth conversion, which also stretches the wavelengths.

The solution is to make a 'line-drawing' following the shape of the horizons and assign the corresponding velocities to them. This is possible with the VELMOD module of FOCUS.

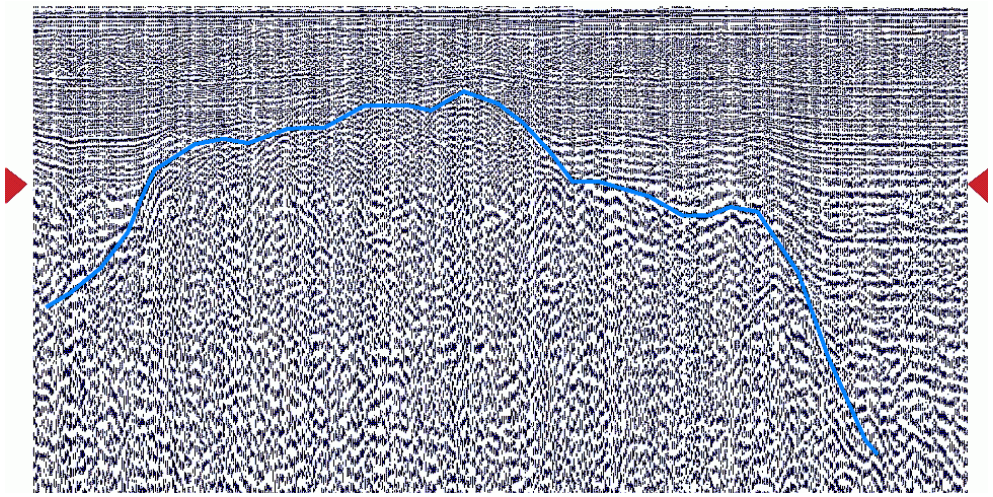

Figure 6.2: Example of a bad depth conversion. The blue line indicates the basement topography, the red triangles show a hard velocity boundary. Note the stretch in wavelength and that the basement has the same velocity distribution like the sediments above the boundary.

The problem here is, how to import the sonobuoy velocity model and how to superimpose it with the reflection data for comfortable horizon picking. A possibility is to simply import the stored velocity model and overlay it with a color code resembling the velocities. This visual help proved not to be accurate enough for picking and hard to distinguish at small velocity gradients. After a lot of tries, including FOCUS support and a short glance at the FOCUS source code, a partly-manual solution proved most effective.

The structure of VELMOD needs at least a pair of CDPs (here, two sonobuoys) for each horizon as well as the depth, the 'upper' velocity and the velocity gradient of the layer beneath these CDPs.

An effective way to obtain the input data is to print the velocity table for each buoy and to draw a depth/velocity function. The layer thickness and its velocity differences were noted from this, and the velocity gradient, $\Delta v/\Delta z$, was calculated (see figure 6.3).

After loading the VELMOD module and the reflection data, one must provide the database name of the velocity model and the horizons (add horizon parameter). This has to be done from top to bottom. Otherwise, if one inserts a horizon between others, the lower, already fitted, horizons will be slightly shifted.

First, horizon parameters for the ocean surface and water velocity must be entered (see figure 6.5), along the whole length of your profile. Activate the interactive mode of the VELMOD module in the processing sequence, and press 'go/process. The sea surface should be visible as a thin red line on the top of the section. The tool to create horizons is located in the VELMOD pull down menu (edit). Here horizons can be created, deleted and edited easily with the mouse by creating or deleting nodes along the horizon line (see figure 6.4).

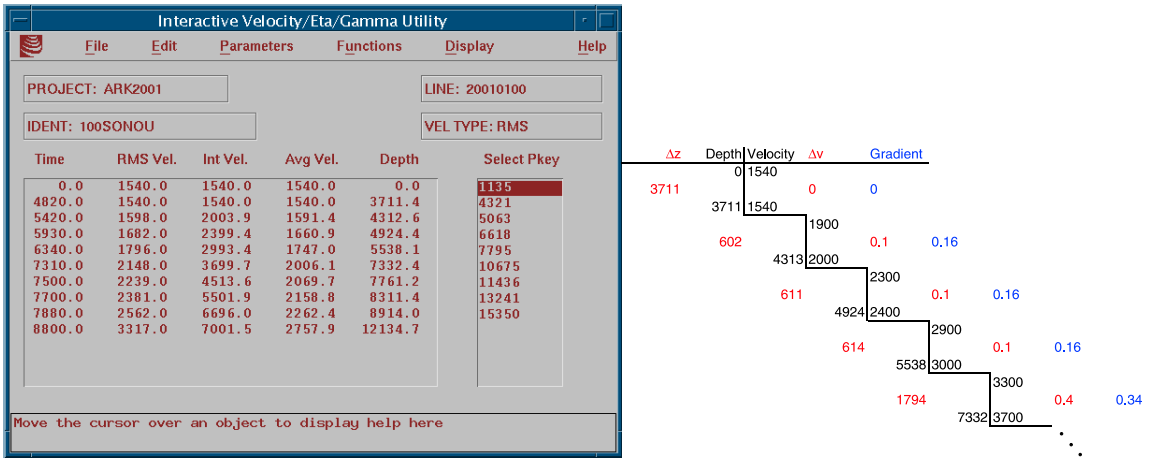

Figure 6.3: Table from the velocity utility and velocity/depth function.

The seafloor should be picked next, by creating a new horizon. One will be prompted to provide a velocity and a gradient. The user should either enter the one from the sonobuoy model, or a dummy one. The gradient can be altered later in the production window to supply different values for each sonobuoy. After creating the seafloor, successive horizons can be entered by hand in the production window of FOCUS. After compiling this job again, entering the horizon edit menu and choosing edit for the new horizon, the existing nodes should resemble the sonobuoy positions.

In order to fit the line to the reflections, it is a good idea to mark the sonobuoys with large mispicks (spikes) before or after. This assures an easy and fast way to find them again when the line consists of a multitude of nodes, rather than searching for the CDP numbers. After picking is finished, these markers should be cleared before moving on to the next horizon. The reflection data may be displayed in 'VA' mode, as in figure 6.4 with the picked velocity field superimposed on the data, but sometimes it may be easier to pick in 'density' mode.

The picking procedure can take some cpu time with long profiles (many CDPs). By making a set of 'orientation nodes', it is possible to load and work on smaller sections. Smaller sections otherwise have the potential problem of mispicking a horizon because the whole transect is not available for orientation. Sometimes it can be tricky which horizon to choose when the modelled layer boundaries do not fit on the same reflector at different buoys. If a reflector fitted 2 to 3 modelled layer boundaries, it was followed, even if it showed discrepancies at another buoy. Usually this difference was inside the fault tolerances.

It is not permitted to cross horizons, but horizons can start and end anywhere, for example if the basement cuts through the sediments. The VELMOD job can also be altered with text editors to merge or divide horizons. After creating the last horizon, the model is ready for the depth conversion.

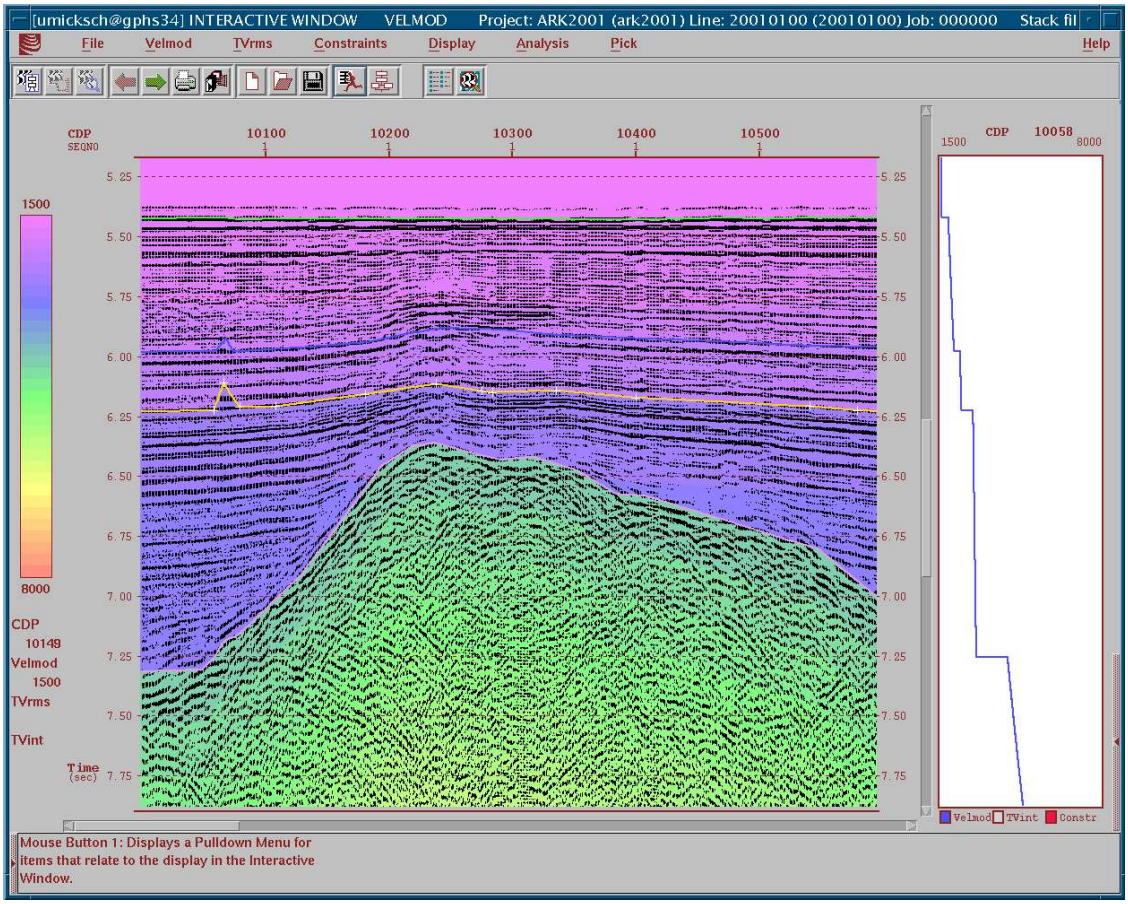

Figure 6.4: Picking horizons with VELMOD. Colored lines resemble the modelled and picked layer boundaries. White crosses show the picks done at the active horizon. The kink in the picked horizons is the described sonobuoy marker.

6.2 DEPCON module and depth conversion

The FOCUS module DEPCON converts seismic traces from a regular sampling in time to a regular sampling in depth, or vice versa, with a user-defined velocity model (streamer or sonobuoy origin). DEPCON uses a simple vertical stretch function given through the velocity model (v5.0 Focus Manual, 2002)

For the profiles in this thesis, a trace length of 10 000 m and sampling rate of 1 m was used. Plots of the depth-converted sections are shown in the next chapter with accompanying profile descriptions. The sections are shown in the appendix as well.

Problems occurred when merging profile 99176 and 20010100 for a joint horizon picking, because some CDP values were assigned double. Resorting of the data was not wanted, and the primary key variables (like CDP, SHOT) are limited in the VELMOD module in order to create a new primary key sequence for both profiles. The depth conversion was done

separately for each profile. The velocity-depth function of SB2101 and SB9938 are quite similar and therefore, the velocity model of SB2101 was forwarded to profile 99176, since the chosen reflectors to tie the velocities on can be followed visually over the transition without problems. The two depth sections are merged during the plotting job in the same way as for the time sections. The differences between the profiles lie in their processing sequence and profile 99176 was acquired with an active length of 2400 m (Geissler, 2001). This results in a visual effect in the plots of both profiles, noticeable in different shades of gray.

With the final, depth-converted profiles a variety of geologic interpretations and methods are possible. Subsidence calculations and roughness analysis, for example, will be demonstrated in the next chapters. The following figure (6.5) shows part of the job used for the VELMOD process and depth conversion.

```
*CALL   VELMOD  100FOCUSCDP
HORIZON SURFACE
12      0       1500    0
22217
HORIZON SEAFLOOR
12      3246    1900    0.16
53      3260
     ...
22207   3429
22217   3487
HORIZON HZ 1
13      3864    2300    0.16
29      3876
     ...
11937   4512
11970   4461
HORIZON basement
22      6697    4200    0.45
24      6919
     ...
22147   3484
22217   3735
*CALL   DEPCON  100FOCUS        10000   1
*CALL   DSKWRT  /awi8/data/100focus.depth
*END
```

Figure 6.5: Main parts of the depth conversion job. The velocity model is loaded, and the individual horizons are supplied with their 'upper' velocity and the gradient. Next, the DEPCON module is called and the result is written to disk.

7 Profile description

In this chapter, the results of previous data processing and interpretation are shown: The depth-converted seismic sections. The profile position, its structure and visual appearance is explained for all sections in detail. The reader is referred to the appendix with larger plots of the seismic reflection data set, if details of the figures are too small to be noticed comfortable. The depth sections are compressed horizontally very much due to the profile length of several hundred kilometers. The 'steep' part of the continental slope (until a depth of approx. 2300m) in profile 20010100 has inclinations of approx. 6°. 2000 CDPs equal 50 km. Figure 7.1 and figure 7.5 at the end of this chapter show overview maps of the profiles for orientation. Depth intervals are traced every 1000 m (white lines), the blue lineations represent the alignment of the magnetic chrons.

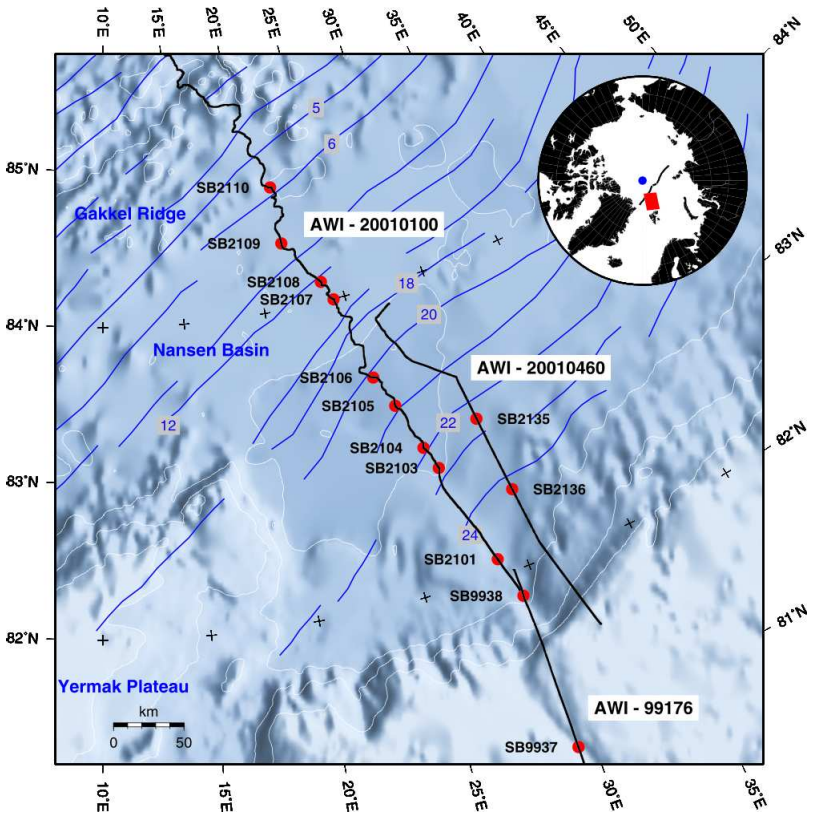

Figure 7.1: Overview map of profiles 20010100 and 20010460.

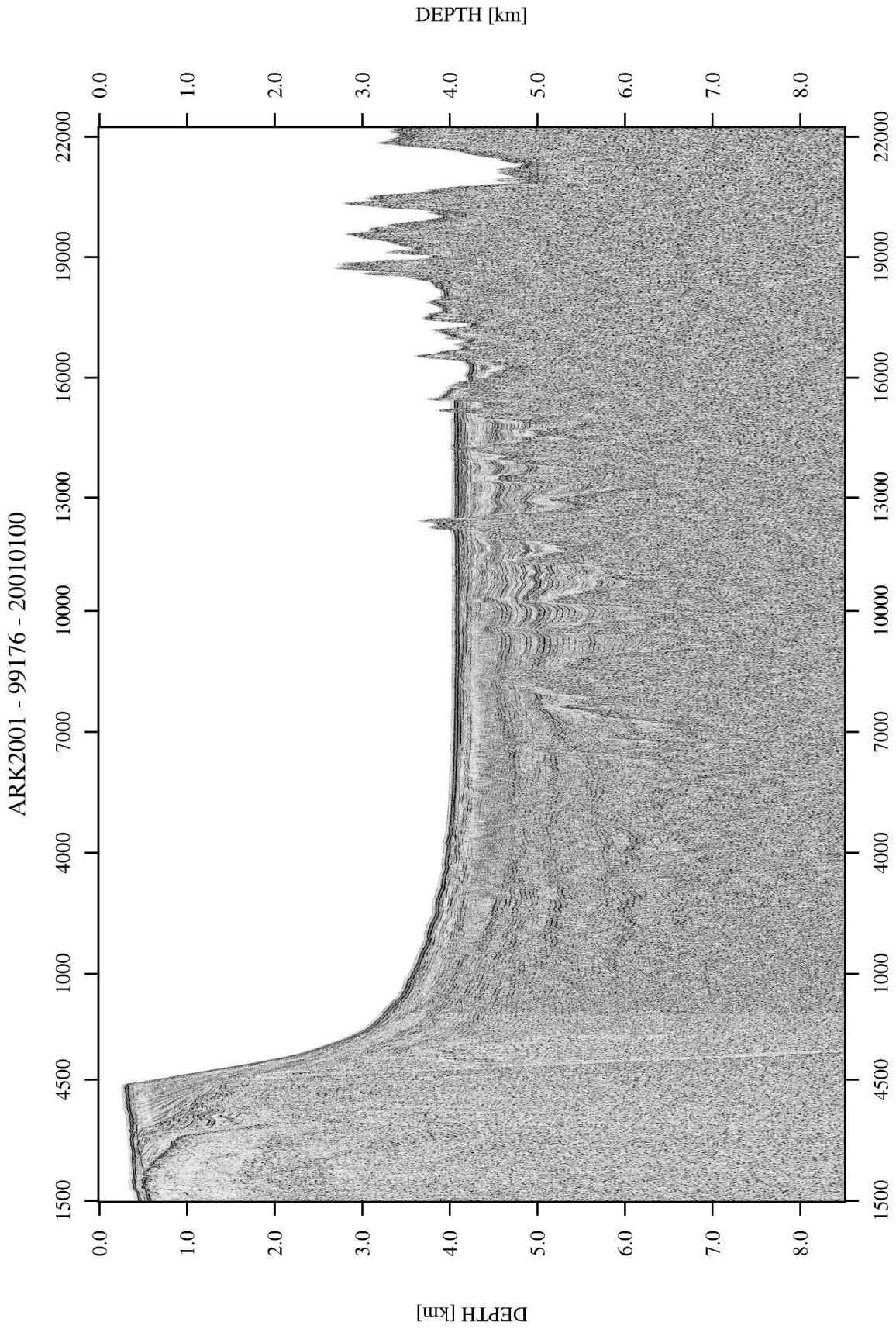

Figure 7.2: Depth section, 99176 and 20010100

7.1 Profile 99176 and 20010100

Figure 7.2 shows part of profile 99176, connected to profile 20010100. The whole length of the transect is approx. 670 km and begins on the Svalbard shelf at 80°50'N 29°22'E. Profile 20010100 starts shortly after the shelf break at 81°52'N 29°15'E and ends after reaching the Amerasian side of Gakkel Ride at 85°44'N 15°20'E.

The shelf side shows many distinct propagating sequences of glacial advances (grounded ice) and retreats extending the shelf and filling up Nansen Basin with accompanying slides and turbidity streams. Underneath, the basement shows a blocky structure with great detached blocks, possibly structures from the early rifting of GR. More information about profile 99176 and the glacial history can be obtained in Geissler (2001).

At the beginning of profile 20010100 (CDP 1 to 4000), the data quality is diminished due to coarse detritus brought by glaciers and material distributed by ice floes and icebergs originating from these glaciers. This effect is also noticeable in the recordings of 99176 close to 20010100, even though a longer active section was used. With increasing CDP numbers of profile 20010100 the data quality increases as well, rather rapidly around CDP 6000.

The sediments are up to 4.5 km thick close to the Svalbard margin and thin continuously towards Gakkel Ridge, until the basement crops out at CDP 15500. Afterwards, the sediments fill only the valley floors or are almost absent close to the axial valley. The Eurasian flank of Gakkel Ridge shows some pronounced basement highs around CDP 18000. Profile 20010100 meets with the axial valley of GR at 85°36'N 16°41'E in the sparsely magmatic zone, but right next to a focused volcanic center there. The modest hills on the the axial valley floor may be volcanoes.

The created oceanic crust along the whole basin is very rough, and the undulations have great wavelengths. Several basement highs have a wide extension, for example from CDP 7200 to 9000 or CDP 11000 to 13000. The latter zone even crops out of the sediments at CDP 12500. It does not seem that these basement highs acted as dams in the past, because the sedimentary structure is similar on both sides. This indicates that their extension in strike direction of GR is limited and that they might originate from strongly localized volcanic features as observed on the ridge during the AMORE cruise. The sediments coming from the Svalbard side are 'washed around'. Another possibility can be a main influx of sediment in strike direction of GR. A steady supply of sediments comes from dead organic matter and the melting of ice floes, if present, during summer.

Between CDP 1000 and 10000, in a depth of approx 4100 to 4400 m the quality of the seismic recording is impaired, associated with a large slumping area, whose origin is not certain. It seems, that the slumps came from a western direction, since a lesser thickness of this zone is visible in the neighboring, more eastern profile 20010460.

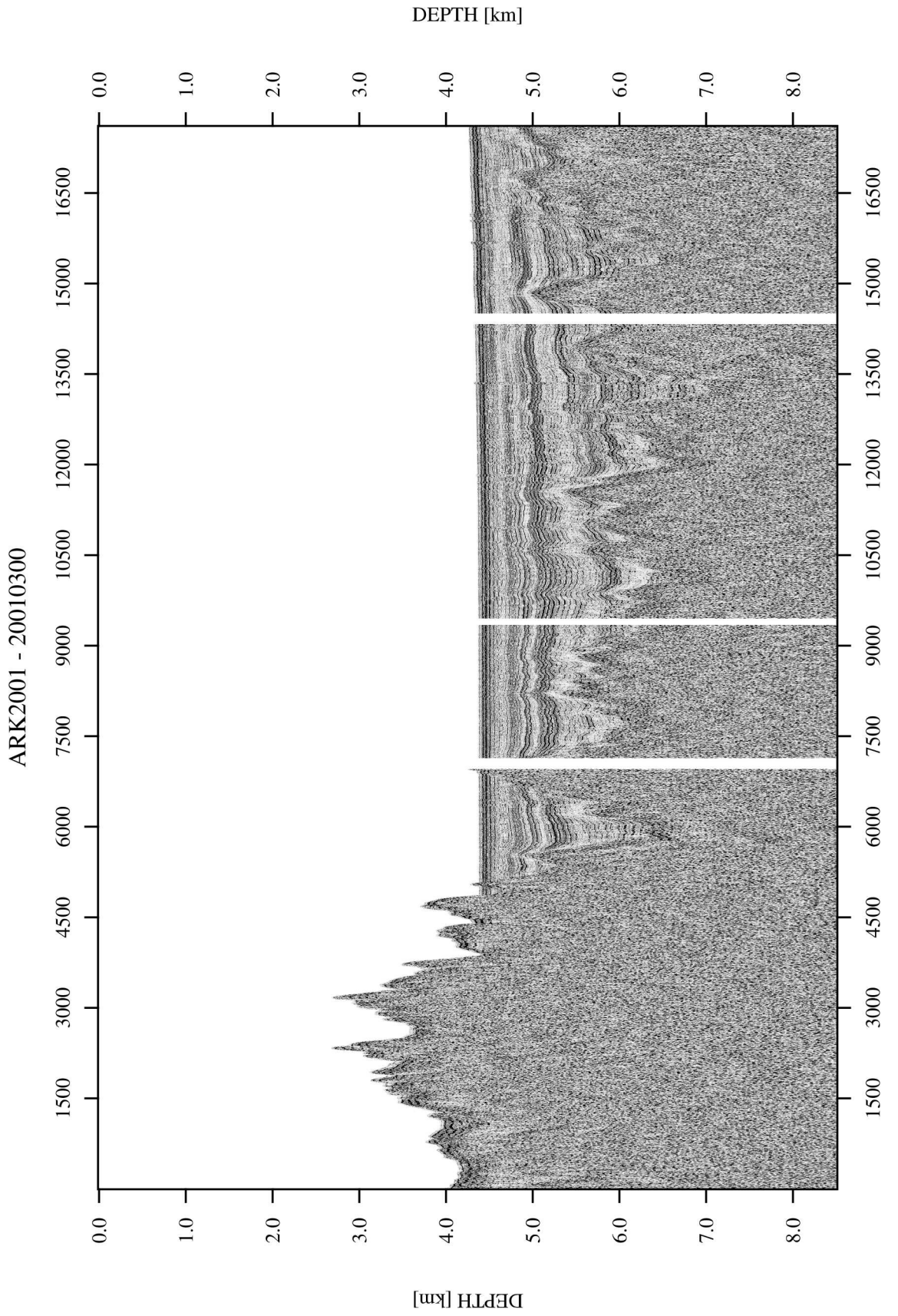

Figure 7.3: Depth section, 20010300

7.2 Profile 20010300

Figure 7.3 shows the acquired seismic transect in the Amundsen Basin (20010300). The length of this profile is approx. 440 km and it begins in the axial valley of Gakkel Ridge at 86°16'N 72°37'E. The profile was terminated close to the Lomonosov Ridge at 89°N 129°53'E.

The data quality (signal to noise ratio) is of a consistent good level throughout the whole transect and better than the quality of profile 20010100. This is certainly due to the far distances to costal or shelf regions, and therefore the lacking of coarser sediments in the area covered by the profile. Disturbances in the data are mainly caused by streamer depth variations because of more difficult ice conditions, encountered during profiling. This is visible around CDP 16000 at the end of the profile in a bulging of the seafloor, and can be followed along the whole trace length (here depth direction).

The transect starts in the eastern volcanic zone. Here, the axial valley is covered with sediments up to 1 km in thickness (CDP 1 - 1000). Oceanic basement of the ridge crops out at the seafloor for almost 100 km to the north (CDP1000-5000) showing only little sediments. After this, the top of the basement drops from 4.4 km to 6.5 km depth over a 15 km distance (CDP 5000 - 5600). The mean thickness of the sediments is around 1.7 km. Thicknesses greater than 2 km are only locally reached in the central part of the basin (CDP 5600: 2 km; CDP10000: 2.2 km; CDP13500: 2.8 km). The sedimentary layers dip slightly southwards towards Gakkel Ridge. The greatest inclination can be found in the layers on top of the basement between CDP 9500 and the end of the profile, especially visible in this horizontal compressed format. Their tilting angle numbers only approx 0.28°.

Towards Lomonosov Ridge, after CDP 15000, data quality is diminished, especially for the deeper sediments and the crust. This may be because of coarser, terrestrial sediments originating from the LR, deposited there, before the ridge was subsided below sea-level. This happened around chron 22 (50 Myrs) time (Jokat et al., 1995). The continent ocean boundary may be around CDP 16000. The basement may therefore be composed of metamorphosed or highly altered continental sedimentary rocks, instead of pure oceanic crust. This could explain the impaired visibility of the basement. The found seismic velocities are between 2.8 and 3.0 km/s (SB2129) for the top of the acoustic basement, which is not typical for 55 Myrs old oceanic crust. (basement = only oceanic crust; acoustic basement = crystalline continental crust or altered or metamorphosed sedimentary rocks).

The relief of the oceanic crust is equally rough as in the Nansen Basin, but lacking great undulations caused by buried seamounts, for example between CDP 7500 to 13000. Nevertheless, some prominent seamounts are existent, around CDP 7000 and 15000.

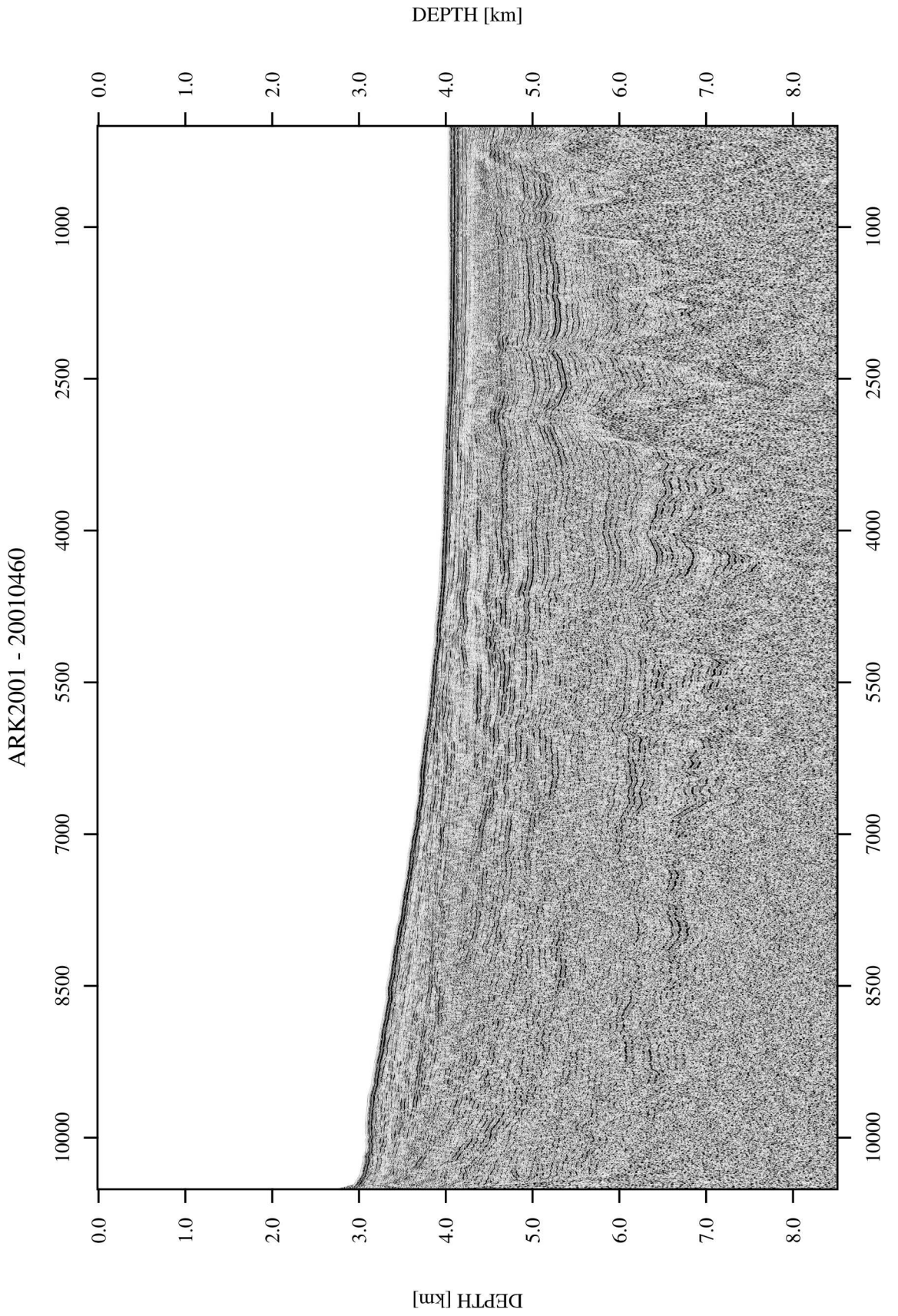

Figure 7.4: Depth section, 20010460

7.3 Profile 20010460

Profile 460 is shown in figure 7.4. This seismic line starts at 83°52'N 27°30'E in the Nansen Basin and recording was stopped at 81°29'N 32°3'E after crossing the shelf break close to Svalbard. The depth conversion was applied only to the basin part of that profile, because of the complex structure of the continental slope, showing extensive slump and channel systems. No reliable velocity model to use for the depth conversion could be developed for the shelf out of the sonobuoy recordings in the basin.

The data quality of the seismic data is similar to the one of profile 20010100, the visibility of the basement is worse after CDP 4500. Again, this is due coarser material deposited from the slopes. Several fans and slump or mud flow deposits are visible between CDP 5500 and end of the profile (beginning of the steeper continental slope).

The huge disturbed area from profile 20010100 is of lesser extent than in profile 20010460. The corresponding area can be found between CDP 4000 and the beginning of the profile in a depth of 4150 to 4250 m. The total extension towards GR was not imaged due to the starting point of the profile.

The thickness of the sediments ranges around 4 km and is thinning out in the direction of GR. The crustal relief is rough, the basement highs are not as pronounced as in the other profiles.

A common feature of all three profiles is a wavey pattern of the sediments, accompanied by variations in amplitudes above basement highs. This can be explained with the following scenario: The sediments fill up the 'valleys' between the basement highs and are deposited in flat layers above, as it can be seen at the current sediments, the seafloor. With the increase of sediments the unique layers are compacted due to this overburden. More compaction is possible in the valleys between the basement highs than directly over them. This causes depressions in the valleys and leads to fractures and faults along the slopes of the crustal highs. The compaction causes de-watering of the sediments and the fluids migrate along the fractures towards the top of these basement highs and further towards the seafloor (building of 'pipes' and 'seeps'). That reflectors with strong amplitudes suddenly show a low reflectivity over these highs, whereas other non-prominent reflectors close-by (above) are amplified is a typical pattern related to fluid migration and/or the existence of gas hydrates (Chand and Minshull, 2003).

In addition, 'blanking' of reflectors occurs in all profiles, for example, around CDP 5000 of profile 20010460, in a depth of 4.3 km along several hundred CDPs. Reflectors above this blanked zones are amplified as well. This pattern is associated with the existence of gas hydrates in the pore space of the sediments, which might be the cause for this blanking in the AMORE data (Chand and Minshull, 2003).

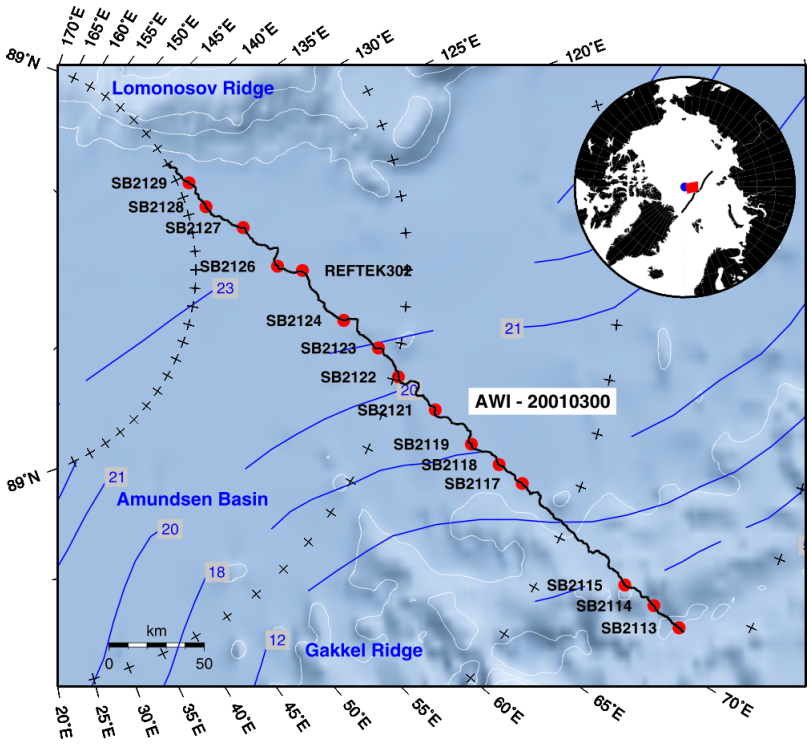

Figure 7.5: Overview map of profile 20010300

8 Line drawings

A line drawing of seismic data shows an interpretation of the most prominent reflectors, geologic or tectonic features, and additional information like velocity distributions in a very compact, but clearly arranged way.

Here, the main concern was to show the thickness of the sediments across Nansen and Amundsen basin, their major layers and corresponding seismic p - wave velocities, derived from the refraction data modelling. In addition, the magnetic chrons are marked, because they are important for the following subsidence and roughness analysis.

8.1 Illustration of the seismic data

A digital image of the seismic data was imported in a publishing program (CorelDRAW). The points of reference for all objects are the CDP numbers. Basement picks were made first, the prominent seismic reflectors were traced afterwards. Where their course was uncertain the line stops, or is continued with a dashed signature. The depth - velocity distributions for the sonobuoys were imported and placed at their corresponding CDP numbers.

The modelled boundaries fit, in general, to the traced reflections. The differences are within the fault tolerances and uncertainties from the sonobuoy modeling. As in the depth conversion process, more importance was attached to tracing continous reflectors than the boundaries from the refraction modelling. It is assumed that a prominent reflector, consistent in its appearance, has no lateral changes in velocity. Overall, this approach worked acceptably through all three profiles.

Figure 8.1 shows a stage in the creation of the line drawings. Part of the grey 'basement' fill has been moved to show the prominent transition between sediments and crustal structure. Tracing sedimentary horizons (blue lines) turned out to be more difficult. Some of the blue lines have been removed to show the data where the tracing should continue. The colored column resembles the time-velocity distribution from SB2109. Only the sedimentary velocities from the sonobuoys are shown by these columns in the line drawings. Velocities above 4.0 km/s are associated with the basement. For the first 2000 CDPs of profile 20010100, the basement topography is quite uncertain due to poor data quality caused by coarse sediments. Here, the model of SB2101 provided constraints for the visual interpretation of the basement

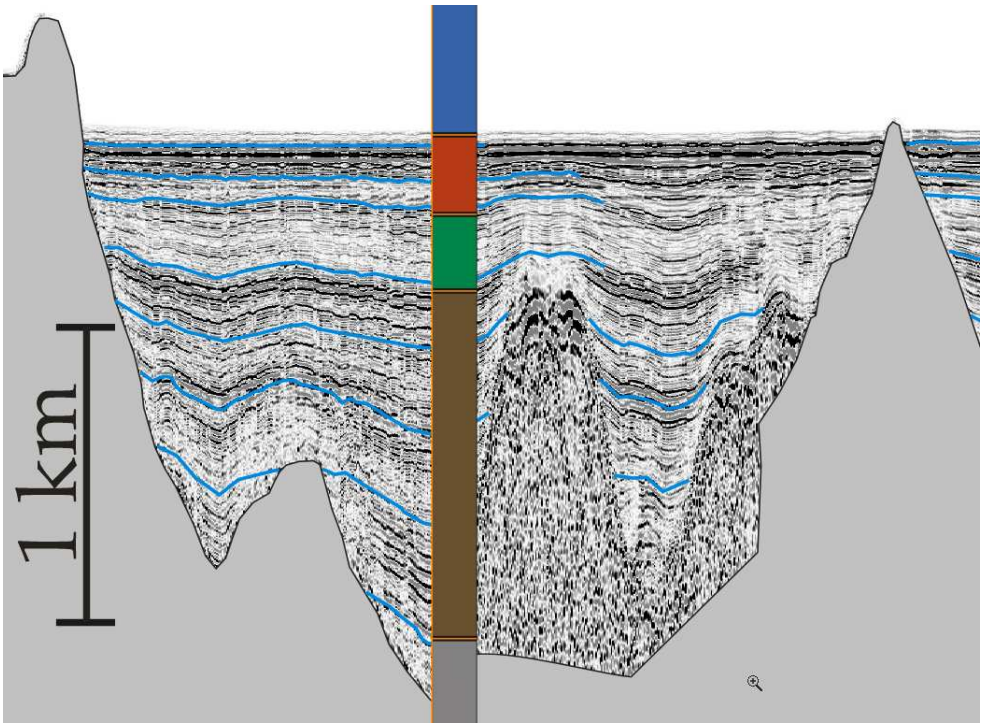

Figure 8.1: Part of profile 20010100 (area around SB2109) during the creation of the line drawing. The grey zone, resembling the basement, has been shifted to show the transition between sediments and basement. to the right of the colored column, the velocity model of SB2109, some horizons and the seafloor are not traced yet.

alignment. An additional feature to include in the line drawing of profile 20010100 was a large slump. The line drawings were created with great care, to minimize errors through mispicking or in the positions of the sonobuoys, for example. For this purpose, CorelDraw's layering and grouping facilities, as well as its excellent positioning accuracy with help-lines and rulers, were very helpful. The magnetic chrons were placed last.

8.2 The magnetic chrons

When the temperature of the magma at the ridge axis falls below its Curie point, the rocks acquire a thermo-remanent magnetization because they contain Ti-magnetite, $(Fe, Ti)_3O_4$. This happens at roughly 250 - 570 $°C$, depending on the content of titanium which lowers the Curie point temperature (Juteau and Maury, 1999). This fixed magnetization is parallel to the contemporary orientation of the Earth's magnetic field. Older parts of the crust, created in epochs with a reversed magnetic field, show therefore a reversed remanent magnetization. This is visible in the now classical image of linear anomaly stripes, alternately positive and negative, parallel to the ridge axis (Juteau and Maury, 1999).

The age of most reversals are well known today. The most prominent 'normal' (current polarization) periods are numbered as chrons 1 - 34, with anomaly 34 being a long period (35 Myrs) of normal polarization in the Upper Cretaceous. Earlier magnetic periods are numbered M0 - M33, until the Permian - Triassic period (Juteau and Maury, 1999). The nomenclature of 12y or 12o stands for the beginning (young) and ending age (old) of a chron, here chron 12.

The extent and distribution of magnetic anomalies related to each of the chrons is measured with magnetometers pulled behind ships or submarines, or beneath planes or helicopters. The first magnetic surveys in the High Arctic were started around around 1946 by Russian agencies and were followed by surveys from the North American (U.S.A & Canada) side. In the early sixties the first extensive airborne surveys were started by several polar and naval institutes from the U.S.A. and Canada (Grantz et al., 1990).

The magnetic anomaly identification used in this thesis was digitized from a map compiling tectonic features of the Arctic Ocean region, published in 'The Arctic Ocean region' by Grantz et al. (1990) (plate 11) and are based on the work of Karasik (1968) and Vogt et al. (1979).

The identified anomalies for the Acrtic Ocean span from 1 to 24. Between anomaly 24 and the physiographic margin of Lomonosov Ridge or Eurasia exist another 50 - 100 km, in which anomalies 25 - 28 were expected, but only a broad negative anomaly was found. This situation is explained with three possibilities: First, this area could be deeply subsided, possibly modified, continental crust. Second, the oceanic crust could have been formed at an early stage of spreading, with high enough spreading rates compared to the reversal frequency that no reversals are recorded in the crust. Last, the parts of the crust show the typical magnetic polarizations for anomalies 25 -28, but their magnetic expression was erased by deep sediment burial and heating (Vogt et al., 1979).

In the map of Grantz et al. (1990) only the most prominent lineations (5, 6, 12, 18, 20, 21, 22, 24) of the Cenozoic reversal pattern are marked in the vicinity of the seismic profiles from 2001. An enlarged map with a dense coordinate grid was created with GMT, to obtain the CDP numbers where the digitized magnetic lines cut the ship track. The intersection coordinates were established visually, and then plotted over the ship track and magnetic data, to check if the visual obtained values were accurate enough. With the shot-lists of the profiles, the corresponding CDP numbers for the magnetic chrons were picked out and transferred to the line drawings. Their ages after Harland et al. (1982), that were used for further calculations, are listed in the tables below (Table 8.1, 8.2 and 8.3).

The error in the position of the chrons comes from several sources : First, the error from flight navigation is given by Taylor et al. (1981) as $\pm$ 5 km. The error in the transfer to the map of Grantz et al. (1990) is given as $\pm$ 6 km. The error created during digitizing and transfer to the line drawing of a seismic profile can be given as an additional $\pm$ 3 km. The total possible error adds up to $\pm$ 14 km for each chron.

New aerogeophysical results and their interpretation, were published by Brozena et al. (2003)

(September), to late to obtain the data set and to include it in already done calculations in this theses. The magnetic anomaly identifications are generally similar to those of Vogt et al. (1979), but the denser sampling, improved navigation and greater geographical coverage improve isochron resolution (Brozena et al., 2003).

An example line drawing of profile 20010100 is shown in figure 8.2. All three line drawings will be shown after the subsidence analysis and the addition of the subsidence curves.

Profile 20010100		
chron #	age [Mys]	CDP
5	10	16584
6	20	15093
12	34	11609
18	42	9386
20	45	7971
22	50	4933
24	53	2550

Table 8.1: Chrons, ages and CDP numbers for profile 20010100

Profile 20010300		
chron #	Age [Mys]	CDP
6	10	1828
12	34	3930
18	42	6544
20	45	9108
21	48	10637
23	52	14327

Table 8.2: Chrons, ages and CDP numbers for profile 20010300

Profile 20010460		
chron #	Age [Mys]	CDP
20	45	1525
21	48	3162
22	50	4428
23	51.5	5374
24	53	6824

Table 8.3: Chrons, ages and CDP numbers for profile 20010460

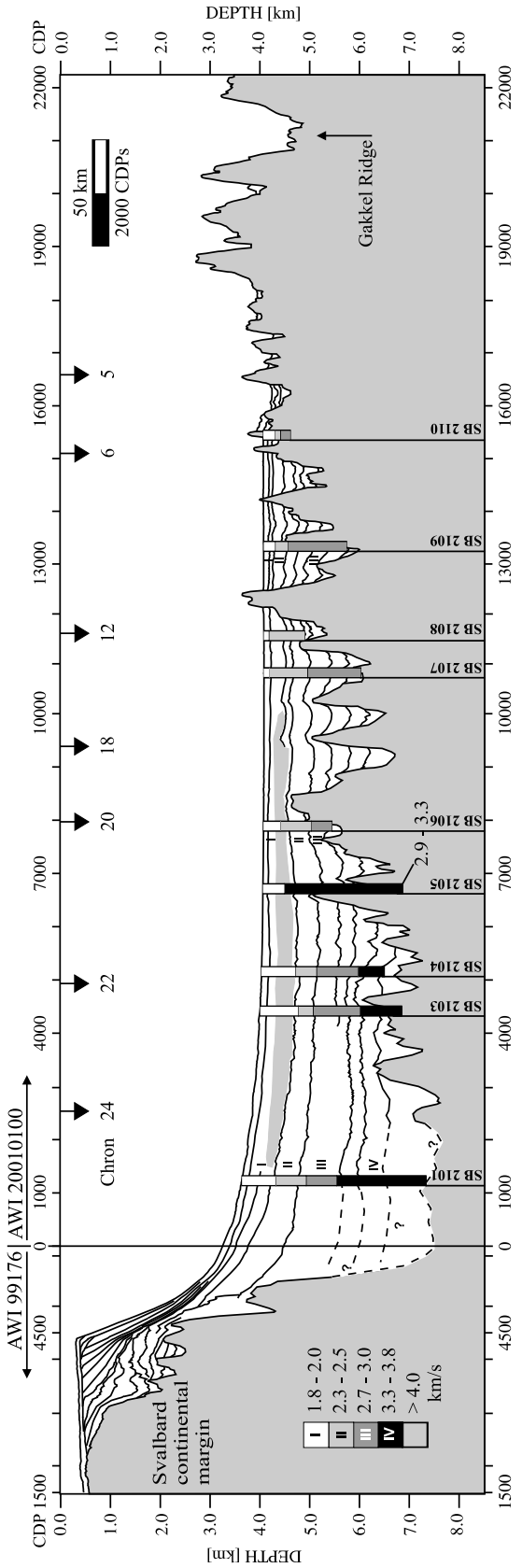

Figure 8.2: Example line drawing of profile 99176 and 20010100.

9 Subsidence of oceanic crust

The subsidence of sedimentary basins, and therefore, the depth and temperature history of their individual sedimentary layers is very important in terms of their oil or gas reservoir possibilities. For fundamental scientific research, the history of basins is important to create reconstructions of the initial situation, before extension or deformation processes, for example. The subsidence of Nansen and Amundsen Basin is interesting in terms of their differences and common features. Do the basins fit the model subsidence curve or was there some influence to prevent normal subsidence? Are differences in the spreading velocity or the slightly asymmetric spreading rates of Gakkel Ridge visible in subsidence history?

As the newly built oceanic crust is conveyed away from the mid oceanic ridge (MOR), the hot rocks begin to cool and to contract. The denser older rocks sink back into the mantle to maintain isostatic equilibrium. The cooling is caused by heat loss through thermal conduction and the majority of thermal energy is dissipated through the circulating of oceanic water (thermal convection), creating black smokers for example (Press and Siever, 1994). Some rock fragments from a black smoker chimney were dredged from the ridge flanks during the AMORE cruise, showing the typical mineralized composition of these thermal vents. In addition, unexpectedly abundant hydrothermal activity was found at the ridge, not expected in this amount (Dick et al., 2003). Before the cooled oceanic crust is recycled in subduction zones, about 180-200 Myrs must pass by (Juteau and Maury, 1999).

The subsidence of oceanic crust due to thermal processes is described in a the model by Parsons and Sclater (1977). Since the influx of sediment or the deposition of dead organic matter is always present in the oceans, the thermal subsidence is altered because of this additional burden. This means, the crust submerges earlier to deeper levels than without sediments. Several corrections of the thermal subsidence model, to take account of the sediment loading, have been published. Here, the approach of Allen and Allen (1990) is used to include the effects of the sedimentary cover.

Alternative subsidence models are given in the literature for sedimentary basins in continental crust. They consider tectonic influences like crustal thinning through extension (McKenzie, 1978) or crustal thickening through magmatic underplating or intrusions (Hübscher, 1994). Further on, phase changes from gabbro to eclogite in the lower crust (density change of 0.5 $\cdot 10^3 kg/m^3$ at a constant total mass) alter the subsidence mechanism and can be included. Other models include also the presence of hot-spots and pressurized flows in the asthenosphere, preventing the 'standard' subsidence. Here, only the sediment load is taken in account, since

the basins are not thought to have been altered through competing tectonic influences.

In the next sections, theory, results and interpretation of the subsidence calculations for the Arctic ocean basins is explained in detail.

9.1 Theory

9.1.1 Thermal subsidence after Parsons and Sclater

In order to set up a subsidence model, a number of starting parameters are are needed. Figure 9.1 gives an overview of the tectonic setting and the used nomenclature. z is the depth variable, density is coded with ϱ. w, l, a, r are indices for water, lithosphere, asthenosphere and ridge. Thickness of a layer is coded with d. In addition, two isostatically-compensated columns are shown, one at the ridge, and one on the the flank of the ridge. Each column extends from the surface to the depth of isostatic compensation, D. They have the same mass M per unit area, because the older column contains water (lesser density as astenospheric rocks) to offset the weight of cooler and therefore more denser lithospheric rocks. Isostatic compensation is possible due to the ability of the mantle to act like a fluid on geological timescales (Eisbacher, 1996).

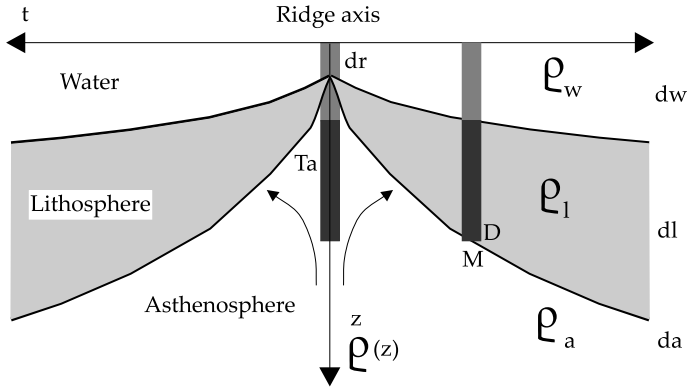

Figure 9.1: Sketch explaining variables and settings for subsidence calculation

The following assumptions were made to calculate the subsidence:
At mid ocean ridges, the lithospheric thickness d_l and age t equal zero. D is the isostatic compensation depth, and the mass M of the overburden layers is independent of the distance to the spreading axis. This leads to (Hübscher, 1994):

$$M = \int_0^D \varrho(z)dz \tag{9.1}$$

Directly above the spreading center (ridge axis), M is given through:

$$M = \int_0^{d_r} \varrho_w dz + \int_{d_r}^{D} \varrho_a dz \tag{9.2}$$

with d_r, the thickness of the water column above the ridge.
For a lithospheric thickness $d_l > 0$ ($t > 0$), it follows that

$$M = \int_0^{d_r} \varrho_w dz + \int_{d_r}^{D} \varrho_a dz = \int_0^{d_w} \varrho_w dz + \int_{d_w}^{d_w+d_l} \varrho(z) dz + \int_{d_w+d_l}^{D} \varrho_a dz, \tag{9.3}$$

which gives us :

$$\begin{aligned}(d_w - d_r)(\varrho_a - \varrho_w) &= \int_{d_w}^{d_w+d_l} \varrho(z) dz - d_l \varrho_a \\ &= \int_0^{d_l} \varrho(z) dz - \int_0^{d_l} \varrho_a dz \\ &= \int_0^{d_l} (\varrho(z) - \varrho_a) dz\end{aligned} \tag{9.4}$$

$\varrho(z)$ is a function of depth and temperature. T_a is the temperature at the spreading axis of $1300°C$. Further, it is assumed that

$$\varrho(T) = \varrho_a(1 - \alpha(T - T_a)). \tag{9.5}$$

$\alpha = 3 \cdot 10^{-5}\ °C^{-1}$ is the thermal expansion coefficient. The temperature variation in the lithosphere is given by

$$T(z,t) = T_a\ erf\ \left(\frac{z}{2\sqrt{\chi\ t}}\right) \tag{9.6}$$

with the thermal diffusity, χ, of $10^{-6}\ m^2 s$, and the error function erf. These equations lead to:

$$d_w = d_r + \frac{2\varrho_a \alpha T_a}{\varrho_a - \varrho_w}\sqrt{\frac{\chi\ t}{\pi}}. \tag{9.7}$$

$d_r = 2.5$ is a standard depth at the ridge axis, generalized over worldwide spreading centers. The density values used are $\varrho_w = 1.03 \cdot 10^3 kg/m^3$, and $\varrho_a = 3.30 \cdot 10^3 kg/m^3$. t is the age of the crust in Myrs (other variables see above).

With these values, the following equation, well known from the literature is derived (Parsons and Sclater, 1977). It gives the thickness of the water column above the seafloor, and therefore the depth of the crust due to thermal subsidence. It is valid for oceanic basins with an age

up to 70 Myr, which equals a depth of ∼5.4 km. This equation was used in my calculations, because initial rifting at Gakkel Ridge started about 60 Myr ago.

$$\boxed{d_w = 2.5 + 0.35\sqrt{t}} \tag{9.8}$$

Older basins satisfy the following relation (Parsons and Sclater, 1977):

$$d_w = 6.4 - 3.2\ exp\left(\frac{-t}{62.8}\right) \tag{9.9}$$

9.1.2 Sediment corrected subsidence after Allen and Allen

In the following section, the crustal subsidence due to a sedimentary cover is calculated after Allen and Allen (1990). The sedimentary cover is replaced by a corresponding water column which must be subtracted from the sediment thickness to obtain the depth of the crust (S_s) without the overburden sediments.

If the sediments are covered with a water column like in the oceanic basins, S_s must be added to the crustal depth obtained after equation 9.8 (Parsons and Sclater).

Reasonable assumptions concerning the sediment densities are essential, obtainable in two ways. First, the Nafe-Drake curve (Fowler, 1990) can be used, which relates density to p and s wave velocities. These could be taken from the depth-velocity distribution of the sonobuoy models. However, for a huge sediment load it is more suitable to include the depth related compaction of the sediments. Sawyer (1985) introduces a method to obtain sediment densities, which includes porosity and sediment grain packing. The calculated sediment densities must be inserted in the model of Allen and Allen (1990).

If sediments are compacted, the porosity decreases. The depth related porosity $\Phi(z)$ is given by Sawyer (1985) with:

$$\Phi(z) = \Phi_0 e^{-cz}, \tag{9.10}$$

where Φ_0 is the porosity at the top of the sedimentary layer, and c is the compaction coefficient. With the new index 's' for the sediment, the depth-related density results from :

$$\varrho_s(z) = \Phi(z)\varrho_w + (1 - \Phi(z))\varrho_g). \tag{9.11}$$

Here, ϱ_g is the sediment grain packing. The average density, ϱ_s, of a sediment layer in the depth interval z_1 (top) to z_2 (bottom) with the same grain packing is given by :

$$\varrho_s = \int_{z_1}^{z_2} \frac{\varrho_s}{z_2 - z_1} dz = \varrho_g + \frac{\varrho_w - \varrho_g}{z_2 - z_1} \int_{z_1}^{z_2} \Phi(z) dz \tag{9.12}$$

Solving this integral leads to the non-linear relation of (Hübscher, 1994):

$$\boxed{\varrho_s = \varrho_g - \frac{\varrho_w - \varrho_g}{z_2 - z_1}\frac{\Phi_0}{c}(e^{-cz_2} - e^{-cz_1})} \tag{9.13}$$

After obtaining the sediment densities, the overburden sediment layer, d_s, must be replaced with a water column, $d_{w_{aa}}$, as shown by Allen and Allen (1990):

$$d_{w_{aa}}\varrho_w + (d_s - d_{w_{aa}})\varrho_a = d_s\varrho_s \tag{9.14}$$

is transferred to

$$\boxed{d_{w_{aa}} = ds\frac{\varrho_a - \varrho_s}{\varrho_a - \varrho_w}} \tag{9.15}$$

which is the thickness of the water column to replace the sediments. The corrected depth for crust with overlying sediments is given through:

$$\boxed{S_s = d_s - d_{w_{aa}}}. \tag{9.16}$$

The resulting values from equation 9.16 must be added to those from equation 9.8 to obtain the final theoretical depth of the oceanic crust to be compared with the acquired data.

9.2 Calculation and illustration

Crucial for all the subsidence calculations is an accurate age model, since the main parameter is geological time (see equation 9.8). The time constraints are obtained through the magnetic sea floor spreading anomalies. Therefore, absolute depth values could only be calculated at these magnetic chrons. Afterwards, the data were fitted with a quadratic function, resulting in an interpolated subsidence curve showing the theoretical crustal depth over time. The result was superimposed on the line-drawings.

But first, the sediment densities were calculated using the sediment thickness obtained from the depth conversion of the seismic data, visualized in line-drawings. The thickness was simply measured at the positions of the chrons on enlarged plots. The uncertainty in this measurement is ± 10 m (= 0.05 cm on the plot) and can be ignored, in comparison to the much bigger errors resulting from the positions of the magnetic lines. Sometimes, the chrons coincide with basement highs. Since these are not always representative of the sediments buried in the basin, the thickness was measured close to them. This is practicable, because of the uncertainty in the location of the chrons, and the widespread magnetic anomaly they represent. For example, in figure 9.2, chrons 5 and 6 occur over a basement ridge, so sediment thickness was measured in the vicinity of the chrons (red dots). At chron 12, the distance from the base of the seamount to the sediments was considered too far off, and the seamount itself must have a prominent influence in local subsidence, so the lesser sedimentary thickness was taken in account.

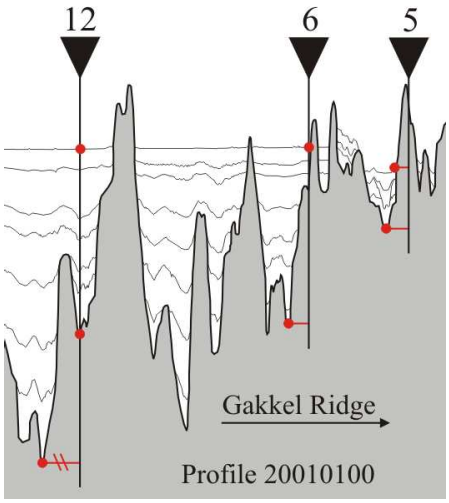

Figure 9.2: Picking sediment thicknesses for subsidence calculation

In addition to top and bottom depths of the sediments, equation 9.13 requires values for porosity, grain packing and compaction coefficients to asses the mean density of the sediment column. For these, Sawyer (1985) also gives examples and ranges, shown in the following table (see table 9.2). The table also shows the values adapted here, which were chosen after sensitivity tests using the values from Sawyer (1985) and the available literature. For example, Kim and Kim (2001) provide a comparisons of physical properties from a detailed analysis of plain and slope sediments in the Sea of Japan. The values for the densities of water and

parameter	Sawyer	used values
Grain size, ϱ_g $[to/m^3]$	2.50 - 2.70	2.60
Porosity, Φ_0	0.25 - 0.75	0.75
Compaction coefficient, c $[km^{-1}]$	0.30 - 0.60	0.50

Table 9.1: Sediment parameters used during subsidence calculation

asthenosphere selected by Sawyer (1985) as well as by Parsons and Sclater (1977) ($\varrho_w = 1.03 \cdot 10^3 kg/m^3$, and $\varrho_a = 3.30 \cdot 10^3 kg/m^3$) were also used to provide a comparable standard.

The calculated sediment densities obtained with equation 9.13 were put to equation 9.15 for the compensating water column, and then the depth of the crust without sediments was calculated with equation 9.16 (boxed equations). This term must be added to the depth values obtained after the thermal model from Parsons and Sclater (1977), equation 9.8. The resulting values were plotted and fitted with a quadratic regression, listed in the tables below (Table 9.2, 9.3 and 9.4). The corresponding thermal subsidence values are used, if no sediments are present. The error in the horizontal position of the curves rise up to ± 150 m when using extreme values for the variables found in literature. For more modest and common values a error of ± 75 m can be given for the curves. The obtained curves were transferred to the line drawings of each profile, completing these.

Profile 20010100				
CDP	thermal [km]	corrected [km]	age [Myrs]	chron #
2550	5.12	7.20	53	24
4933	5.05	6.94	50	22
7971	4.91	5.87	45	20
9386	4.83	6.48	42	18
11609	4.60	5.35	34	12
15093	4.11	4.84	20	6
16584	3.64	3.85	10	5
21100	2.50		0	0
$y = 7.4092 - 7.2017 \cdot 10^{-05}\ x - 7.8382 \cdot 10^{-09}\ x^2$				

Table 9.2: Values for subsidence curve and corresponding fit equation, profile 20010100

Profile 20010300				
CDP	thermal [km]	corrected [km]	age [Myrs]	chron #
300	2.50		0	0
1828	4.07	no sediment	20	6
3930	4.54	no sediment	34	12
6544	4.77	5.43	42	18
9108	4.85	5.77	45	20
10637	4.92	6.06	48	21
14327	5.02	6.32	52	23
$y = 2.6839 + 5.5224 \cdot 10^{-04}\ x - 2.132 \cdot 10^{-08}\ x^2$				

Table 9.3: Values for subsidence curve and corresponding fit equation, profile 20010300

Profile 20010460				
CDP	thermal [km]	corrected [km]	age [Myrs]	chron #
6824	5.05	7.14	53	24
5374	5.01	7.48	51.5	23
4428	4.97	7.46	50	22
3162	4.92	6.60	48	21
1525	4.85	6.69	45	20
$y = 5.8947 + 4.9287 \cdot 10^{-04}\ x - 4.2913 \cdot 10^{-08}\ x^2$				

Table 9.4: Values for subsidence curve and corresponding fit equation, profile 20010460

9.3 Line-drawings and subsidence curve

The following figures (9.3 to 9.5) show the created line drawings with the superimposed subsidence curves, marked in red. The calculations could only be carried out between identified magnetic chrons, providing the required ages. For other parts of the crust, the curves were interpolated (dashed signature). The positions of the sonobuoys and their p - wave velocity model are displayed in columns. Their color code is explained in the legend on the left side of the figure, the roman numbers are given for orientation. The basement starts with velocities greater than 4.0 km/s. The error in depth of the subsidence curves can be given with ±75 m. The dashed area in the basement of profile 20010300 towards Lomonosov Ridge marks the possible continent-ocean transition zone between AB and LR.

In the Nansen Basin, the subsidence curve fits the top of the basement reasonable well for both acquired profiles (20010100 and 20010460). The subsidence of the whole basin along the profiles was therefore normal and not altered.

Locally, the huge basement highs (i.e. profile 20010100, CDP 7500 and 12000) were not subsided as deep as the surrounding sections of crust. This sustains the idea, that they might be old specimen of the localized and temporary volcanic centers found in the sparsely magmatic zone on GR. They may mainly consist of basaltic and effusive volcanic material with a lot of cracks and fissures, reducing their density. The adjacent crustal parts could then be created by the accretion of asthenospheric material (i.e. peridotites) and only little volcanism, during phases when the centers are extinct. Their greater density could result in the observed, deeper subsidence than the one of the huge basement highs. In addition, lesser sediment to suppress them is deposited above them.

The basement depths of the Amundsen Basin also fit to the theoretical subsidence curve. Some deviation can be found at the beginning of the profile over the Amerasian flank of GR (CDP 2000 - 5000). This might be explained by a drop in half spreading rate around chron 15/13 time (37 Myrs) from 5.9 to 3 mm/a. Reliable evidence for a connection between spreading rate and subsidence for the Eurasia Basin can't de given with the AMORE data-set. The slight asymmetric spreading cant' be resolved either. More information on the spreading regime of GR will be given in the following section about crustal roughness. The subsidence curve, as a representative trend of the basement depth, is a major parameter in crustal roughness calculation.

Weigelt and Jokat (2001) show subsidence curves for seismic transects in the NB and AB, acquired in 1991. The profile locations are shown in the overview map of the survey area (see appendix) as black lines crossing the basins. The calculated subsidence curves fit the basement as well, whereby only the thermal subsidence was accounted for in areas close to the ridge (few sediments). For the deeper part, the basement was approximated with a linear trend.

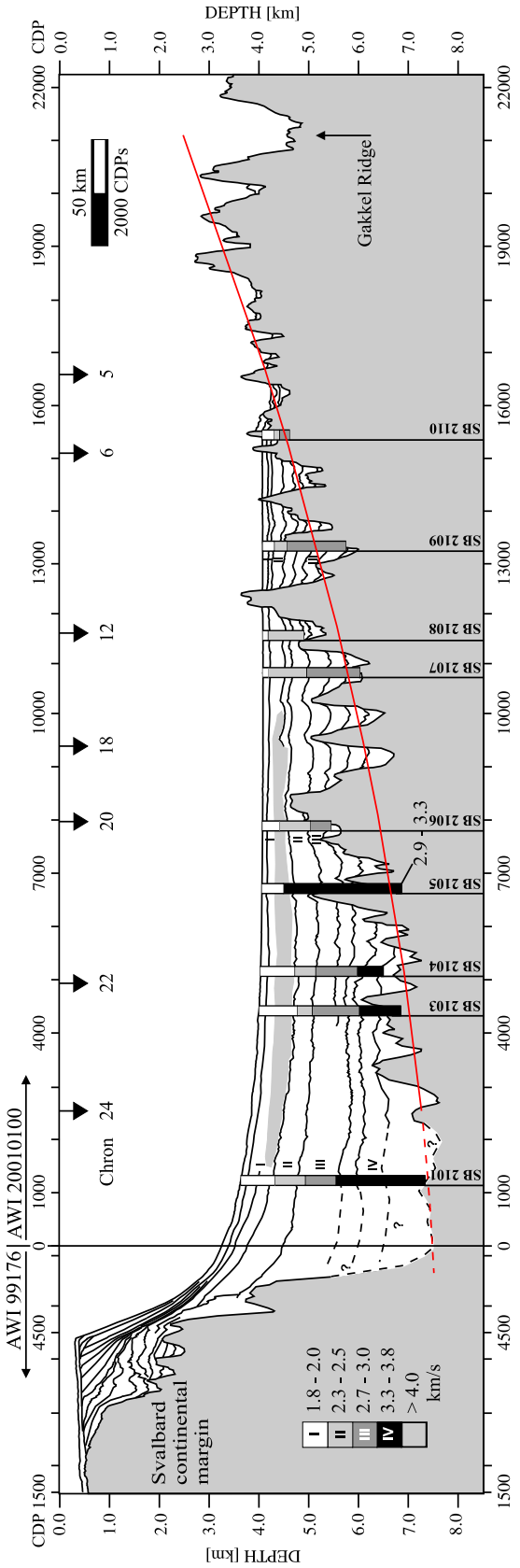

Figure 9.3: Line drawing of profile 99176 and 20010100

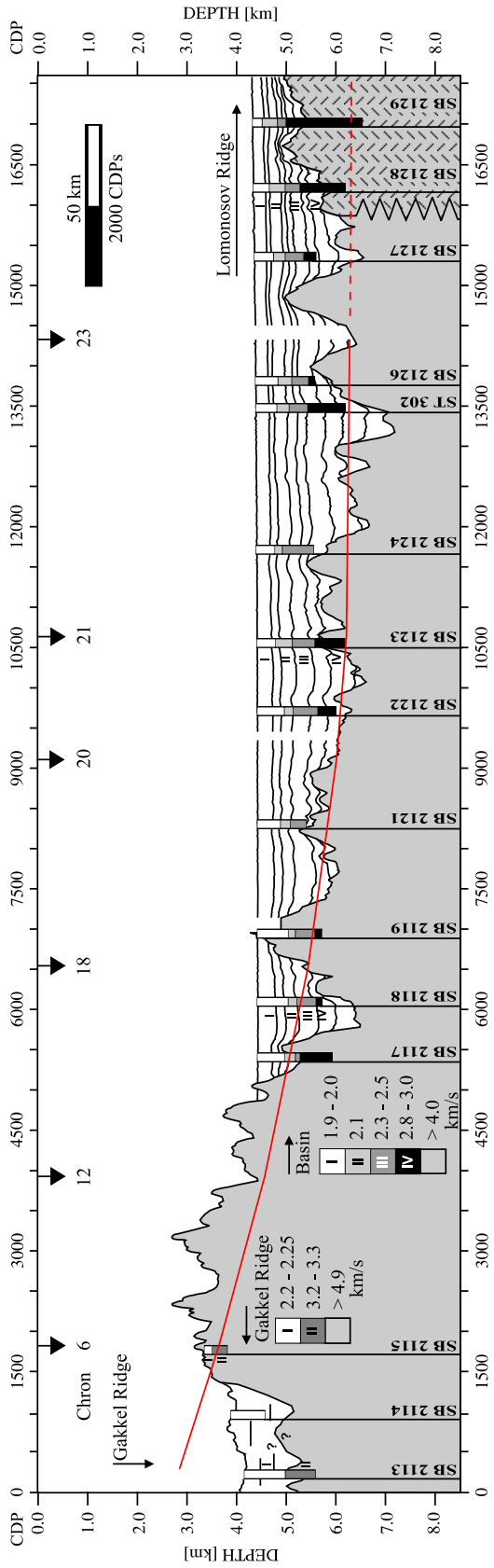

Figure 9.4: Line drawing of profile 20010300

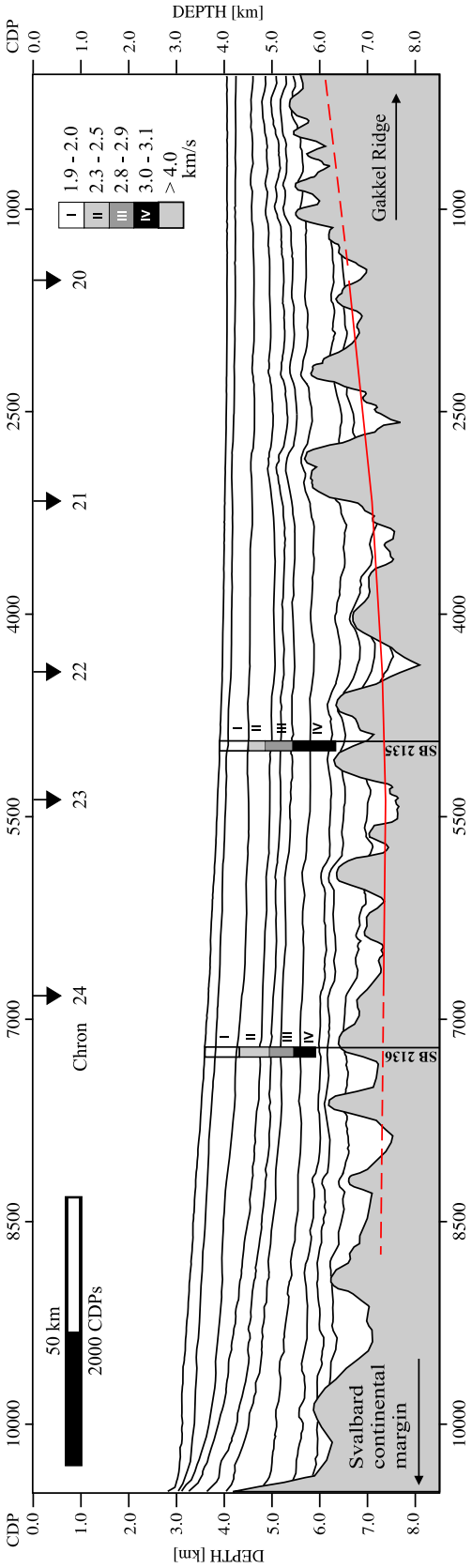

Figure 9.5: Line drawing of profile 20010460

10 Roughness of the oceanic basement

Another tool to understand ocean ridge processes in the past and present is the calculation of crustal roughness. Several studies have been made in the past years to tie the roughness to other ridge parameters like spreading velocity, crustal thickness, faulting or segmentation for a better understanding of the tectonic evolution of oceanic ridges (Malinverno, 1991; Hayes and Kane, 1991; Goff, 1991; Malinverno and Cowie, 1993; Small, 1994; Minshull, 1999; Chen, 1992). The existence of a relation between spreading rate and roughness was mentioned by Sclater and Francheteau as early as 1970.

Because of the known problems of obtaining data in the polar regions, extensive roughness calculations were lacking there. Recent work in these regions, including roughness calculations, has been done by Rogenhagen (2000) (Antarctica, Weddell Sea) and Weigelt (1998) (Arctic Ocean). The unique slow spreading Gakkel Ridge, with its adjacent basins, is of special interest because existing global roughness models lack data from ultra slow spreading centers (< 11 mm/y half rate). The calculated values are compared to ones published by Weigelt and Jokat (2001) and correlated to the global data.

10.1 Background and existing data

The imprint of spreading velocity can be seen right at the ridge axis in a very distinct way. Fast spreading ridges, such as the East Pacific Ridge show a central high, whereas slow and ultra-slow ridges have a deep axial valley. In case of the Gakkel Ridge, the central valley is up to 5 km deep (Gauger, 2002). The reason for these differences can be found in the viscosity of the magma underneath, which depends on temperature and composition of the melt. Fast cooling increases the viscosity and therefore results in lower crustal production rates and slower spreading (Sleep and Rosendahl, 1979). There is still a ongoing discussion about ridge push versus slap pull at subduction zones as a control for spreading velocities and spreading itself, but slap pull seems to be the major driving force. So, a small spreading velocity could also mean a small or lack of slab pull.

For Gakkel Ridge, the major reason for a slow spreading seems to be the relative slow moving Eurasian and North American plate in respect to the the global tectonic setting (Vogt et al., 1979). In addition, these plates are not subducted anywhere in large amounts to initiate slab pull. The close setting of the ridge to the point of rotation (Euler pole) of the surrounding

lithospheric plates also results in low angular velocities and therefore, slow spreading. Petrological particularities in the composition of the up-welling material also contribute to this ultra slow spreading (Michael et al., 2003). The whole mechanism of ridge processes, especially at slow spreading centers is still not understood in total.

For roughness calculations, the shape of the crust over time is necessary. Close to the ridges, the shape can be mapped simply by bathymetric surveys, since sediments are thin or absent. In the abyssal plains, seismic recordings are needed to penetrate the sedimentary cover. Studies that relate roughness to spreading rate have used different statistical methods, but all come to the same conclusion: Slow spreading, and therefore small spreading rates, results in rough crustal topography. In seismic data, this will be seen as rough basement topography.

After an analysis of around 100 global bathymetric profiles across MORs, Malinverno (1991) derives a power law, that is confirmed by Small (1994) who worked on 135 profiles. According to Small (1994), there is no significant decrease in roughness for half spreading rates over 40 mm/y, indicating a linear trend, which comes close to a power law as described by Malinverno (1991). Hayes and Kane (1991) even draw this border at 30 mm/y (half rate). Other authors like Goff (1991), Ranero et al. (1997) or Henstock and White (1996), contribute several values, not sufficient enough to construct a new dependance and their calculated values fit in with the model of Malinverno (1991) (see equations and figures below). Topographic roughness can also be measured along axis of the ridge itself, where the same correlation between slow spreading rates and rough axial topography is seen.

10.2 Theory

After the broad introduction it remains to show what roughness means mathematically. Topographic roughness, R, is defined as the RMS deviation of the residual basement relief, h, along a given length of the profile, measured at equidistant positions (Malinverno, 1991).

The following equation is used for calculating the roughness, R (Malinverno, 1991):

$$R = \sqrt{\sum_{i=1}^{n} \frac{h_i^2}{n}}\ , \quad \text{for i=1,2,...n,} \tag{10.1}$$

in which h is the difference between the subsidence curve and the basement. The power law describing the relationship of roughness, R, and full spreading rate, v, is given by Malinverno (1991) as:

$$R = 1296 \cdot v^{-0.539}. \tag{10.2}$$

The reference level to obtain the residual basement relief can be a linear trend of the basement (Malinverno and Cowie, 1993) or the subsidence curve (Hayes and Kane, 1991). After comparing both possibilities, here the subsidence curve is used. It provides a better fit of the

basement characteristics than a linear trend, applied over several hundred kilometers. The chosen length of the profile section, and thus the number, n, of measurements should exceed some tens of kilometers, preferable about 100 km (Malinverno, 1991), to overcome problems of self affinity and influences of the chosen window borders.

Malinverno (1991) also mentions the possibility to calculate roughness inside a window (length approx. 100km and more) sliding along the profile, the median of the obtained values gives the final roughness. This technique is not suitable due to the tectonic settings of Gakkel Ridge (see below). Several window lengths and different window step length were applied to the data, where possible, and no real improvement for the interpretation of the roughness values was detected, since the median of the values ranged in the same area as the roughness value calculated without the sliding window.

Like the subsidence of the basin, the roughness is biased by volcanoes and seamounts, fracture zones, anomalous spreading and hotspots.

10.3 Calculation and illustration

The main regions to calculate crustal roughness were selected according to reliability of the picks of the basement. For example, the basement relief of profile 20010100 is uncertain for the first 2000 CDPs, because the data quality is impaired by coarse material deposited from the shelf areas (see stacked profile sections). Other terminators are the axial valley and chron 24 (see below).

Spreading rates were not constant through time at the Gakkel Ridge. A spreading rate versus age model was developed by Karasik (1968) and represented and revised by Vogt et al. (1979).

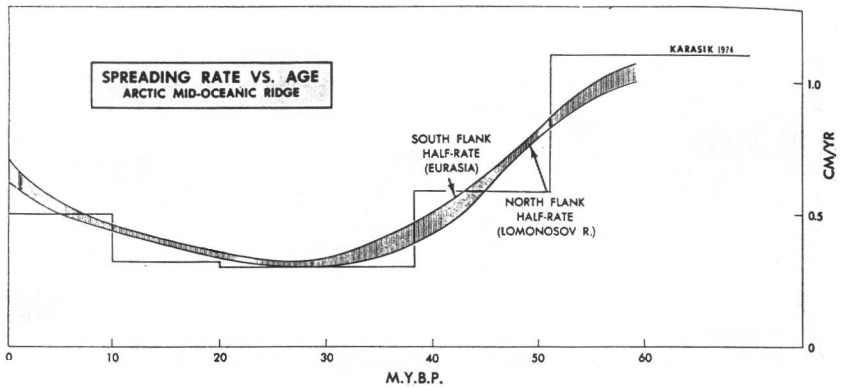

Figure 10.1: Half spreading rates vs. age for GR after Karasik (1968) and Vogt et al. (1979). The figure is reduced from the original to show the relevant portion for this work.

Figure 10.1 shows the spreading history obtained by Karasik (1968) (step function) and the

revised model by Vogt et al. (1979) (line band), which includes asymmetric spreading of Gakkel Ridge. The values of the curves from Vogt et al. (1979) are not given explicitly but do fit the step function of Karasik (1968). Neither study is able to distinguish conclusively between gradual and stepwise changes in spreading rate.

The spreading half rates, given by Karasik (1968), are: 5, 3.2, 3, 5.9 and 11 mm/yr for the time intervals bounded by chrons 1, 5, 6, 13, 20 and 24. The roughness calculation must therefore be carried out for each time window, resembling a different spreading rate. Since the Gakkel Ridge always showed a slow spreading regime, the corresponding swaths of oceanic crust are not as wide, as those, created by the Mid Atlantic Ridge in the same period. Some of these crustal sections don't fit the criteria of a minimum profile length (100 km) and must be excluded from further interpretation.

Because asymmetric spreading requires the systematic, preferential accretion of new crust to one flank, any resultant roughness variations between the ridge flanks must be the result of the persistent unequal partition, by faulting and volcanism, of the newly-accreted axial zone material (Hayes and Kane, 1991). Asymmetric spreading of approx. 10 - 15 % maximum at Gakkel Ridge was not resolvable with the available data. The errors of the roughness values (see below) are larger than the differences of roughness values for asymmetric or symmetric spreading rates calculated after the power law of (Malinverno, 1991).

The values for the basement depths can be taken from the picks made with the VELMOD module during the depth conversion process. The data points were re-sampled to the equal spacing of one CDP, because the picking was not done at equal distances but rather at the topographic highs and lows of the basement. If the original and re-sampled data are superimposed, they differ only at a few spots with minor amounts that can be neglected. Afterwards, these depth values are subtracted from the subsidence curve to obtain the residual basement relief, h. Inside the interval for each spreading rate, bounded by the chrons or other border criteria, the roughness, Ri, was calculated with equation 10.1 and compared to the corresponding roughness, Rc, obtained after the curve fitting equation 10.2 from Malinverno (1991).

The boundary between 3 and 5.9 mm/y half spreading rate, chron 13 (37 Myrs), was replaced with chron 15 (39 Myrs). This exchange was necessary in order to use the same age model as in the line drawings and subsidence calculations. This is possible, since these two chrons lie close together, only within 3 Myrs (Harland et al., 1982). The maximum lateral error of this change results to 18 km in the location of the chron, if the greater half spreading rate (5.9 mm/y) is assumed. This error is acceptable, because chron 15 separates areas where spreading was constant for a long period of time (chron 6 - 15 (10 - 39 Myrs) and 15 - 23 (39 - 52 Myrs)).

The following figures (10.2 - 10.5) show the used boundaries, the residual basement topography and the roughness values. In addition the used and omitted values for further interpretation are marked with green and red boxes. The best way to read the figures is from bottom to top, the seafloor is shown for orientation. Figure 10.2 explains the details of the figures.

Figure 10.2: Legend for the following figures

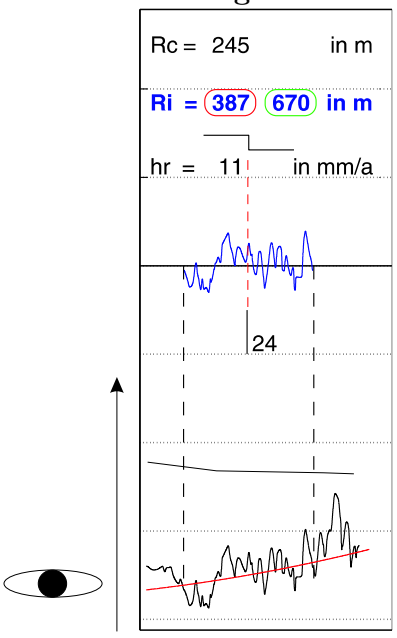

Roughness after Malinverno (1991), power law.

Calculated roughness after Malinverno (1991), marked for further interpretation.

Half spreading rate after Vogt (1979), graphic step-function and values.

Residual basement relief used for calculation in selected regions (black dashed lines), subdivided by red dashed lines for each spreading velocity.

Chron number

Seafloor

Basement and subsidence curve

Figure 10.3:
Profile : 20010100, Nansen Basin

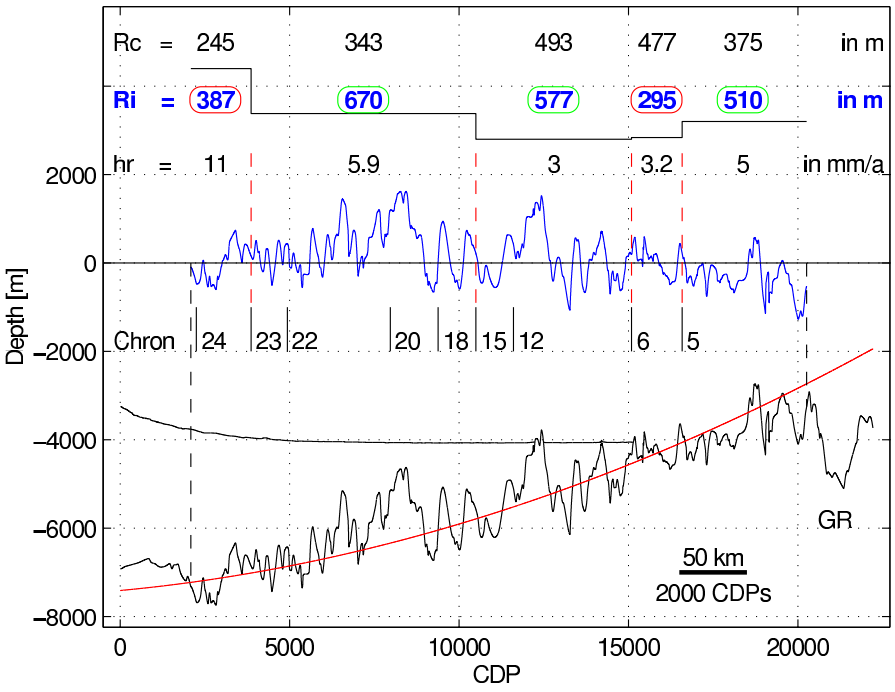

Figure 10.4:
Profile: 20010300, Amundsen Basin

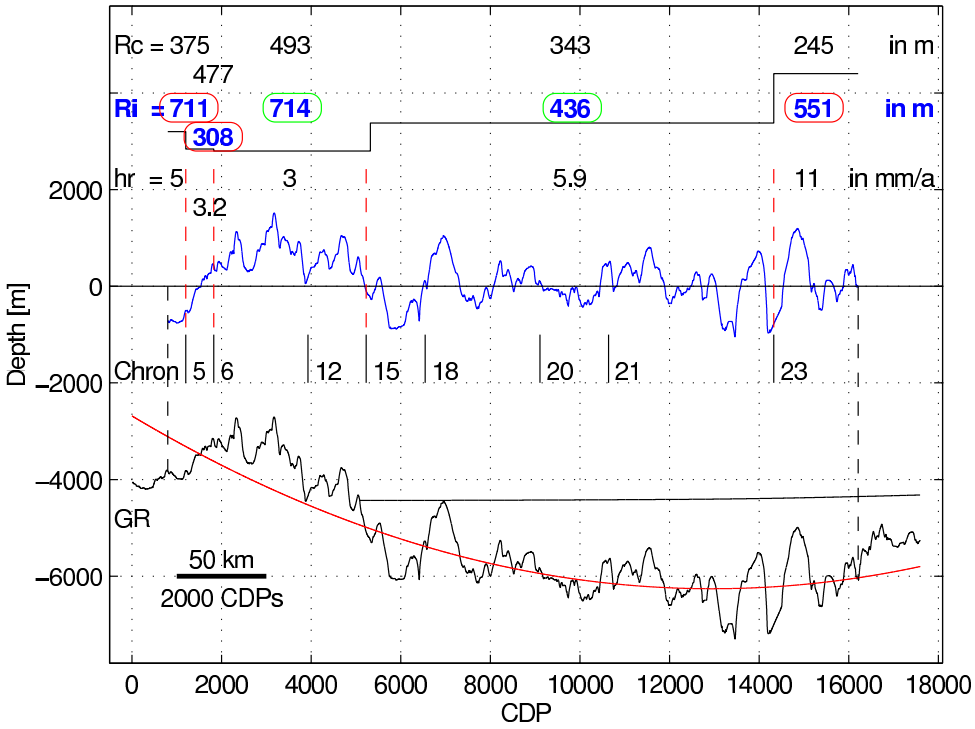

Figure 10.5:
Profile: 20010460, Nansen Basin

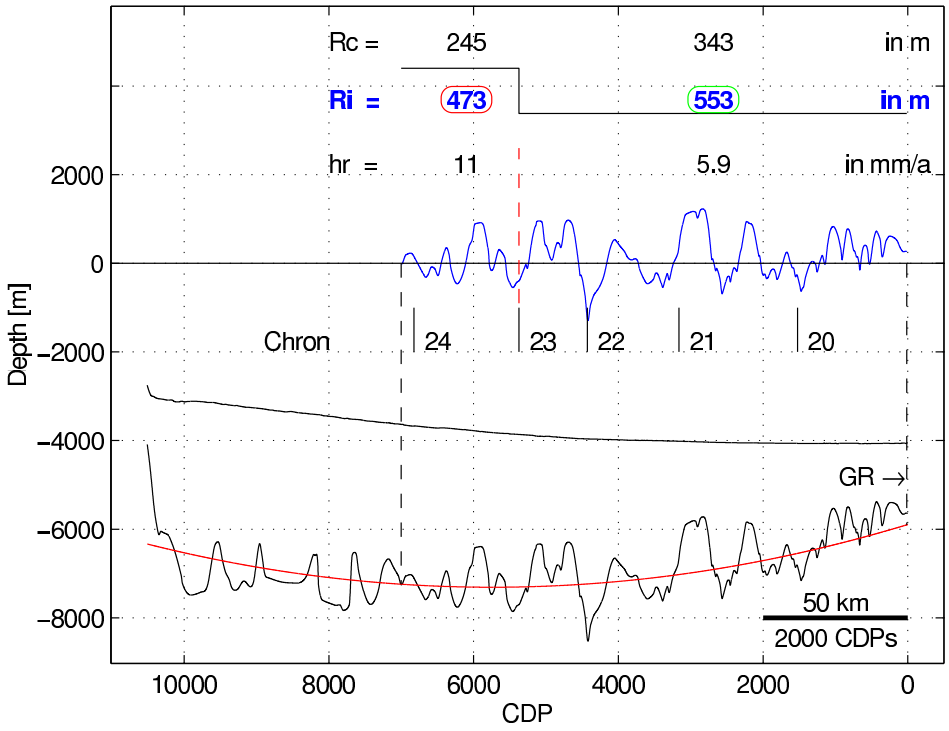

10.4 Results and interpretation

Figure 10.6 shows the results of the roughness analysis (blue circles) including the values given by Weigelt and Jokat (2001) (triangles). In addition, the results from Malinverno's (1991) studies are shown. Grey circles mark the values that are omitted, due to a too short profile length or position close to the ridge axis.

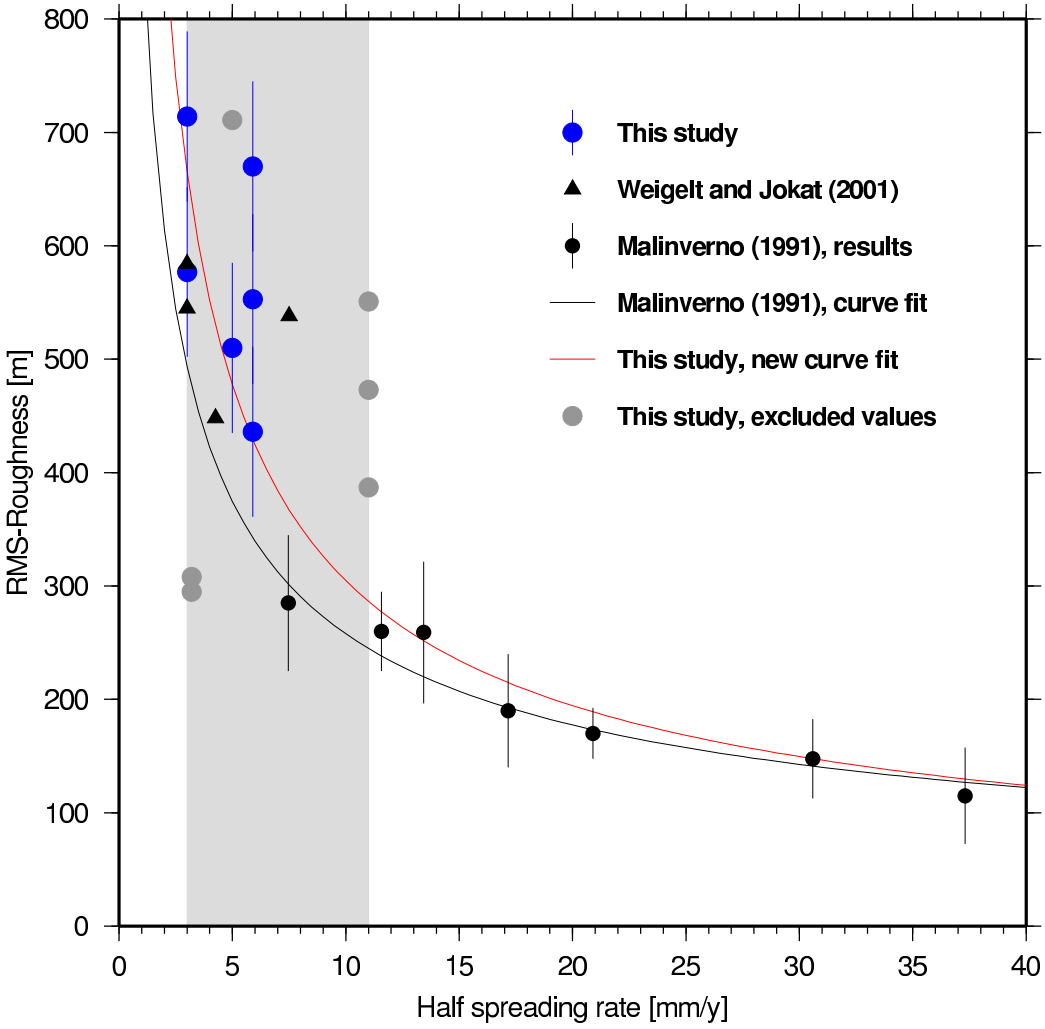

Figure 10.6: Results of roughness analysis. The grey shaded area marks the range of spreading rates for Gakkel Ridge, the blue error bars amount to ±75 m

All the roughness values from the Arctic region, inclusive the given error bars, lie above the curve derived by Malinverno (1991). The values calculated by Weigelt and Jokat (2001) agree with the values obtained in this study. The excluded values lie in the greater range of the usable values, but don't fit the general trend. This proves the demands for a minimum profile length and border criteria. For example, in figure 10.4 the residual basement reliefs between chrons 1 and 5 and 5 and 6 are not representative because the area lies close to the deep axial

valley of Gakkel Ridge and the lengths of both profile sections are under 100 km.

The error bars for the values of this study are taken from the uncertainty of the subsidence curves. Their error is about ± 75 m. Since Malinverno (1991) used a empirical linear trend as reference for the basement, no comparable errors could be given. The error bars shown for his studies derive from the range of calculated roughness values for a certain spreading rate. They simply show the variation in the values, reduced for a better visibility. The spreading model and the basement picks are assumed error free (Malinverno, 1991).

The obtained values for the Arctic region confirm the prediction that slow spreading rates are characterized by rough basement. The degree of roughness at Gakkel Ridge is higher than expected, or predicted by Malinvernos (1991) law. The variations in the values for small spreading rates also increase as observed by Malinverno (1991) and other authors. For example, roughness values at 5.9 mm/y half rate range from 436 m to 670 m (234 m). For a half spreading rate of 13.5 mm/y, the variation is just 125 m. Small changes in the spreading regime of slow oceanic ridges may therefore result in big changes in basement roughness, whereas faster spreading ridges are not so sensitive to changes in spreading velocity. This is clearly visible in the fitted power law curve.

A new curve fit (red line in fig 10.6) was applied to all the data sets shown in figure 10.6. The result shows a steeper increase for slow spreading rates, but is still similar to the law obtained by Malinverno (1991). The revised power law is:

$$R = 2126 \cdot v^{-0.6484}. \tag{10.3}$$

This similarity is also shown in figure 10.7. Almost no difference exists for half spreading rates greater than 35 mm/a. The roughness values stay at a constant level of 80 to 100 m and sustain the idea of a more linear trend for half spreading rates greater than 30 mm/y (Small, 1994; Hayes and Kane, 1991).

In addition to the already shown data, more data examples, from various authors, are shown to provide a more global view on the obtained data. There is quite some variation in the shown values, but they all fit the general trend reasonably well. The black triangles mark roughness values of Mesozoic crust, sections from the North Atlantic (Canary Basin, for example). This is older crust (+ 65 Ma) than found in the Amundsen and Nansen Basins. These values fit into the global data set, indicating the independence of roughness and age of the crust.

The large variation in roughness values for ultra slow spreading ridges shows, that it is not possible to draw conclusions about the spreading rate, as it is possible for intermediate to fast ridges. There, roughness changes indicate a change in the spreading rate like it was found in the North Atlantic by Sundvik et al. (1984). A wide spread decrease in crustal roughness marks a change in spreading rate during the Mesozoic era.

Small changes in spreading rates are also not resolvable for fast spreading ridges, due to the general uniform roughness values.

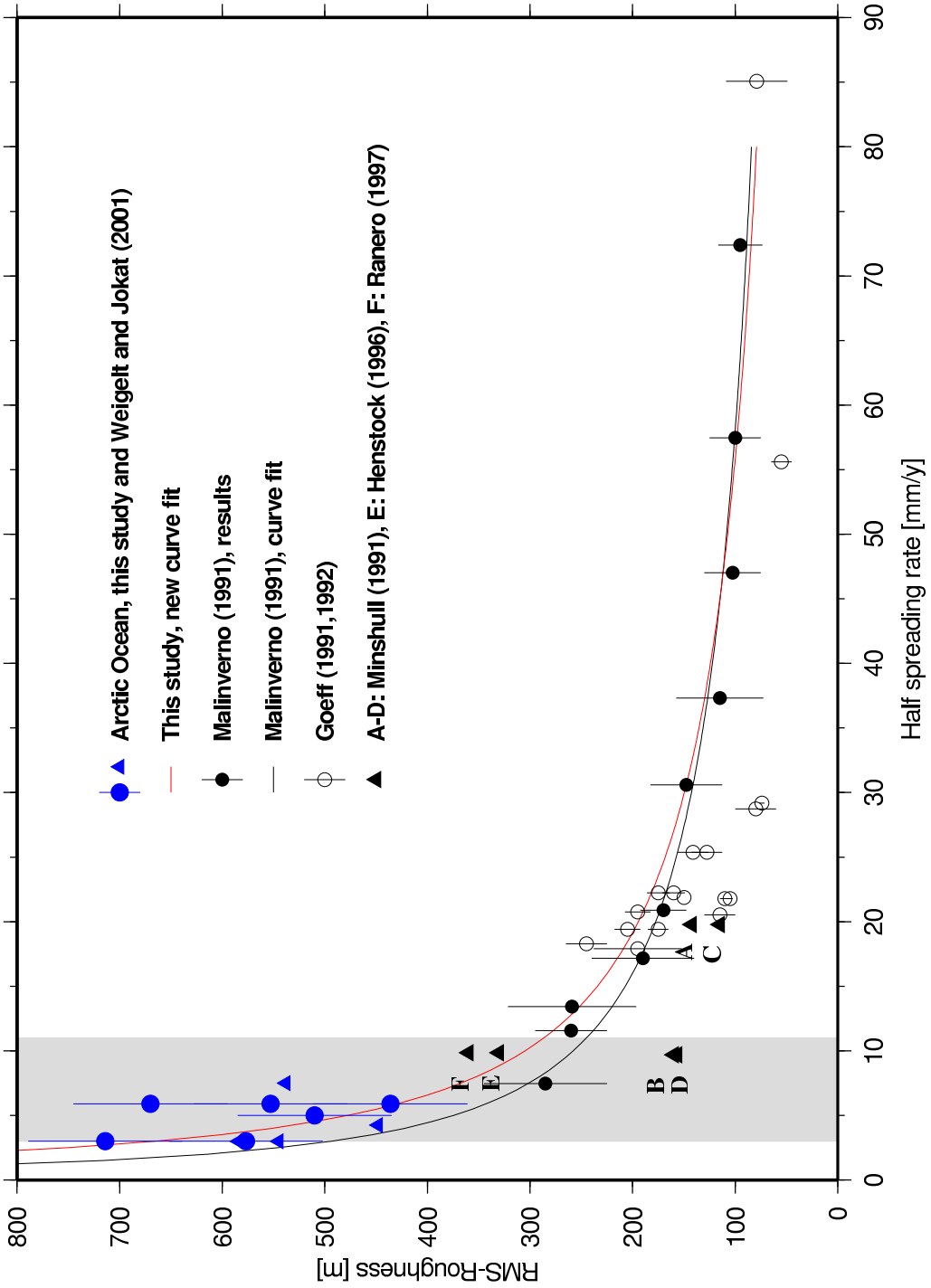

Figure 10.7: Results of roughness analysis, compilation after Rogenhagen (2000) modified to include recent data for the Arctic Ocean. The values marked with black triangles originate from Mesozoic North Atlantic crust. The grey shaded area marks the range of spreading rates for Gakkel Ridge, the blue error bars amount to ±75 m

11 Nansen vs. Amundsen Basin, a comparison

The profiles acquired 2001 permit a comparison between the two oceanic basins. The data was processed and interpret with the same methods and is therefore highly comparable. The reader is referred to the foldout maps and line drawings shown in the appendix for a better placement of the profiles and the geographic names. Some of the following observations and theories are also described in a publication by Jokat and Micksch (2004), in press.

At a first glance, the abyssal plains are very flat and deep. The Nansen Basin is significantly shallower than the Amundsen Basin, the water depths are 4050 to 4400 m, respectively. This difference has been reported by almost all researchers working in the Eurasia Basin and is explained by the minor amount of sediments received by the Amundsen Basin during its evolution.

In case of the Nansen Basin, the main source of sediments are the European and West Siberian Shelf regions (Kara and Barents Shelf), up to the Laptev Shelf, with the vast amount of material brought into the ocean from the hinterland. The sediments are deposited in rockfall, slumps and debris flows, originating from shelf break erosion with accompanying turbidity currents (Sand and mud turbidites) which reach farther into the basin. A compilation of marine erosional processes is shown in figure 11.1.

The right foreground of the figure shows erosional structures related to shelf break erosion. The truncated slope (far right side) shows sedimentary structures, similar to the structures found in closeups of the merged profiles 99176 and 20010100 near the foot of the continental slope. In addition, some detached blocks (marked 'old rocks') are shown under the shelf. Structures like this are associated with passive continental margins, like the margins in the Eurasian Basin. In profile 99176, these horst and graben structures are buried by propagating shelf sequences of glacial origin.

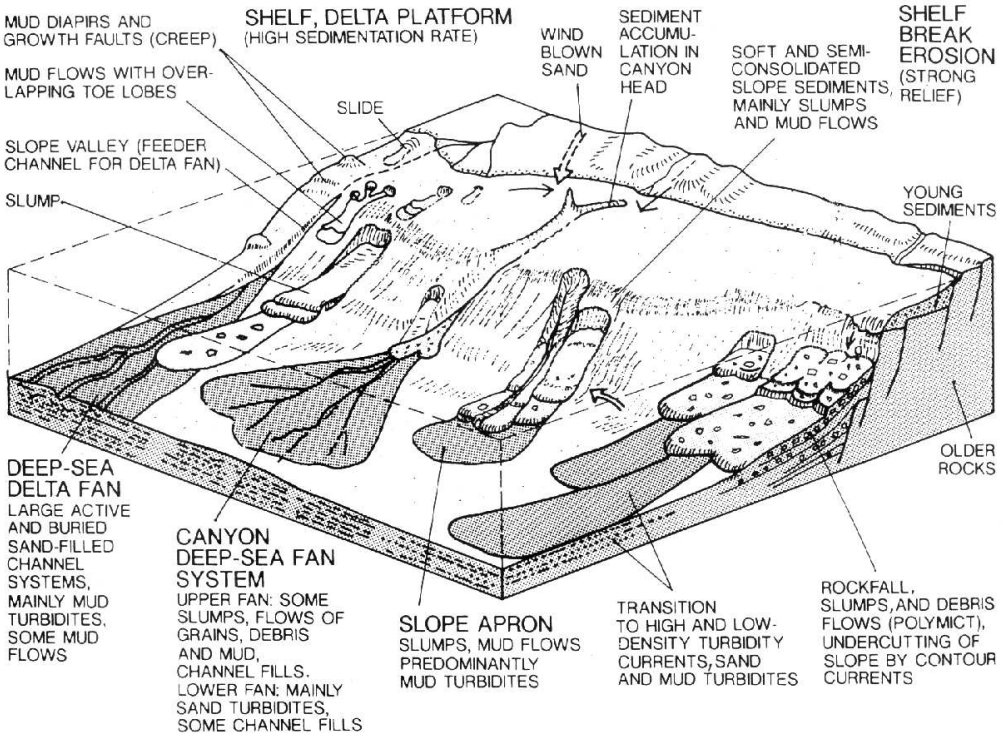

Figure 11.1: A compilation of marine erosional processes (Seibold and Berger, 1993).

The terrestrial sediments reaching the surveyed area in the Amundsen Basin by means of sub-marine transport consist of fine-grained materials (i.e. clay minerals). They are carried in turbidity streams and water currents for far distances. The borders of the basin towards Greenland and the Laptev Sea surly will show the effects described for the NB with a close terrestrial sediment source.

Other main sediment sources are a constant supply of biogenous (i.e. shells) and dead organic matter (Pelagic Rain) and the mud, sand and rock deposits from melting icefloes. In addition, material distributed in the Earths' atmosphere like dust (i.e. volcanic origin) and aerosols (i.e. heavy metals) contribute to the buildup, formation and alternation of the sediments and sedimentary rocks. Figure 11.2 shows an example of recent sediments in the AB.

The sediment thickness in the Nansen Basin is more than double than that in the Amundsen Basin, especially in the older crustal sections, close to the continental slope (NB). In the Nansen Basin the sediments thin out, whereby the sediments in the Amundsen Basin increase slightly in thickness towards Gakkel Ridge. This may be explained with the remote position where profile 20010300 meets LR, and that the major amount of transported sediments do not reach that far. Particles from the far eastern side (Chukchi Shelf, East Siberian Shelf), transported in deep water layers, may get blocked by the Lomonosov Ridge.

The old (first deposited) sediments also show differences: In the Amundsen Basin, the lower sedimentary layers dip southwards (0.28°), towards GR, a pattern that is not found in the NB.

Figure 11.2: The 'ultra-fine' structure of sediments from the Amundsen Basin. They were obtained with a 'gravity corer' penetrating the seafloor (approx. 10 m). The light and dark sequences originate from different sedimentary regimes and materials during cold and warm times (i.e. ice and no ice floes present for sediment transport).

An explanation may be a slower sediment deposition and a main particle transport in direction of the basin, rather than perpendicular to the basin axis during that time. Lomonosov Ridge as source for terrestrial sediments ceased around 50 Myrs, when the ridge crests were subsided below sealevel (Jokat et al., 1995). Lomonosov Ridge did not provide enough material just after break-up to significantly depress the oceanic crust close to its foot. In the NB, higher sedimentation rates and sediment loading close to the shelf margin depressed the oceanic crust more. The Amundsen basin was rather uniformly filled with sediments.

The sediment velocities differ slightly between both basins. In the Nansen Basin the top velocities are 3.3 to 3.8 km/s, whereas in the Amundsen Basin, the top velocities are 2.8 to 3 km/s. Different compaction of the deeper sediment layers (because of different overburdens) might be the reason, since the high velocities are found in the older parts of NB, for example.

In the Amundsen Basin, the basement stays at rather the same level (depth of 6 km) between CDP 7500 and 12000, whereas the depth of the basement in the Nansen basin increases steadily away from the ridge. In addition, a rather distinct and abrupt change in basement depth is visible in the Amundsen Basin around CDP 5500, also found by Weigelt (1998) in the data set of 1991 in a similar way. This might be a characteristic feature for the entire basin and not a local observation.

Further explanations for differences and similarities of the basins are sought-after, and are believed to be connected to the ultra-slow spreading rate and the slight asymmetric spreading. The results of the subsidence and roughness analysis were investigated towards this, but no anomalous subsidence was detected, for example. The next chapter summarizes all key results of this thesis.

12 Major results and prospect

The major results after processing, modelling and the appliance of geological tools are listed below:

Sedimentary velocities:
A reliable velocity model for the sedimentary horizons in the survey area was developed by ray-tracing. The sedimentary velocities range from 1.8 - 3.8 in the Nansen Basin and are slightly lower in the Amundsen Basin. This can be explained by different compaction rates, due to the lesser sediment overburden. These seismic velocities can be converted to densities, for example, for further gravimetric modelling of the Eurasian Basin.

Depth conversion, depth sections and line drawings:
Depth sections of the seismic data were created, using the stacked time section and the refraction velocity model. They are presented in form of line drawings, including the velocity model. These provide the first complete view of the deeper structure of the Nansen and Amundsen Basins in the western part of the Eurasian Basin. The sediment thicknesses and the crustal relief is now known in detail, constraint by seismic data. Any depth-to-source algorithm for magnetic data can be calibrated against these results, for example. Plots of the stacked and depth-converted sections, as well as the line drawings can be found in the appendix.

Subsidence history:
The thermal model relationship of Parsons and Sclater (1977) and the sediment correction after Allen and Allen (1990) was used for calculation. The curves are included in the line drawings. The subsidence of the Nansen and Amundsen Basins seems to be rather normal, no evident effect of the asymmetric spreading was detected, for example. Locally, the basement shows deviations from the curve at huge buried seamounts.

Roughness analysis:
Crustal roughness in the Eurasian Basin is higher than expected or predicted by a trend of previous available data (Malinverno, 1991). The new obtained values fit to those obtained by Weigelt (1998) for the Nansen and Amundsen Basin. The values prove the assumptions, that slow spreading rates result in rough crustal topographies. The large variation in roughness values for ultra slow spreading ridges shows, that it is not possible to draw conclusions about the spreading rate, as it is possible for intermediate to fast ridges.

The crawled data provides a good insight into the structure of the Eurasian Basin, but only

to the top of the basement. Together with the acquired gravimetric data during the AMORE cruise, a profound crustal model could be developed. With existing gravimetric models from the borders of the surveyed area (Svalbard, GR, LR) as constraints, a complete gravimetric transect through the Eurasian Basin is possible, for example. In addition, a stratigraphic model could be be created and compared to existing models by Jokat et al. (1995).

The shown seismic lines and interpretations are only a small part of the complete geophysical and petrological data set from the AMORE cruise. Together with the recent findings and publications on Gakkel Ridge, a huge amount of new data is now available for further interpretation and calibration of existing models.

References

Allen, P. A. and J. R. Allen (1990). *Basin analysis - principles and applications*. Blackwell Scientific Publications.

Beaumont, E. A. and N. H. Foster (1988). *Geophysics I-IV*. American Association of Petroleum Geologists (AAPG).

Berckhemer, H. (1997). *Grundlagen der Geophysik*. Wissenschafttliche Buchgesellschaft Darmstadt.

Brozena, J. M., V. A. Childers, L. A. Lawver, L. M. Gahagan, R. Forsberg, J. I. Faleide and O. Endholm (2003). New aerogeophysical study of the Eurasia Basin and Lomonossov Ridge: Implications for basin development. *Geology 31*(9), 825–828.

Červený, V., I. Molotkov and I. Pšenčík (1977). *Ray method in seismology*. University of Karlova, Prague.

Chand, S. and T. A. Minshull (2003). Seismic constraints on the effects of gas hydrate on sediment physical properties and fluid flow: a review. *Geofluids 3*, 275–289.

Chen, Y. J. (1992). Oceanic crustal thickness versus spreading rate. *Geophysical Research Letters 19*(8), 753–756.

Dick, H. J. B., J. Lin and H. Schouten (2003). An ultraslow-spreading class of ocean ridges. *Nature 426*, 405–412.

Dix, C. H. (1955). Seismic velocities from surface measurements. *Geophysics XX*(1), 68–86.

Eisbacher, G. H. (1996). *Einführung in die Tektonik*. Ferdinand Enke Verlag, Stuttgart.

Feden, R. H., P. R. Vogt and H. S. Fleming (1979). Magnetic and bathymetric evidence for the "Yermak Hot Spot" northwest of Svalbard in the Arctic Basin. *Earth and Planetary Science Letters 44*, 18–38.

Forkmann, B. (1987). Geschwindigkeitsbestimmung, pp. 133–151, Apparativ-methodische Grundlagen, pp. 65–105. In H. Militzer and F. Weber (Eds.), *Angewandte Geophysik, Band 3, Seismik*. Springer-Verlag Wien/Akademie Verlag Berlin.

Fowler, C. M. R. (1990). *The solid earth: An introduction to global geophysics*. Cambridge University Press.

Gaina, C., W. R. Roest and R. D. Müller (2002). Late Cretaceous - Cenozoic deformation of northeast Asia. *Earth and Planetary Science Letters 197*, 273–286.

Gauger, S. (2002). Aufbereitung, Visualisierung und Analyse einer bathymetrischen Vermessung im westlichen Teil des Gakkel-Rückens. Master's thesis, Hochschule für Angewandte Wissenschaften Hamburg.

Geissler, W. H. (2001). Marine seismische Untersuchungen am nördlichen Kontinentalrand von Svalbard (Spitzbergen). Master's thesis, Institut für Geophysik der Technischen Universität Bergakademie Freiberg and AWI.

Goff, J. A. (1991). A global and regional stochastic analysis of near-ridge abyssal hill morphology. *Journal of Geophysical Research 96*(B13), 21713–21737.

Goff, J. A. (1992). Quantitative characterization of abyssal hill morphology along flow lines in the Atlantic Ocean. *Journal of Geophysical Research 97*, 9183–9202.

Grantz, A., L. Johnson and J. F. Sweeney (1990). *The Arctic Ocean region*. The Geological society of America, Inc.

Harland, W. B., R. L. Armstrong, A. V. Cox, L. E. Craig, A. G. Smith and D. G. Smith (1982). *A geologic time scale*. Cambridge University Press, Cambridge.

Hayes, D. E. and K. A. Kane (1991). The dependence of seafloor roughness on spreading rate. *Geophysical Research Letters 18*(8), 1425–1428.

Heezen, B. C. and M. Ewing (1961). *Geology of the Arctic*, Chapter The Mid-Oceanic Ridge and its extension through the Arctic Basin. University of Toronto Press.

Helm, V. (2003). Die Struktur des Kontinentalrandes im Gebiet des Larsenschelfes, Antarktische Halbinsel. Master's thesis, Institut für Geophysik der Technischen Universität Bergakademie Freiberg and AWI.

Henstock, T. J. and R. S. White (1996). Along-axis variability in crustal accretion at the Mid-Atlantic Ridge: Results from the OCEAN study. *Journal of Geophysical Research B6*(101), 13673–13688.

Herber, R., W. Weigel and H. K. Wong (1997). Relationship between Shot-induce noise and shot interval in seismic refraction experiments at sea. *Marine Geophysical Researches 19*, 257–265.

Hübscher, C. (1994). Krustenstrukturen und Verlauf des Kontinentalrandes im Weddell-Meer/Antarktis. *Berichte zur Polarforschung (Reports on Polar Research) 147*.

Jakobsson, M., N. Z. Cherkis, J. Woodward, R. Macnab and B. Coakley (2000). New grid of Arctic bathymetry aids scientists and mapmakers. *EOS 81*, 89,93,96.

Johnson, G. L. (1990). *Geological History of the Polar Oceans: Arctic versus Antarctic*, Chapter Morphology and Plate Tectonics: The modern Polar oceans., pp. 11–28. Kluwer Academic Publishers.

Jokat, W., M. Alvers, V. Y. Buravtsev, B. Heesemann, Y. Kristoffersen and G. Uenzelmann-Neben (1992). ARCTIC'91: The expedition ARK VIII\3 of R/V Polarstern in 1991. *Berichte zur Polarforschung (Reports on Polar Research) 107*.

Jokat, W., V. Y. Buravtsev and H. Miller (1994). Marine seismic profiling in ice covered regions. *Polarforschung 64*(1), 9–17.

Jokat, W. and U. Micksch (2004). Sedimentary structure of the Nansen and Amundsen basins; accepted 14 November 2003, published 2004. *Geophysical Research Letters*.

Jokat, W., O. Ritzmann, M. C. Schmidt-Aursch, S. Drachev, S. Gauger and J. Snow (2003). Geophysical evidence for reduced melt production on the Arctic ultraslow Gakkel mid-ocean ridge. *Nature 423*, 962–965.

Jokat, W., E. Weigelt, Y. Kristoffersen, T. Rasmussen and T. Schöne (1995). New insights into evolution of the Lomonosov Ridge and the Eurasian Basin. *Geophysical Journal International 122*, 378–392.

Jones, E. J. W. (1999). *Marine Geophysics*. John Wiley and Sons, Ltd.

Juteau, T. and R. Maury (1999). *The oceanic crust, from accreation to mantle recycling*. Springer Verlag and Praxis Publishing, Chichester, UK.

Karasik, A. M. (1968). Magnetic anomalies of the Gakkel Ridge and origin of the Eurasia Subbasin of the Arctic Ocean. *Geophys. Methods Prospect. Arctic 5*, 8–19.

Kerz, W. (1992). *Einführung in die Geophysik, Band 1*. Spektrum Akademischer Verlag.

Kiær, H. (1906). *The Norwegian North Polar Expedition 1893 – 1896*, Chapter Thalamophora of the bottom deposits and mud from the ice surface. New York, Longmans, Green & Co.

Kim, G. Y. and D. C. Kim (2001). Comparison and correlation of physical properties from the plain and slope sediments in the Ulleung Basin, East Sea (SEa of Japan). *Journal of Asian Earth Science 19*, 669–681.

Kovacs, L. C. and P. R. Vogt (1982). Depth-to-source analysis of the Arctic Ocean region. *Tectonophysics 89*, 255–294.

Kristoffersen, Y. (1990). *The Arctic Ocean region*, Chapter Eurasia Basin. The Geological society of America, Inc.

Malinverno, A. (1991). Inverse square-root dependence of mid-ocean ridge flank roughness on spreading rate. *Nature 352*, 58–60.

Malinverno, A. and P. A. Cowie (1993). Normal faulting and the topographic roughness of mid-ocean ridge flanks. *Journal of Geophysical Research 98*(B10), 17921–17939.

McKenzie, D. P. (1978). Some remarks on the development of sedimentary basins. *Earth and Planetary Science Letters 40*, 25–33.

McMechan, G. A. and W. D. Mooney (1980). Asymptotic ray theory and synthetic seismograms for laterally varying structure: theory and application to the Imperial Valley, California. *Bulletin of the Seismological Society of America 70*, 2021–2035.

Michael, P. J., C. H. Langmuir, H. J. B. Dick, J. Snow, S. L. Goldstein, D. W. Graham, K. Lehnert, G. Kurras, W. Jokat, R. Mühe and H. N. Edmonds (2003). Magmatic and amagmatic seafloor generation at the ultraslow-spreading Gakkel Ridge, Arctic ocean. *Nature 423*, 956–961.

Militzer, H. and F. Weber (1987). *Angewandte Geophysik, Band 3, Seismik*. Springer-Verlag Wien/Akademie Verlag Berlin.

Minshull, T. A. (1999). On the roughness of Mesozoic oceanic crust in the western North Atlantic. *Geophysical Journal International 136*, 286–290.

Minshull, T. A., R. S. White, J. C. Mutter, P. Buhl, R. S. Detrick, C. A. Williams and E. Morris (1991). Crustal structure at the Blake Spur fracture zone from expanding spread profiles. *Journal of Geophysical Research 96*(B6), 9955–9984.

Myhre, A. M. and J. Thiede (1995). *Proceedings of the Ocean Drilling Program , Initial Reports, Vol.151*, Chapter North Atlantik - Arctic Gateways. National Science Foundation.

Nansen, F. (1906). *The Norwegian North Polar Expedition 1893 – 1896*. New York, Longmans, Green & Co.

Palmer, D. (1986). *Refraction Seismics, The lateral resolution of structure and seismic velocity*. Geophysical Press.

Parsons, B. and J. G. Sclater (1977). An analysis of the variation of ocean floor bathymetry and heat flow with age. *Journal of Geophysical Research 82*(5), 803–827.

Press, F. and R. Siever (1994). *Understanding earth*. W.H. Freeman and Company, New York.

Ranero, C. R., E. Banda and P. Buhl (1997). The crustal structure of the Canary Basin: Accretion processes at slow spreading centers. *Journal of Geophysical Research 102*(B5), 10185–10201.

Ritzmann, O. and W. Jokat (2003). Crustal structure of northwestern svalbard and the adjacent Yermak Plateau: evidence for Oligocene detachment tectonics and non-volcanic breakup. *Geophysical Journal International 22*(3), 523–552.

Robinson, E. S. and C. Çoruh (1988). *Basic Exploration Geophysics*. John Wiley and Sons, Ltd.

Rogenhagen, J. (2000). Interpretation seismischer und gravimetrischer Daten des Weddellmeeres, Antarktis. *Berichte zur Polarforschung (Reports on Polar Research) 369*.

Sawyer, D. S. (1985). Total tectonic subsidence: A parameter for distinguishing crust type at the U.S. Atlantic continental margin. *Journal of Geophysical Research 90*(B9), 7751–7769.

Schmöller, R. (1987). Bearbeitung reflexionsseismischer Daten. In H. Militzer and F. Weber (Eds.), *Angewandte Geophysik, Band 3, Seismik*, pp. 188–231. Springer-Verlag Wien/Akademie Verlag Berlin.

Sclater, J. G. and J. Francheteau (1970). The implications of terrestrial heat flow observations on current tectonic and geochemical models od the crust and upper mantle of the earth. *Geophysical Journal of the Royal astronomical Society 20*, 509–542.

Seibold, E. and W. H. Berger (1993). *The sea floor. An introduction to Marine Geology*. Springer Verlag.

Sheriff, R. E. and L. P. Geldart (1986). *Exploration seismology*. Cambridge University Press.

Sleep, N. H. and B. R. Rosendahl (1979). Topography and tectonics of mid-ocean ridge axes. *Journal of Geophysical Research 84*(B12), 6831–6839.

Small, C. (1994). A global analysis of mid-ocean ridge axial topography. *Geophysical Journal International 116*, 64–84.

Sundvik, M., R. L. Larson and R. S. Detrick (1984). Rough smooth basement boundary in the western North Atlantic basin: Evidence for a seafloor-spreading origin. *Geology 12*, 31–34.

Taylor, P. T., L. C. Kovacs, P. R. Vogt and G. L. Johnson (1981). Detailed aeromagnetic investigation of the Arctic Basin. *Journal of Geophysical Research 86*, 6323–6333.

Telford, W. M., L. P. Geldart, R. E. Sheriff and D. A. Keys (1985). *Applied Geophysics*. Cambridge University Press.

Vogt, P. R., P. T. Taylor, L. C. Kovacs and G. L. Johnson (1979). Detailed aeromagnetic investigations of the Arctic Basin. *Journal of Geophysical Research 84*(B3), 1071–1089.

Weigelt, E. (1998). Die Krustenstruktur und Sedimentdecke des Eurasischen Beckens, Arktischer Ozean: Resultate aus seismischen und gravimetrischen Untersuchungen. *Berichte zur Polarforschung (Reports on Polar Research) 261*.

Weigelt, E. and W. Jokat (2001). Peculiarities of roughness and thickness of oceanic crust in the Eurasian Basin, Arctic Ocean. *Geophysical Journal International* (145), 505–516.

Yilmaz, Ö. (1987). *Seismic Data Processing, investigations in geophysics*. Society of Exploration Geophysicists, SEG.

Yilmaz, Ö. (2001). *Seismic Data Analysis: Processing, Inversion and Interpretation of Seismic Data*. Society of Exploration Geophysicists, SEG.

Zelt, C. A. (1998). Zplot – an interavtive plotting and picking program for seismic data. *modified by P. Sroda, Warsaw 1999*.

Zelt, C. A. and R. M. Ellis (1988). Practical and efficient ray tracing in two-dimensional madia for rapid traveltime and amplitude forward modelling. *Canadian Journal of Exploration Geophysics 24*, 16–31.

Zelt, C. A. and R. B. Smith (1992). Seismic traveltime inversion for 2-D crustal velocity structures. *Geophysical Journal International 108*, 16–34.

v5.0 Focus Manual (2002). *The DISCO/Focus Reference Manual*. Paradigm Geophysical Ltd.